Interaction between oscillating-grid turbulence and a solid impermeable boundary

Mark W. McCorquodale, MEng.

Thesis submitted to the University of Nottingham
for the degree of Doctor of Philosophy

October 2017

Abstract

The interaction of a boundary with turbulence is a defining feature of many turbulent flows, resulting in a turbulent boundary layer which plays a prominent role in the production and dissipation of turbulence. Commonly, this interaction is dominated by the effects of mean shear. However, more subtle aspects of the interaction, such as effects associated with turbulent motions impinging onto the boundary, are still thought to play a key role in giving rise to the boundary layer structure. Unfortunately, these aspects of the interaction are currently poorly understood. A better understanding of these aspects of the interaction may be derived by isolating them from the effects of mean shear through the study of zero-mean-shear turbulence interacting with a boundary.

This study reports experimental work investigating the interaction between oscillating-grid turbulence (OGT) and a solid impermeable boundary. OGT is a commonly used experimental tool that produces a turbulent flow which is approximately homogeneous and isotropic in planes parallel to the oscillating grid but which is inhomogeneous in planes perpendicular to the oscillating grid. Throughout this study, instantaneous velocity measurements of the flow are obtained by applying two-dimensional particle imaging velocimetry to the vertical plane through the centre of the oscillating grid.

A detailed preliminary study to characterise the flow generated by the OGT apparatus is initially performed. Visualisation of the flow close to the oscillating grid indicates that large-scale circulations are induced in OGT by the merging of grid-induced jets close to the tank walls. The installation of an open-ended cuboidal 'inner box' below the grid is shown to inhibit the merging of these jets, thereby resulting in a more regular jet structure close to the oscillating grid and a corresponding reduction in mean flow within the inner box. It is also found that, contrary to assumptions in the literature, this amendment to the standard OGT apparatus is most effective when the top of the inner box is located close to the oscillating grid. The reduction in mean flow intensity that results from the use of a correctly installed inner box brings about a turbulent flow in which the mean flow velocity components are small compared to velocity fluctuations, thereby enabling a meaningful comparison to be made with zero-mean-shear turbulence.

Consequently, the interaction between OGT and a solid impermeable boundary is studied to derive insight into the mechanisms governing the interaction of zero-mean-shear turbulence with boundaries. Results indicate that a critical aspect of the interaction is

the blocking of a boundary-normal flux of turbulent kinetic energy across the boundary-affected region, which acts to increase the magnitude of the boundary-tangential turbulent velocity components, relative to the far-field trend, but not the boundary-normal turbulent velocity component. This feature arises as a result of the anisotropic nature of the flow produced by OGT, whereby the turbulent fluctuations decay with distance normal to and away from the oscillating grid, and would not be present in a turbulent flow that was otherwise homogeneous above the boundary-affected region of the flow. This observation provides new insight into the validity of well-established models of the interaction of zero-mean-shear turbulence and a solid impermeable boundary and provides a physical mechanism that explains the disparity in previously reported measurements relating to this problem.

The results reported are also in support of intercomponent energy transfer mechanisms previously proposed to govern the interaction of zero-mean-shear turbulence with boundaries, including viscous and 'return-to-isotropy' mechanisms. That is, within a thin region adjacent to the boundary, approximately equal in thickness to the viscous sublayer, the data indicate that turbulent motions incident towards the boundary are more energetic than motions away, which are characteristics of an intercomponent energy transfer primarily driven by the viscous dissipation of turbulent kinetic energy. In addition, at the edge of the boundary-affected region, where the magnitude of the boundary-tangential turbulent velocity components exceeds the magnitude of the boundary-normal turbulent velocity component, results indicate that an intercomponent energy transfer occurs from the boundary-tangential turbulent velocity components to the boundary-normal turbulent velocity component in a so-called 'return-to-isotropy' energy transfer. However, the data also indicate the presence of an additional intercomponent energy transfer, from the boundary-normal turbulent velocity component to the boundary-tangential turbulent velocity components over a thin region outside the viscous sublayer. Comparison to previously published results of related studies indicates that this mechanism is also prevalent in previous work, but is not captured within existing models of intercomponent energy transfer at the boundary. Results further indicate that the intercomponent energy transfer mechanisms are not independent of the blocking of the boundary-normal turbulent kinetic energy flux. That is, the blocking of the boundary-normal turbulent kinetic flux promotes anisotropy within the boundary-affected region of the flow and thereby induces a stronger 'return-to-isotropy' energy transfer mechanism. Hence, the effect of a solid impermeable boundary on turbulent velocity components in zero-mean-shear turbulence depends critically on the nature of the original turbulent field (*i.e.* homogeneous or inhomogeneous turbulence).

Acknowledgements

First and foremost, I would like to thank my supervisor, Dr Rick Munro, for his support throughout my studies. His guidance, encouragement and, perhaps most importantly, patience pushed me through the inevitable missteps that I made during this research and has helped steer my professional development over the past four years. Further support and feedback throughout my PhD from Dr Barbara Turnbull and Dr David Hargreaves was also appreciated.

I thank the Engineering and Physical Science Research council (EPSRC) for the financial award of a studentship, without which I would have been unable to conduct these studies. My thanks for financial support also extend to the Fluids and Thermal Engineering research group and the Graduate School at the University of Nottingham and the Confederation of Scandinavian Societies.

I thank the technicians of the Civil Engineering Department for their assistance with the experimental apparatus, most notably Jim Meakin and Steve Lawton, who ensured that my plans were not only turned into being but that they also actually worked as intended!

However, my greatest appreciation goes to Catherine for her unwavering support throughout the inherent highs and lows that arose during the course of this work.

Statement of authorship

I certify that this thesis is submitted incorporating published works. Written statements from each co-author are included below attesting to my contribution to any jointly authored papers. I warrant that I have obtained, where necessary, permission to use any of my own published work in which the copyright is held by another party.

McCorquodale, M. W. and Munro, R. J. (2017). A method for reducing mean flow in oscillating-grid turbulence. *In preparation for: Experiments in Fluids*.

Statement from Author: I confirm that the research was first conceived by the lead author and that the detailed design of the experimental project, the data collection and the data analysis were performed solely by the lead author. The first draft of the paper was also written solely by the lead author but revisions were incorporated by Dr Munro before completion of the paper.

Statement of Contribution from Dr Rick Munro: I confirm that the statement above is an accurate description of the contribution of each co-author to this article.

McCorquodale, M. W. and Munro, R. J. (2017). Experimental study of oscillating-grid turbulence interacting with a solid boundary. *Journal of Fluid Mechanics*, 813:768-798.

Statement from Author: I confirm that the detailed design of the experimental project, the data collection and the data analysis were performed solely by the lead author. The first draft of the paper was also written solely by the lead author but revisions were incorporated by Dr Munro before completion of the paper.

Statement of Contribution from Dr Rick Munro: I confirm that the statement above is an accurate description of the contribution of each co-author to this article.

McCorquodale, M. W. and Munro, R. J. (2017). Analysis of intercomponent energy transfer in the interaction of oscillating-grid turbulence with an impermeable boundary. *Submitted to: Physics of Fluids*.

Statement from Author: I confirm that the detailed design of the experimental project, the data collection and the data analysis were performed solely by the lead author. The first draft of the paper was also written solely by the lead author but revisions were incorporated by Dr Munro before completion of the paper.

Statement of Contribution from Dr Rick Munro: I confirm that the statement above is an accurate description of the contribution of each co-author to this article.

Contents

1 Introduction **1**

1.1 Motivation 1

1.2 Previous work 5

1.3 Objectives and approach 12

2 A method for reducing mean flow in oscillating-grid turbulence **15**

2.1 Introduction 18

2.2 Experiments 21

2.2.1 Apparatus & Set-up 21

2.2.2 Velocity Measurements 24

2.3 Results 26

2.3.1 The mean-flow structure in the near-grid region with no inner box installed 26

2.3.2 The mean-flow structure in the near-grid region with inner box installed 31

2.3.3 Effect of mean flow on turbulent structure 35

2.4 Discussion 48

2.5 Conclusions 50

3 Experimental study of oscillating-grid turbulence interacting with a solid boundary **55**

3.1 Introduction 58

3.2 Experiments 63

3.3 Turbulence measurements within the bulk interior region 68

3.3.1 Side wall effects 68

3.3.2 Degree of isotropy 70

3.3.3 Spatial decay of the rms velocity components 70

3.3.4 Mean flow 71

3.4 Turbulence measurements in the boundary-affected region 72

3.4.1 Integral length scales 72

3.4.2 Root-mean-square velocity data 74

3.5 Turbulent kinetic energy in the boundary-affected region 78
3.5.1 Turbulent kinetic energy and turbulent kinetic energy flux 78
3.5.2 Reynolds stress and turbulent kinetic energy balances 82
3.6 Discussion 87
3.7 Conclusions 91

4 Analysis of intercomponent energy transfer in the interaction of oscillating-grid turbulence with an impermeable boundary 95
4.1 Introduction 98
4.2 Experiments 102
4.3 Estimates of the pressure-strain correlation 104
4.4 Energy spectra 107
4.5 Quadrant analysis 109
4.5.1 A criteria for isolating splats and antisplats 110
4.5.2 Conditional statistics 113
4.6 Discussion and Conclusions 117

5 Summary 122
5.1 Conclusions 122
5.2 Future work 125

Chapter 1

Introduction

This dissertation is split into 5 chapters; this introduction, a summary (chapter 5) and three chapters (chapters 2, 3 and 4) in the form of journal articles; chapter 2 is in preparation for submission, chapter 3 is a published article and chapter 4 is an article currently under review for publication. Each of chapters 2, 3 and 4 is presented as a self-contained research article (*i.e* each chapter presents a review of the relevant literature, the experimental method used, results, discussion and conclusions), but the related nature of the research reported within each article lends itself well to forming a collective body of research on the topic of the interaction of oscillating-grid turbulence (OGT) with a solid impermeable boundary. That is, chapter 2 reports a detailed preliminary experimental study to characterise the flow generated by the OGT apparatus and details a method to reduce the intensity of the mean flow produced by the oscillating grid such that the flow better approximates zero-mean-shear turbulence. Both chapters 3 and 4 report detailed experimental studies that investigate the interaction between OGT and a solid impermeable boundary in order to derive insight into the mechanisms governing the interaction of zero-mean-shear turbulence with boundaries. Note that due to the nature of research presented in chapters 2, 3 and 4 there is some repetition of material in these chapters, in particular with regards to descriptions of the apparatus used. This material has been retained within each chapter for clarity; minor differences are present in the precise apparatus used within each chapter. In addition, note that subtlety different notation or terminology is sometimes used in chapters 2, 3 and 4 (although every effort has been made to be as consistent as possible). To this end a list of nomenclature is provided at the start of chapters 2, 3 and 4 defining the notation used.

1.1 Motivation

Turbulent boundary layers are defining features of many natural and engineered flows. For example, turbulent boundary layers affect the mass transfer rate in pipes, the drag exerted on automobiles and aircraft and the dispersion of pollutants in the atmosphere. Consequently, a large body of academic research has been devoted to developing an

understanding of the structure and characteristics of the turbulent boundary layer. This research is widely applied for applications such as turbulent boundary layer control, which aims to offer engineering efficiencies through drag reduction, and is fundamental to our understanding of, for example, weather and other atmospheric processes. However, despite significant ongoing research, our understanding of the fundamental structure of the turbulent boundary layer is far from complete.

When viewing the turbulent boundary layer as a whole, the interaction between a turbulent flow and an impermeable bounding surface is commonly dominated by the effects of mean shear. That is, the no-slip condition of the impermeable boundary gives rise to steep velocity gradients in the flow as the velocity components reduce to zero at the boundary. It is these velocity gradients that give rise to the production of turbulent kinetic energy (TKE) which sustains the turbulence within the flow. However, within the turbulent boundary layer, turbulent structure is a result of the local balance of production, transport and dissipation of TKE. The local balance of TKE has been linked to the presence of so-called 'coherent structures'[§] within the turbulent boundary layer (see, for example, Robinson, 1991). As a result, these coherent structures have been extensively studied and documented in order to better understand turbulent boundary layer structure.

However, although extensive support for the presence of coherent structures within the turbulent boundary layer has been reported, the nature of the observed coherent structures has proven to be a controversial topic (for reviews on this topic see, for example, Robinson, 1991; Grass et al., 1991; Adrian, 2007). Common elements of early observations or models of these coherent structures included features, shown in figure 1.1, such as (i) streamwise streaks of high and low speed fluid (low speed and high speed are relative terms, referring to deviations from the mean at that height above the wall); (ii) the presence of arch shaped vortices, referred to using a variety of names, including hairpin and horseshoe vortices; (iii) streaks of fluid intermittently ejecting (or 'bursting') outwards from the boundary towards the edge of the boundary layer. Underpinning many observations and models of these structures was a common feature; their genesis close to the boundary and subsequent growth across the boundary layer thickness. In light of these features, we refer to these models as 'bottom-up' models of the turbulent boundary layer.

However, advances in experimental and computational research resources have enabled ever more comprehensive studies of these structures. That is, the complexity of studying high Reynolds-number flows close to a wall ensured that early studies of turbulent

[§]A generally accepted definition of 'coherent structures' does not appear to be used in the literature; consequently here the term is used to refer to persistent flow patterns which typically occur within the flow over larger spatial extent or timescales than the integral scales of the turbulence (Robinson, 1991). These patterns may be expressed in the form of, for example, a high correlation of a turbulent velocity component with itself or another velocity component.

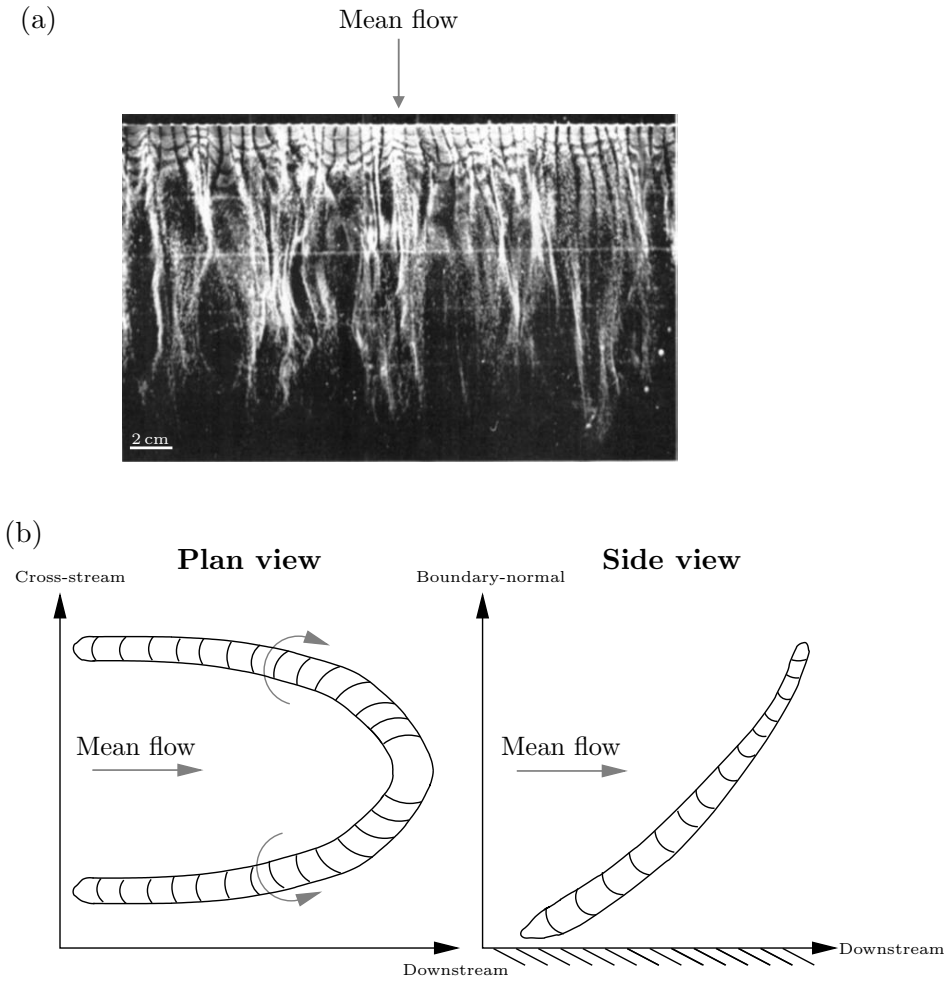


Figure 1.1: (a) Photograph (plan view) of streamwise streaks of high and low speed fluid in a channel, taken from Kline et al. (1967). (b) Schematic of hairpin vortex.

boundary layer structure were limited to the study of relatively low Reynolds-number flows (*i.e.* $Re_\theta \equiv U\theta/\nu \lesssim 5000$, where U denotes the free-stream mean velocity, θ denotes the momentum thickness and ν denotes the kinematic viscosity), where the range in spatial scales is limited but where effective experimental instrumentation and numerical simulation were possible (Robinson, 1991). Conversely, with ongoing advances in research tools it is possible to study increasingly higher Reynolds-number flows in ever increasing detail. Correspondingly, recent research has revealed the presence of larger (as a proportion of boundary-layer thickness) and more complex coherent structures (for recent reviews see, for example Adrian, 2007; Smits et al., 2011). These coherent structures have included packets of hairpin vortices travelling at the same convective velocity, shown in figure 1.2, and very long, narrow regions of low-streamwise-momentum fluid adjacent to regions of higher-momentum fluid.

As our ability to identify coherent structures within the turbulent boundary layer has improved, so too has our understanding of the structure of turbulent boundary

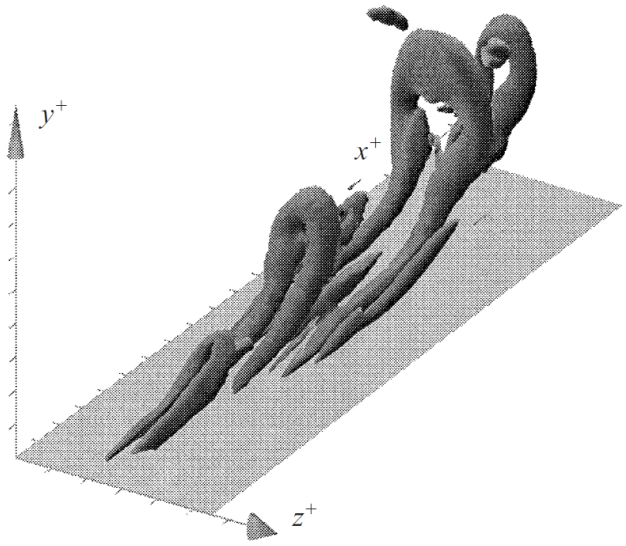


Figure 1.2: Hairpin vortex packet, as computed by Direct Numerical simulation, taken from Zhou et al. (1999).

layer. That is, recent studies have begun to challenge the notion of a 'bottom-up' model of the turbulent boundary layer. In particular, Hunt and Morrison (2000) proposed a 'top-down' model of the turbulent boundary layer applicable for high Reynolds-number flows, whereby the authors emphasised the importance of eddy impingement to the structure of the turbulent boundary layer. That is, the authors proposed that as large scale turbulent eddies within the flow impact onto, and are blocked by, the boundary, they decelerate and are sheared by the mean flow, generating shear layers that grow as the blocked fluid elements are advected downstream by the flow. The shear layers generated by several blocked fluid elements were proposed to interact to eject fluid away from the boundary. A schematic of this model is shown in figure 1.3. The internal shear layers created during this process were proposed to be a source of turbulent energy, which could be transported away from the boundary during the ejection event, and therefore were instrumental in maintaining the structure of the turbulent boundary layer. Support for the 'top-down' model of the turbulent boundary layer has subsequently been reported in a range of studies (see, for example, Hunt and Carlotti, 2001; Carlotti, 2002; Dogan et al., 2016; Tsai et al., 2007), such that a 'top-down' influence on the turbulent fluctuations within the turbulent boundary layer is thought to be dynamically significant (Smits et al., 2011).

However, the model of Hunt and Morrison (2000) was proposed, in part, based upon observations from studies on the interaction of a boundary with turbulence in which there was no mean shear; the effect of turbulence impinging onto a boundary is thought to play the dominant role in giving rise to the turbulent structure in this interaction. That is, in a boundary layer where the mean-flow is not sheared there is no production of

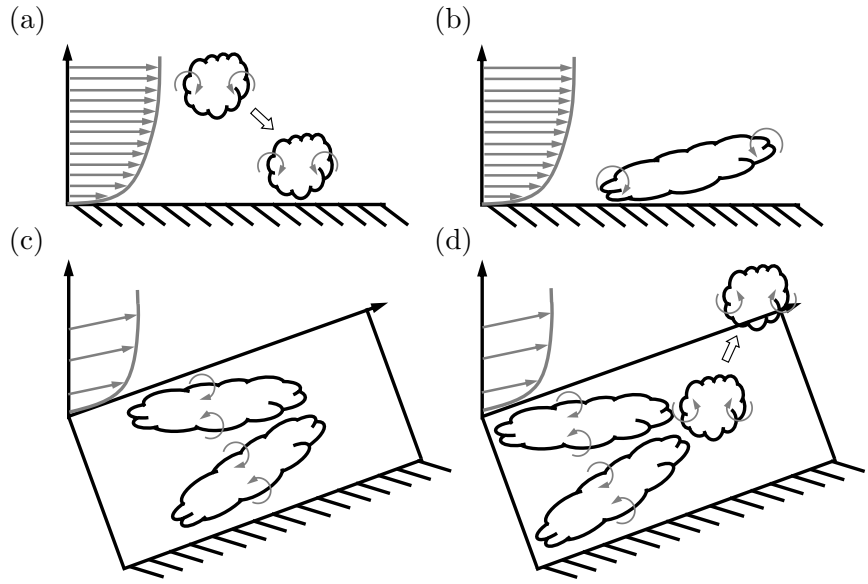


Figure 1.3: Schematic of the 'top-down' turbulent boundary layer model proposed by Hunt and Morrison (2000). (a) Turbulent eddy is blocked by a boundary, (b) the blocked eddy is sheared by the mean flow and the resulting shear layer grows in spanwise and streamwise directions, (c) shear layers from adjacent events interact and (d) cause an ejection away from the boundary.

TKE within the boundary layer and therefore the direct effects of the boundary on the turbulent fluctuations can be isolated. However, the nature of the physical mechanisms that govern this interaction has proven to be a controversial topic (see section 1.2). Consequently, an improved understanding of the nature of this interaction is necessary to underpin key models of turbulent boundary layer structure (such as Hunt and Morrison, 2000); the remainder of this thesis is devoted to the topic of the interaction between zero-mean-shear turbulence and a solid impermeable boundary.

1.2 Previous work

Note that reviews of the literature regarding the interaction of zero-mean-shear turbulence with a boundary are provided in chapters 3 and 4. As a result, only an introduction to the field, sufficient to illustrate the key techniques previously used to study this problem and to highlight some of the controversial aspects of the interaction, is provided here.

The interaction of zero-mean-shear turbulence and a boundary was first studied 50 years ago (Uzkan and Reynolds, 1967). However, despite numerous subsequent studies on this problem, the nature of the dominant physical mechanisms that govern the interaction has proven to be a controversial topic. Much of this controversy can be traced to two key studies in the field; those of Hunt and Graham (1978) and Perot and Moin (1995a). That is, Hunt and Graham (1978) proposed that the interaction was primarily governed by the kinematic blocking condition of the boundary, whereas, in contrast, Perot and

Moin (1995a) proposed that the interaction was primarily governed by viscous dissipative effects. In order to provide context for these proposals it is informative to review the research approaches taken within each study.

Hunt and Graham (1978) developed rapid distortion theory (RDT) to model the interaction of zero-mean-shear turbulence with an impermeable boundary that occurs within a specific flow that was used in early experimental studies (Uzkan and Reynolds, 1967; Thomas and Hancock, 1977) of this problem; the flow generated by a 'moving belt' apparatus, shown schematically in figure 1.4(a). In this flow, homogeneous and isotropic turbulence is generated in a channel using a fixed vertical grid positioned normal to the horizontal mean flow direction. A short distance downstream of the grid the flow interacts with a horizontal wall (*i.e.* a continuous 'belt') that moves at the same speed (and in the same direction) as the mean flow. The turbulence first feels the inhibiting effect of this boundary at the boundary's leading edge and is free to evolve as the flow continues downstream. Note that matching the velocity of the wall to that of the mean flow ensures that when the flow interacts with this boundary the production of TKE is inhibited. The horizontal wall is also assumed to be sufficiently wide that the effects of the side walls of the channel are negligible in a central region of the flow.

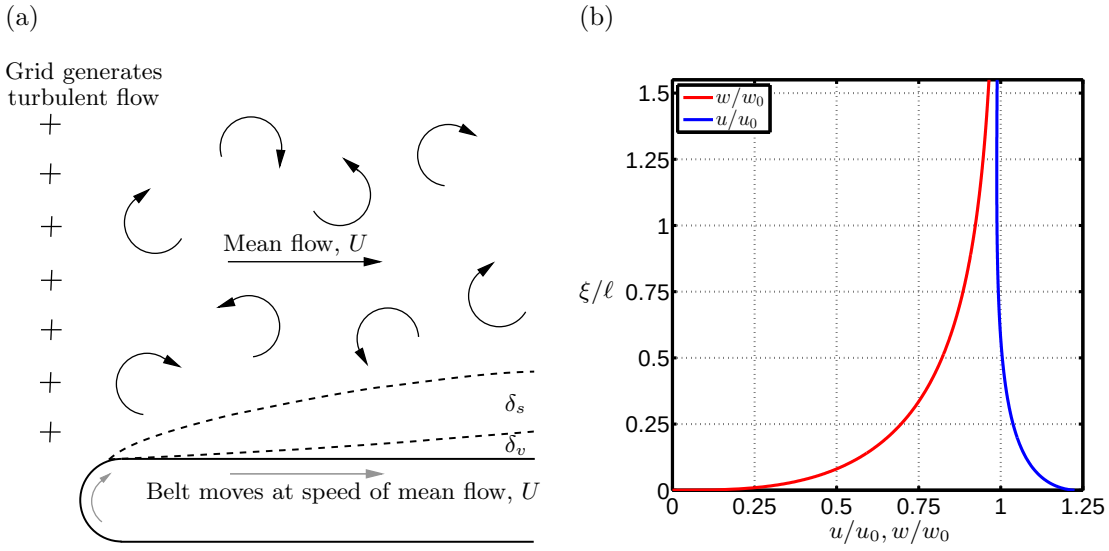


Figure 1.4: (a) Schematic showing the 'moving belt' apparatus used to study the interaction of zero-mean-shear turbulence with a solid impermeable boundary that moves at the same speed (and in the same direction) as the mean velocity of the flow (see, for example, Uzkan and Reynolds, 1967; Thomas and Hancock, 1977). Also shown is the source region δ_s (*i.e.* the boundary-affected region of the flow) and the viscous sublayer δ_v. (b) RDT predictions (Hunt and Graham, 1978) of the rms turbulent velocity components w and u within the source region of a zero-mean-shear turbulent flow, normalised by their expected values in the absence of the boundary w_0 and u_0, against scaled distance above the boundary ξ/ℓ.

In essence, the RDT analysis (Hunt and Graham, 1978) sought to predict the effect of the boundary on the turbulent flow by invoking assumptions that simplified the

Navier-Stokes equations for fluctuating velocity to a set of linear equations. Fourier analysis was used to solve the simplified RDT equations, subject to boundary conditions consistent with the moving belt, which produced energy spectra of the resulting turbulent flow based on an assumed initial spectrum of the undistorted turbulence. Predictions of the effect of the boundary on the root-mean-square (rms) turbulent velocity components were obtained by integrating the distorted energy spectra across the wavenumber space. Within the RDT analysis, the region of flow influenced by the boundary was split into two distinct layers; an outer inviscid layer, denoted the source region, and an inner viscous layer. That is, the kinematic blocking condition was thought to directly inhibit the flow over the source region but viscous effects were assumed to be constrained to the inner viscous layer. Within the source region, boundary-tangential turbulent velocities were found to be amplified and the boundary-normal turbulent velocities were reduced, as shown in figure 1.4(b). (Note that u/u_0 and w/w_0 denote the magnitude of the boundary-tangential and boundary-normal rms turbulent velocity components, respectively, normalised by their expected values in the absence of the boundary, ξ denotes distance above the boundary and ℓ denotes the longitudinal integral length scale of the boundary-tangential turbulent velocity component.) That is, in order to preserve continuity, suddenly imposing the wall-blocking condition (at the leading edge of the boundary) gave rise to pressure increases and a redistribution of TKE from the boundary-normal rms turbulent velocity component to the boundary-tangential turbulent velocity components. In contrast, in the viscous sublayer all components of the turbulent velocity reduced to zero (Hunt and Graham, 1978).

However, the distinct two-layer structure of the boundary layer was a critical assumption of the RDT analysis. That is, Hunt and Graham (1978) conducted their analysis under the assumption that the turbulent flow considered was at sufficiently high Reynolds number that, beyond the viscous sublayer, viscous effects could be ignored over short times following boundary insertion. However, this assumption (that viscous effects could be ignored in the source layer) implies that the theory may be valid only for short times after boundary insertion, over which the turbulence does not decay significantly. In spite of this, Hunt and Graham (1978) proposed that the RDT predictions could still describe the subsequent development of the flow following boundary insertion if local values of undistorted turbulence were used for scaling.

In contrast, Perot and Moin (1995a) used Direct Numerical Simulation to determine the effect of instantaneously inserting an infinite flat impermeable boundary into an established turbulent flow that was statistically homogeneous and isotropic with zero mean-flow. The instantaneous effect of rapidly inserting the boundary was to alter the turbulent field in a thin region close to the boundary, in which the resulting turbulence was inhomogeneous and anisotropic, shown in figure 1.5. Following this, a short 'developing state' occurred in which the flow adjusted to the rapid change to inhomogeneity.

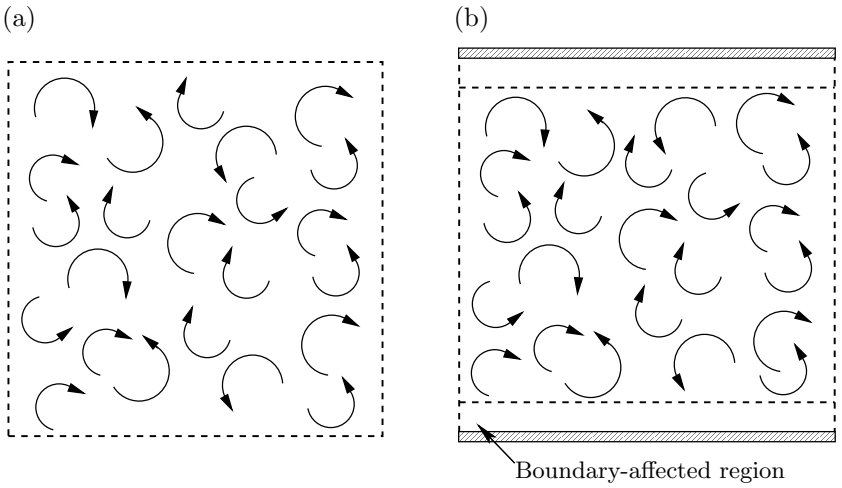


Figure 1.5: Schematic showing an idealised interaction of zero-mean-shear turbulence with a solid impermeable boundary; an initially homogeneous isotropic turbulent field with zero mean-flow, shown in (a), interacts with an infinite flat impermeable boundary that is instantaneously inserted into the flow, giving rise to a boundary-affected region of the flow, shown in (b).

Throughout this process the boundary did not produce any new turbulence since there were no mean velocity gradients within the flow. Measurements of the evolution of the flow, as it occurred in time, could be compared to predictions or measurements of the evolution of the flow at distances downstream of the leading edge of the 'moving belt' configuration through invoking Taylor's frozen turbulence hypothesis (Perot and Moin, 1995a).

Perot and Moin (1995a) reported that during boundary insertion the boundary-tangential turbulent velocities were amplified and the boundary-normal turbulent velocities were reduced, in accordance with the predictions of Hunt and Graham (1978), as shown in figure 1.6. However, following boundary insertion the peak in the boundary-tangential turbulent velocity components was rapidly dissipated, also shown in figure 1.6, which was attributed to viscous effects. That is, Perot and Moin (1995a) argued that as the flow developed in response to boundary insertion an intercomponent energy transfer still occurred from the boundary-normal to the boundary-tangential turbulent velocity components, but they argued that this was not a net transfer of energy and rather described a viscous dissipative effect. This was explained in the context of a model of 'splats' and 'antisplats'. Here a 'splat' can be considered to be a conceptualised element of fluid that is blocked as it travels towards the boundary; the blocking of these fluid elements results in high instantaneous dynamic pressure and a corresponding transfer of energy from the boundary-normal velocity component to the boundary-tangential velocity components (Perot and Moin, 1995a). The collision of fluid elements travelling tangential to the boundary was proposed to give rise to similar events, so-called 'antisplats', in which the collision of elements results in high instantaneous dynamic pressure and a transfer of

energy from boundary-tangential velocity components to the boundary-normal velocity component as the fluid elements eject from the boundary. If the fluid were inviscid, these events could occur without loss of TKE, such that there would be little intercomponent energy transfer on average. However, Perot and Moin (1995a) proposed that antisplats were, on average, less energetic than splats as a result of the viscous dissipation of TKE from fluid elements as they travel close to the boundary. Thus, Perot and Moin (1995a) proposed that although an energy transfer occurred, this energy transfer did not describe a net transfer of energy from the boundary-normal velocity component to the boundary-tangential velocity components, as the energy was dissipated. As a result, Perot and Moin (1995a) proposed that following boundary-insertion there would be no amplification of the boundary-tangential velocity components, relative to their expected values in the absence of the boundary, within the boundary-affected region of the flow. The idea that the strength of viscous effects governs the level of splat-antisplat imbalance, and hence energy transfer, is notably different from the ideas of Hunt and Graham (1978) that energy transfer was governed by a kinematic blocking condition.

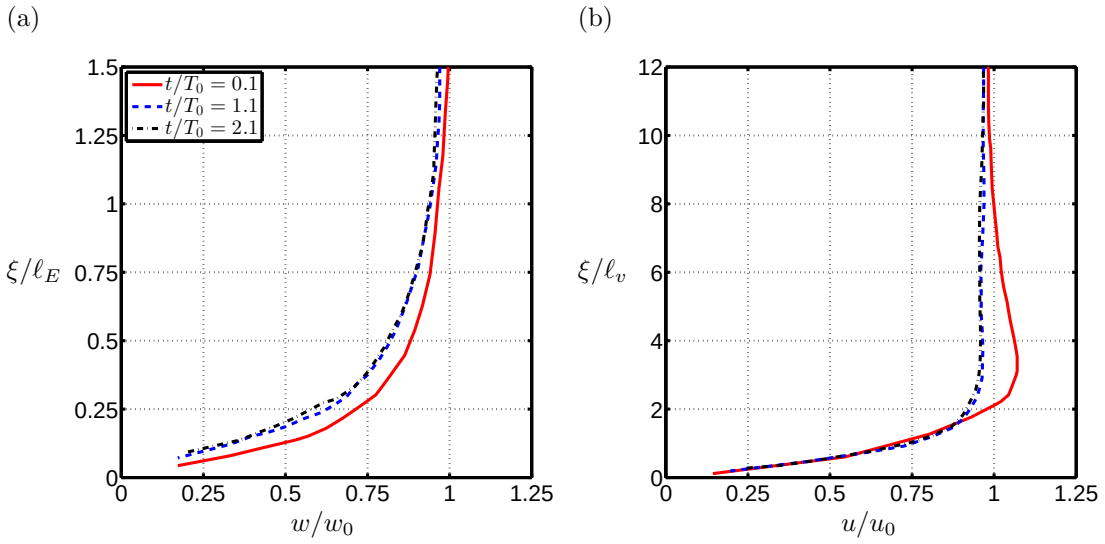


Figure 1.6: Measurements of (a) the boundary-normal rms velocity component w and (b) the boundary-tangential rms velocity components u reported by Perot and Moin (1995a), normalised by their expected values in the absence of the boundary w_0 and u_0, against distance above the boundary ξ. The distance above the boundary has been scaled in order to collapse the data; in (a) a measure of the size of energy-containing turbulent eddies ℓ_E within the flow has been used for scaling [$\ell_E \equiv q^3/\varepsilon, q^2$ denotes TKE and ε denotes turbulent dissipation rate], in (b) a viscous length-scale ℓ_v has been used for scaling [$\ell_v \equiv (t\nu)^{0.5}, \nu$ denotes kinematic viscosity, t denotes time following boundary insertion]. Results shown correspond to measurements taken at different times t (as a proportion of eddy turnover time T_0) following boundary insertion [see legend in (a), which applies to both plots].

Results from a range of other related studies have done little to clarify this conflict relating to the governing mechanisms. That is, results from a range of experimental

and numerical studies (see, for example, Thomas and Hancock, 1977; Biringen and Reynolds, 1981; Hannoun et al., 1988; Aronson et al., 1997; Bodart et al., 2010), indicate that the boundary-normal turbulent velocity component is inhibited by the boundary in accordance with the RDT proposed by Hunt and Graham (1978). In addition, some studies have reported that as the flow develops following boundary-insertion, the boundary-tangential rms turbulent velocity components remain amplified, relative to their values in the absence of the boundary, in qualitative accordance with RDT (see, for example, Thomas and Hancock, 1977; Biringen and Reynolds, 1981; Hannoun et al., 1988). However, other studies have reported that the amplification of the boundary-tangential rms turbulent velocity components dissipates within a period of several eddy turnover times after boundary insertion (or at short distances downstream of the leading edge of the boundary). In this case, the flow has been reported to approach a state where u/u_0 is monotonically reduced within the boundary-affected region (see for example Aronson et al., 1997; Bodart et al., 2010), in accordance with the results of Perot and Moin (1995a). Although explanations for these conflicting results have been proposed in light of limitations of the experimental, numerical or theoretical techniques used in individual studies (see, for example Perot and Moin, 1995a; Aronson et al., 1997; Löfdahl et al., 1998), a physical mechanism able to consistently explain the reported variations between previous studies has not been proposed. Indeed, despite ongoing research into the validity of the models of Hunt and Graham (1978) and Perot and Moin (1995a) (see, for example, Hunt, 1984; Magnaudet, 2003), each model remains contentious.

Previously, results obtained from studying the interaction of zero-mean-shear turbulence and an impermeable boundary have also been compared to the results obtained from studies using oscillating-grid turbulence (OGT); a flow produced by the oscillation of a planar grid within a cuboidal tank of water (see, for example, Thompson and Turner, 1975; Hopfinger and Toly, 1976). In this experimental apparatus, under ideal conditions, the turbulence produced is thought to be approximately homogeneous and isotropic in planes parallel to the grid, with negligible mean flow sufficiently far beneath the oscillating grid (De Silva and Fernando, 1994). The negligible mean flow results in negligible production of TKE when the flow interacts with a boundary below the oscillating grid, such that the flow can be considered to approximate zero-mean-shear conditions (McDougall, 1979; Kit et al., 1997). The turbulence is, however, inhomogeneous in planes normal to the grid; that is, the rms turbulent velocity components decay with increasing distance normal to the grid (Hopfinger and Toly, 1976). Hence, when the flow interacts with a horizontal boundary placed parallel to and below a horizontal oscillating grid, the boundary induced effects are superimposed onto pre-existing inhomogeneity in the boundary-normal direction (Brumley and Jirka, 1987). A schematic of this flow is shown in figure 1.7.

In previous studies using OGT, the boundary-normal turbulent velocity component

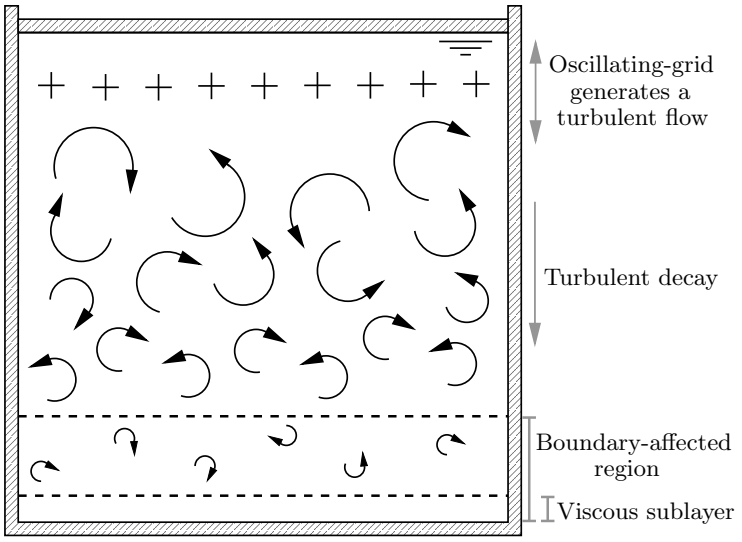


Figure 1.7: Schematic showing the 'oscillating-grid turbulence' apparatus used to study the interaction of approximately zero-mean-shear turbulence with a solid impermeable boundary positioned parallel to the oscillating-grid. Also shown is the boundary-affected region of the flow and the viscous sublayer.

has been found to be reduced and the boundary-tangential turbulent velocity components have typically been found to be amplified in the boundary-affected region (Hannoun et al., 1988; Kit et al., 1997; Brumley and Jirka, 1987) in qualitative accordance with RDT predictions (Hunt and Graham, 1978; Hunt, 1984). In contrast, McDougall (1979) reported measurements of the boundary-tangential turbulent velocity components that were monotonically reduced by the boundary, in qualitative accordance with the results of Perot and Moin (1995a). However, in contrast to the previous approaches discussed, these measurements describe a statistically stationary flow and do not describe the initial evolution of a turbulent flow in response to the insertion of a boundary. Thus the measurements obtained using OGT are complimentary to those obtained using the other approaches discussed, rather than equivalent to them. Thus, it is perhaps unexpected that the majority of results obtained using this apparatus exhibit good agreement with RDT predictions (Hunt, 1984; Hunt and Graham, 1978), given that the RDT predictions were proposed initially in the context of rapid-boundary-insertion.

In addition to this result, the nature of the flow produced by OGT causes additional uncertainty when comparing the results obtained using OGT to those from other studies of the interaction of zero-mean-shear turbulence with a boundary. That is, in OGT the spatial decay of the turbulent velocity components normal to and away from the grid not only means that the boundary-induced effects are superimposed onto pre-existing inhomogeneity in the boundary-normal direction but it also gives rise to a vertical flux of TKE towards the boundary (Hannoun et al., 1988). In addition, in a departure from ideal models of OGT, measurements from experiments indicate that the magnitude of

mean flow velocity components can approach the magnitude of the root-mean-square turbulent velocity fluctuations (McKenna and McGillis, 2004) such that the flow may exhibit some mean-shear close to the boundary. The effects that these features have on the interpretation of the results obtained from OGT, in comparison to studies in zero-mean-shear turbulence, has yet to be fully explored. That is, previous studies utilising OGT to investigate this problem were limited by experimental measurement techniques that did not enable spatially-resolved measurements of the flow. Consequently, a thorough analysis of the dominant physical mechanisms that govern the interaction, through, for example, estimating terms of the Reynolds stress transport equations, was not possible. As such, further analysis of the data obtained from studies utilising OGT may offer new insight into the physical mechanisms that govern the interaction of approximately zero-mean-shear turbulence a solid impermeable boundary.

1.3 Objectives and approach

The overall aim of this project was to study experimentally the interaction of OGT with a solid impermeable boundary in order to provide further insight into the mechanisms that govern the interaction of zero-mean-shear turbulence and a boundary. To this end, the structure of the flow produced by OGT was first examined (chapter 2) using spatially resolved measurement techniques (two-dimensional planar particle imaging velocimetry), in order to investigate the limitations inherent in using this apparatus to approximate zero-mean-shear conditions. Then the interaction of OGT with a solid impermeable boundary was studied using the same spatially resolved measurement techniques. This work aimed to (i) quantify the effect of the boundary on the rms turbulent velocity components (chapter 3); (ii) derive insight into the dominant physical mechanisms that govern the interaction of OGT and a solid impermeable boundary (chapters 3 and 4); (iii) interpret these results in the context of existing models of the interaction of zero-mean-shear turbulence and a solid impermeable boundary (chapters 3 and 4). In particular, this work aimed to determine if the interaction was principally governed by the kinematic blocking condition of the boundary (as per Hunt and Graham, 1978) or viscous dissipative effects (as per Perot and Moin, 1995a) and thereby investigate the validity of well-established models of the interaction (Hunt and Graham, 1978; Perot and Moin, 1995a). In addition, this research aimed to identify any additional physical mechanisms that govern the interaction of approximately zero-mean-shear turbulence and boundaries and which may provide an explanation for the disparity in previously reported measurements relating to this problem.

References

Adrian, R. J. (2007). Hairpin vortex organisation in wall turbulence. *Phys. Fluids*, 19:041301.

Aronson, D., Johansson, A. V., and Löfdahl, L. (1997). Shear-free turbulence near a wall. *J. Fluid Mech.*, 338:363–395.

Biringen, S. and Reynolds, W. C. (1981). Large-eddy simulation of the shear-free turbulent boundary layer. *J. Fluid Mech.*, 103:53–63.

Bodart, J., Cazalbou, J. B., and Joly, L. (2010). Direct numerical simulation of unsheared turbulence diffusing towards a free-slip or no-slip surface. *J. Turbul.*, 11(48):1–18.

Brumley, B. H. and Jirka, G. H. (1987). Near-surface turbulence in a grid-stirred tank. *J. Fluid Mech.*, 183:235–263.

Carlotti, P. (2002). Two-point properties of atmospheric turbulence very close to the ground: comparison of a high resolution LES with theoretical models. *Boundary-Layer Meteorol*, 104:381–410.

De Silva, I. P. D. and Fernando, H. J. S. (1994). Oscillating grids as a source of nearly isotropic turbulence. *Phys. Fluids*, 6:2455–2464.

Dogan, E., Hanson, R. E., and Ganapathisubramani, B. (2016). Interactions of large-scale free-stream turbulence with turbulent boundary layers. *J. Fluid Mech.*, 802:79–107.

Grass, A. J., Stuart, R. J., and Mansour-Tehrani, M. (1991). Vortical structures and coherent motion in turbulent flow over rough and smooth boundaries. *Phil. Trans. R. Soc. Lond.*, 336:35–65.

Hannoun, I. A., Fernando, H. J. S., and List, E. J. (1988). Turbulence structure near a sharp density interface. *J. Fluid Mech.*, 189:189–209.

Hopfinger, B. J. and Toly, J. A. (1976). Spatially decaying turbulence and its relation to mixing across density interfaces. *J. Fluid Mech.*, 78(1):155–175.

Hunt, J. C. R. (1984). Turbulence structure in thermal convection and shear-free boundary layers. *J. Fluid Mech.*, 138:161–184.

Hunt, J. C. R. and Carlotti, P. (2001). Statistical structure at the wall of the high Reynolds number turbulent boundary layer. *Flow Turbul. Combust*, 66:453–475.

Hunt, J. C. R. and Graham, J. M. R. (1978). Free-stream turbulence near plane boundaries. *J. Fluid Mech.*, 84(2):209–235.

Hunt, J. C. R. and Morrison, J. F. (2000). Eddy structure in turbulent boundary layers. *Eur. J. Mech. B - Fluids*, 19:679–694.

Kit, E. L. G., Strang, E. J., and Fernando, H. J. S. (1997). Measurement of turbulence near shear-free density interfaces. *J. Fluid Mech.*, 334:293–314.

Kline, S. J., Schraub, W. C., and Runstadler, P. W. (1967). The structure of turbulent boundary layers. *J. Fluid Mech.*, 30(4):741–773.

Löfdahl, L., Johansson, A. V., and Andersson, C. (1998). The influence of temperature on the measurements of Reynolds stresses in shear free turbulence near a wall. *Exp. Fluids*, 25:160–164.

Magnaudet, J. (2003). High-Reynolds-number turbulence in a shear-free boundary layer: revisiting the Hunt-Graham theory. *J. Fluid Mech.*, 484:167–196.

McDougall, T. J. (1979). Measurements of turbulence in a zero-mean-shear mixed layer. *J. Fluid Mech.*, 94(3):409–431.

McKenna, S. P. and McGillis, W. R. (2004). Observations of flow repeatability and secondary circulation in an oscillating grid-stirred tank. *Phys. Fluids*, 16(9):3499–3502.

Perot, B. and Moin, P. (1995). Shear free turbulent boundary layers, Part 1, physical insights into near-wall turbulence. *J. Fluid Mech.*, 295:199–227.

Robinson, S. K. (1991). Coherent motions in the turbulent boundary layer. *Annu. Rev. Fluid Mech.*, 23:601–639.

Smits, A. J., McKeon, B. J., and Marusic, I. (2011). High-Reynolds number wall turbulence. *Annu. Rev. Fluid Mech.*, 43:353–375.

Thomas, N. H. and Hancock, P. E. (1977). Grid turbulence near a moving wall. *J. Fluid Mech.*, 82(3):481–496.

Thompson, S. M. and Turner, J. S. (1975). Mixing across an interface due to turbulence generated by an oscillating grid. *J. Fluid Mech.*, 67(2):349–368.

Tsai, Y. S., Hunt, J. C. R., Nieuwstadt, F. T. M., Westerweel, J., and Gunasekaran, B. P. N. (2007). Effect of strong external turbulence on a wall jet boundary layer. *Flow Turbul. Combust*, 79:155–174.

Uzkan, T. and Reynolds, W. C. (1967). A shear-free turbulent boundary layer. *J. Fluid Mech.*, 28(4):803–821.

Zhou, J., Adrian, R. J., Balachandar, S., and Kendall, T. M. (1999). Mechanisms for generating coherent packets of hairpin vortices in channel flow. *J. Fluid Mech.*, 387:353–396.

Chapter 2

A method for reducing mean flow in oscillating-grid turbulence

This chapter is comprised of an article currently in preparation for submission. Article reference:

> McCorquodale, M. W. and Munro, R. J. (2017). A method for reducing mean flow in oscillating-grid turbulence. ***In preparation for:*** *Experiments in Fluids*.

For ease of the reader the following amendments to the structure of the paper have been included:

1. Section and figure numbers are amended to include a chapter reference to ensure consistency across the thesis.
2. Contact details for corresponding authors have not been included
3. Footnotes are included to facilitate references to other chapters of the thesis

Nomenclature

C_1, C_2, C_3	Empirical constants
f	Grid oscillation frequency
H	Inner box height
ℓ	Longitudinal integral length scale
L	Half-width of inner box
M	Mesh spacing
$p, \overline{p}, p'$	Instantaneous/(time-averaged) mean/fluctuating pressure
$Re \equiv MSf/\nu$	Grid Reynolds number
r_u, c_u	Autocorrelation functions
S	Grid stroke
t	Time
T	Sampling period (4 minutes)
u_i	Instantaneous velocity component
$u_i' \equiv u_i - \overline{u}_i$	Turbulent velocity component
$\overline{u}_i$	(Time-averaged) mean velocity component
U_i	(Ensemble-averaged) mean velocity component
$\overline{u_i'^2}^{1/2}$,	Root-mean-square turbulent velocity component
x_1, x_2, x_3	Co-ordinate system with origin at center of grid's mean position
$x_{3,k}$	Vertical displacement of the grid with respect to $x_3 = 0$
ζ	Half width of outer or inner box
η	Kolmogorov length scale
ν	Kinematic viscosity
ρ	Density
$\sigma_{u_i'}$	Standard deviation associated with repeated measurements of $\overline{u_i'^2}^{1/2}$ under nominally identical conditions
χ	Variable denoting spatial lag used within autocorrelation analysis
ω_i	Instantaneous vorticity component
$\overline{\omega}_i$	(Time-averaged) mean vorticity component
Ω_i	(Ensemble-averaged) Mean vorticity component
A_{ij}^d	Transport due to the mean flow
Φ_{ij}	Production due to the mean flow
T_{ij}	Transport by velocity fluctuations
Π_{ij}^d	Transport by pressure fluctuations
D_{ij}	Molecular diffusion
ε_{ij}	Viscous dissipation

$\overline{p}$	Time-average of quantity p
$\lvert p \rvert$	Magnitude of quantity p
$\langle p \rangle_i$	Spatial average of quantity p in the ith direction

A method for reducing mean flow in oscillating-grid turbulence

Mark W. McCorquodale[1] and R. J. Munro[1]

[1]Faculty of Engineering, The University of Nottingham, Nottingham NG7 2RD, UK

Oscillating-grid turbulence (OGT) is an experimental tool that has been widely used to study the role of turbulent fluctuations under conditions of small mean flow. We report experiments to investigate the structure of the turbulent flow produced by an oscillating grid, using velocity measurements obtained through the application of two-dimensional particle image velocimetry in the vertical plane through the centre of the grid. Ensemble averages of the fluid velocity measurements at specific stages of the grid's oscillation indicate that mean flow is induced in OGT by the merging of grid-induced jets close to the tank sidewalls. The installation of an open-ended 'inner box' (with its top edge positioned just below the bottom of the grid's oscillation) is shown to inhibit the merging of the jets, thereby resulting in a reduction in the magnitude of the mean flow within the interior of the inner-box region. Field measurements of the time-averaged root-mean-square turbulent velocity components and the time-averaged turbulent kinetic energy flux indicate that the installation of the inner box results in turbulence that is in good agreement with the well-established models of OGT across the central 50% of the inner box's width, but that distinct anisotropic regions exist adjacent to the vertical sidewalls. We anticipate that this simple amendment to reduce the mean flow present in OGT can be readily used in future work that utilises OGT to isolate the effects of turbulent fluctuations from those of the mean flow.

2.1 Introduction

Oscillating-grid turbulence (OGT) has been used extensively over the last 50 years as an experimental tool to study the role of turbulent fluctuations. The typical set-up consists of a planar grid, with uniform mesh spacing M, positioned horizontally inside a water-filled container and made to oscillate vertically with frequency f and stroke S. The grid's oscillatory motion produces stationary turbulence that decays spatially in the grid-normal direction, but is approximately homogeneous in planes parallel to the grid, with mean-flow velocity components that are small in magnitude compared to the fluctuations. It is this approximate 'zero-mean-shear' property that has resulted in OGT being used to investigate a broad range of problems, which include the study of turbulent entrainment across a density interface (Turner, 1968; Hopfinger and Toly, 1976; McDougall, 1979; Hopfinger and Linden, 1982; Fernando and Long, 1983, 1985;

Xuequan and Hopfinger, 1986; Nokes, 1988; Hannoun and List, 1988; McGrath et al., 1997), particle coagulation and particle suspension (Brunk et al., 1998; Huppert et al., 1995; Medina et al., 2001; Masalo et al., 2008; Wan Mohtar and Munro, 2013), the growth and collapse of a turbulent front (Honey et al., 2014; De Silva and Fernando, 1998), and the inhibiting effect of boundaries on turbulence, including free surfaces (Brumley and Jirka, 1987), density interfaces (Hannoun et al., 1988; Kit et al., 1997) and impermeable boundaries (Hannoun et al., 1988; McCorquodale and Munro, 2017a)¶.

The widespread use of OGT has resulted in the properties of the turbulence produced being studied extensively and a standard model to describe OGT has been developed. For a grid made of bar elements with square cross-section, the turbulence produced can be described by (McDougall, 1979; Hopfinger and Toly, 1976; Brumley and Jirka, 1987; Fernando and De Silva, 1993)

$$(\overline{u_1'^2})^{1/2} = C_1 M^{1/2} S^{3/2} f x_3^{-1}, \tag{2.1a}$$

$$(\overline{u_3'^2})^{1/2} = C_2 (\overline{u_1'^2})^{1/2}, \tag{2.1b}$$

$$\overline{\ell} = C_3 x_3, \tag{2.1c}$$

where x_3 denotes the grid-normal direction, $\overline{\ell}$ is the time-averaged integral length scale, and $(\overline{u_1'^2})^{1/2}$, $(\overline{u_2'^2})^{1/2}$ and $(\overline{u_3'^2})^{1/2}$ are the time-averaged root-mean-square (rms) velocity components. The symmetry of the grid means that $(\overline{u_1'^2})^{1/2} \approx (\overline{u_2'^2})^{1/2}$ is assumed. Typical values previously reported for the empirical coefficients are $C_1 = 0.2$ to 0.5, $C_2 = 1.1$ to 1.4 and $C_3 = 0.1$ to 0.25 (Thompson and Turner, 1975; Hopfinger and Toly, 1976; McDougall, 1979; Hopfinger and Linden, 1982; De Silva and Fernando, 1994; Kit et al., 1997). This model was derived (for example see Hopfinger and Toly, 1976) from the transport equation for turbulent kinetic energy (TKE) under the simplifying assumptions of zero mean flow, homogeneity (in planes parallel to the grid) and negligible viscous transport. We stress, however, that the model is only valid sufficiently far from the grid (typically, for $x_3 \gtrsim 2.5M$). Close to the grid (*i.e.*, for $|x_3| \lesssim 2.5M$, henceforth referred to as the 'near-grid region'), jets form in the wake of the grid elements resulting in a flow field in the near-grid region characterised by the presence of energetic, mesh-size coherent vortex structures that interact and breakdown as they are advected away from the grid. However, beyond the near-grid region (*i.e.*, for $x_3 \gtrsim 2.5M$, henceforth referred to as the 'turbulent-diffusive region') the jet structures have broken down and the flow is characterised by fluctuations that are large compared to mean-flow components, which decay in the grid-normal direction (x_3) in a way that is well-approximated by equation (2.1).

However, that is not to say the mean flow is not an important factor to consider when using OGT (or when designing OGT apparatus). Although the mean velocity components are typically assumed to be small compared the rms fluctuations, the mean

¶N.B. McCorquodale and Munro (2017a) is shown in chapter 3

flow is not completely negligible. As a result, several studies have attempted to analyse the mean flow (McDougall, 1979; Hopfinger and Toly, 1976; Fernando and De Silva, 1993; McKenna and McGillis, 2004; Drayton, 1993), resulting in a number of conditions on the oscillating-grid mechanism that should be satisfied to minimise the mean flow. The conditions specified include the use of a grid oscillation frequency f less than 7 Hz (McDougall, 1979) and a grid solidity less than 40% (Hopfinger and Toly, 1976). Under these conditions Fernando and De Silva (1993) reported typical values for the 'mean flow intensity' (here used to denote the ratio of mean flow velocity component to the rms velocity component) of approximately 1.3 when using a grid constructed with a square perimeter edge, but that this ratio could be reduced to as low as 0.1 by designing the grid with edge conditions such that the tank side walls act as a plane of reflective symmetry to the grid. However, it has also been reported that even in studies that meet these criteria, including the symmetry condition of the grid design, that the ratio of mean flow intensity can approach unity and that the magnitude of the mean flow can vary by as much as 25% between consecutive experiments conducted under nominally identical conditions (McKenna and McGillis, 2004).

Drayton (1993) proposed that a mean flow is induced in OGT when there is a significant difference in the relative strength of the jets produced by the oscillating grid in different regions of the tank, and suggested the Coanda effect to be the dominant mechanism for this. Here, the term 'Coanda effect' is used to describe the tendency of a jet flowing parallel to a boundary to shift its axis closer to the boundary, as a result of reduced entrainment on the boundary-side of the jet (Sawyer, 1960; Kim et al., 1996; Song et al., 2000; Miozzi et al., 2010; Di Marco et al., 2015). Drayton (1993) argued that, with OGT, a jet produced by the outermost grid elements is drawn onto the tank sidewall by the Coanda effect, preventing a symmetric growth of the jet about its axis. As a result, the jet's growth is inhibited in the wall-normal direction, with a comparatively greater spread of the jet in the wall-tangential direction, meaning that edge jets are more likely to merge with each other than jets produced closer to the centre of the grid. Drayton (1993) also proposed that the merged edge jets are more energetic than those produced close to the centre of the grid, and so do not necessarily breakdown within the near-grid region, giving rise to a more intense mean flow adjacent to the tank sidewalls, which results in large-scale circulations throughout the tank's interior. In the experiments reported by Drayton (1993), the merged edge jets were observed to have a wall-normal thickness of about two mesh lengths (*i.e.*, $2M$).

Previous studies (Hopfinger and Toly, 1976; Dickinson and Long, 1983) have suggested the use of an open-ended 'inner box', positioned symmetrically below the grid, can reduce large-scale circulations present in the tank that contribute significantly to the mean flow. Moreover, Drayton (1993) proposed (in the absence of supporting data) that the installation of an inner box could reduce large-scale circulations induced by the Coanda

effect, but in order for the inner box to be effective in reducing the mean flow it should be positioned with its top edge below the near-grid region (*i.e.*, below $x_3 \approx 2.5M$), otherwise it was argued that the Coanda mechanism would also act within the inner box itself.

However, experimental data analysing how the presence of an inner box reduces mean flow, or the extent of any reduction, has not previously been reported. Therefore, this paper analyses the mean flow produced by OGT and shows how the installation of an inner box, positioned symmetrically below the grid, can be used to significantly reduce the mean flow present in OGT, such that turbulence produced is better described by the standard model (*i.e.*, equation 2.1). In section 2.2 we describe the OGT apparatus used and the application of particle image velocimetry (PIV) to acquire data-sets for both the near-grid and turbulent-diffusive regions. Measurements of the mean flow are presented in section 2.3, in which ensemble-averages are used to determine the statistical properties of the flow in the near-grid region, at different stages during the grid's oscillation, and time-averages are used to determine the flow statistics in the turbulent-diffusive region. Measurements of turbulent statistics are also presented, including the time-averaged rms velocity components $(\overline{u_1'^2})^{1/2}$ and $(\overline{u_3'^2})^{1/2}$, degree of isotropy $(\overline{u_3'^2})^{1/2}/(\overline{u_1'^2})^{1/2}$ and turbulent energy flux, which illustrate the effects of both tank side walls and mean flow intensity on the turbulence statistics. Limitations in the use of an inner box are discussed in section 2.4 and conclusions are made in section 2.5.

2.2 Experiments

2.2.1 Apparatus & Set-up

A schematic view of the experimental set-up is shown in figure 2.1, which is similar to those widely used in previous studies (see for example Brumley and Jirka, 1987; Dickinson and Long, 1983; Thompson and Turner, 1975; Hopfinger and Linden, 1982; De Silva and Fernando, 1994; Kit et al., 1997). The experiments were conducted in a transparent container with internal dimensions 35.2 cm × 35.2 cm × 50.0 cm, henceforth referred to as the 'outer box' (see figure 2.1). A rigid lid was suspended horizontally, 2.0 cm below the top of the outer box, which was filled, to the height of the lid's underside, with a salt-water solution of uniform density $\rho = 1.028\,\mathrm{g/cm^3}$ (*i.e.* the total water depth was 48.0 cm). The salt used was NaCl. We note here that the salt-water solution was required to make the seeding particles used for the PIV technique neutrally buoyant (the PIV technique is discussed in more detail in Section 2.2.2).

A planar grid was attached to the base of a drive shaft (of 1 cm diameter) and suspended inside the outer box with the plane of the grid horizontal (see figure 2.1a). The drive shaft passed through a circular hole of 2.6 cm diameter in the centre of the lid. With the grid in its neutral position (*i.e.*, the position shown in figure 2.1a) its

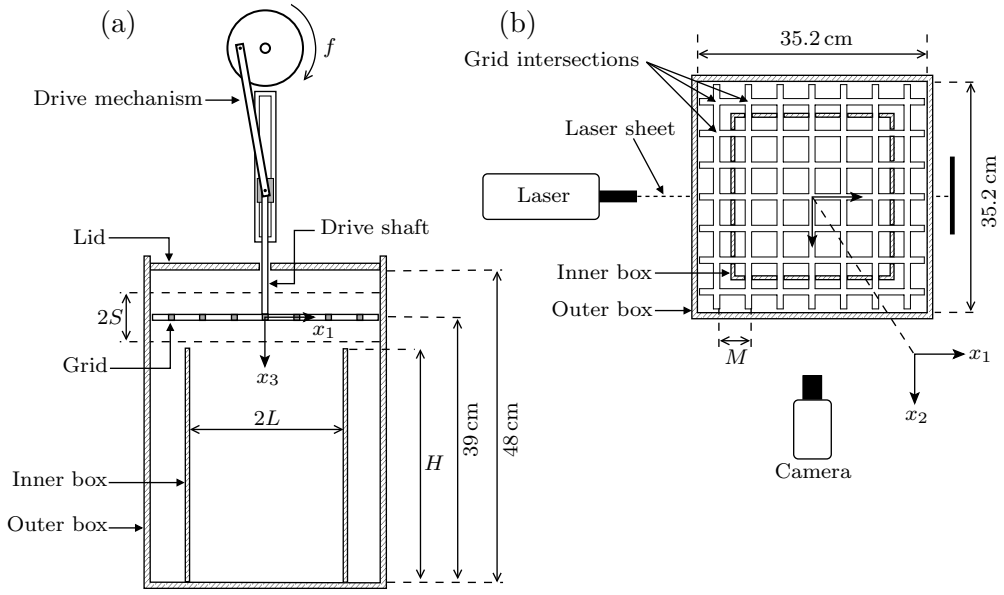


Figure 2.1: Sketches showing the key components of the experimental set-up. (a) A side view showing the positioning of the reciprocating drive mechanism, the horizontal grid and the inner and outer boxes. (b) A plan view showing the position of the inner box relative to the grid's mesh, and the position of the camera relative to the vertical light-sheet produced by the laser. Also shown are the coordinate directions (x_1, x_2, x_3). The set-up shown corresponds to the experiments labelled 'B' in Table 2.1.

mid-plane was a height 39.0 cm above the base of the outer tank. The vertical oscillatory motion of the shaft and grid was driven by using a cam and linear bearing to convert the rotary motion of a motorised flywheel to reciprocating vertical motion of the drive shaft, as shown in figure 2.1(a). The grid's oscillation frequency (f) was controlled using a potentiometer and a single fixed stroke of $S = 2.5$ cm was used throughout (here, the stroke is defined as being equal to the amplitude of the grid's motion). The grid was fabricated from stainless steel bars (of square cross-section, 1.0 cm $\times$ 1.0 cm) joined together to form a 7×7 regular array with a uniform mesh spacing $M = 5.0$ cm. The corresponding solidity of the grid was 36.4%. Figure 2.1(b) shows a plan view of the grid. The edge conditions were chosen so that the tank sidewalls were planes of symmetry, although a narrow clearance of approximately 0.3 cm was required between the grid's perimeter and the internal sidewalls of the outer box. It is convenient here to define terminology that will be used throughout to denote key features of the grid: we use 'grid intersections' to denote where grid elements cross (as illustrated in figure 2.1b) and 'mid-points' as being those points on the grid that are equidistant between two adjacent grid intersections.

During initial tests to determine the effect the installation of an inner box has on the turbulence and mean-flow characteristics, consideration was given to the size and positioning of the inner box. It was found that a significant reduction in the magnitude

of the mean-flow components could be obtained using a cuboid, open-ended inner box, fixed to the base of the outer box and positioned centrally with the vertical sidewalls of the inner box equidistant between the outermost and second-outermost grid intersections (as shown in figure 2.1b), and with its top edge 1 cm below the bottom of the grid's oscillation (as shown in figure 2.1a). For this case, therefore, the inner box had height $H = 35.0\,\text{cm}$ with a square internal cross-section $2L \times 2L$, with $2L = 24.5\,\text{cm}$ (see figure 2.1a). For simplicity we henceforth refer to this as the 'optimal' case, although we stress that no detailed optimisation analysis was performed.

For conciseness, we focus here on reporting results obtained for this 'optimal' case, which will be compared with corresponding results obtained using the standard OGT set-up (with no inner box installed). However, we recall that Drayton (1993) proposed that the inner box should be positioned with its top edge a distance at least $2M$ below the bottom of the grid's oscillation. However, our experiments showed that this was not the case, and that using an inner box of height $H = 26.5\,\text{cm}$ (with the same cross-section stated above), with its top edge located $2M = 10\,\text{cm}$ below the bottom of the grid's oscillation, had little effect in reducing the magnitude of the mean-flow components. This will be demonstrated below in section 2.3, where a comparison with this case will be shown.

Table 2.1 summarises the experimental conditions reported in this paper. The range of f used is typical of that used in most previous studies (Brumley and Jirka, 1987; Hannoun et al., 1988; Kit et al., 1997, 1995; McKenna and McGillis, 2004; Nokes, 1988; McCorquodale and Munro, 2017a; McDougall, 1979)[¶] and is below the maximum recommended frequency of 7 Hz (McDougall, 1979). In Table 2.1, the experiments labelled 'A' correspond to the standard OGT set-up, with no inner box installed; those labelled 'B' correspond to the 'optimal' case described above (using an inner-box of height $H = 35.0\,\text{cm}$); experiments performed with an inner box of height $H = 26.5\,\text{cm}$, positioned with it's top edge $2M$ below the bottom of the grid's oscillation (as proposed by Drayton, 1993), are labelled 'C'. Also shown in Table 2.1 are values of the grid Reynolds number, defined here as

$$Re \equiv MSf/\nu. \tag{2.2}$$

The three values considered, *i.e.*, $Re = 2020$, 4050 and 6070, are representative of those used in many previous studies (Brumley and Jirka, 1987; Hannoun et al., 1988; Kit et al., 1997, 1995; McKenna and McGillis, 2004; Nokes, 1988; McCorquodale and Munro, 2017a)[¶], which are typically between 10^3 and 10^4.

[¶]N.B. McCorquodale and Munro (2017a) is shown in chapter 3

Experiment	M (cm)	S (cm)	f (Hz)	H (cm)	Re
A1†	5.0	2.5	1.6	-	2020
A2†	5.0	2.5	3.2	-	4050
A3	5.0	2.5	4.9	-	6070
B1†	5.0	2.5	1.6	35.0	2020
B2†	5.0	2.5	3.2	35.0	4050
B3	5.0	2.5	4.9	35.0	6070
C2	5.0	2.5	3.2	26.5	4050

Table 2.1: A summary of the experimental conditions reported in this paper, where M denotes mesh size, S is the stroke, f the oscillation frequency, H the inner box height ('-' denotes when no inner box was installed) and Re the grid Reynolds number.

2.2.2 Velocity Measurements

Measurements of instantaneous fluid velocities were obtained using two-dimensional PIV, applied to the vertical plane through the centre of the grid (see figure 2.1b). A thin light sheet, produced by a 100 Hz pulsed laser (Dantec Dynamics NANO L Power 50-100), was used to illuminate small, neutrally buoyant seeding particles suspended within the water column, which act as a passive tracer as they are advected by the grid-stirred turbulence. The particles used were Pliolite with diameter range 75 to 125 μm, which when suspended within the water column had a volume fraction of $O(10^{-4})$. The motion of the illuminated particles was recorded using a high-speed digital camera positioned to point horizontally into the tank's interior (*i.e.*, the 'outer tank' for experiments A; the 'inner tank' for experiments B and C) and aligned perpendicular to the plane of the vertical light sheet (see figure 2.1b). The camera was synchronised with the pulse of the laser, so the images were recorded at 100 frames per second (at 1280×1024 pixel resolution). In all experiments, images were recorded for a period of at least 240 s. Measurements were made only after the grid had been allowed to oscillate (at a fixed frequency and stroke) for at least 15 min to ensure the turbulence was well established in a statistically stationary condition.

PIV calculations were performed in Digiflow (Dalziel, 2006), using square interrogation windows of 15×15 pixels, overlapped to achieve 10 pixel spacing between velocity vectors, which corresponded to a physical spacing between velocity vectors of approximately 0.21 cm to 0.28 cm. By means of comparison, within the turbulent-diffusive region (*i.e.* for $x_3 \gtrsim 2.5M$) the Kolmogorov length scale η was estimated to lie in the range $0.03\,\text{cm} \lesssim \eta \lesssim 0.13\,\text{cm}$. [The Kolmogorov length scale was estimated using the relation $\eta = \nu^{3/4}\varepsilon^{-1/4}$ under the assumption that, in OGT, $\varepsilon \approx 0.75(\overline{u_1'^2})^{3/2}/\ell$ for $x_3 \gtrsim 2.5M$ (Kit et al., 1997)]. Thus, the resolution used was coarser than the smallest turbulent

scales within the flow, such that velocity averaging occurred across interrogation windows and some turbulent fluctuations were unresolved. Consequently, the full energy content of the turbulent flow was not determined by the analysis. However, in the context of the size of the integral scales of the turbulent flow (which are of the order 2 cm in size, see section 2.3.3) the range in scales of turbulent fluctuations that were under-resolved in the current analysis was small and was assumed to have little effect on the results presented in section 2.3 since here we are primarily concerned with the large-scale structure of the flow.

The velocity data were calculated and analysed relative to the right-handed coordinate system (x_1, x_2, x_3), where x_3 denotes vertical depth below the mid-height of the grid's oscillation and (x_1, x_2) are the horizontal coordinates relative to the center of the grid (see figure 2.1). The corresponding velocity components are denoted (u_1, u_2, u_3); the two components measured using the PIV set-up described above are $u_1(x_1, x_3, t)$ and $u_3(x_1, x_3, t)$, in the central plane at $x_2 = 0$. For each experiment listed in Table 2.1, measurements were obtained with the camera focussed on the region $M \lesssim x_3 \lesssim 4.5M$ (*i.e.* focussing on the turbulent-diffusive region) and in this case the instantaneous velocity data were analysed using the conventional Reynolds decomposition $u_i = \overline{u}_i + u'_i$, where $u'_i(\mathbf{x}, t)$ denote the fluctuating components and $\overline{u}_i(\mathbf{x})$ the time-averaged mean components (the overbar notation is used throughout to denote time averaging). Previous PIV studies of OGT have typically analysed time-averaged statistical quantities using an averaging period of between 100 s and 120 s (Cheng and Law, 2001; Lucas et al., 2016; Wan Mohtar and Munro, 2013; Al-Homoud and Hondzo, 2007). Here, however, we found that an averaging period of 240 s was needed to ensure well-converged mean and rms velocity measurements.

A subset of the experiments listed in Table 2.1 (marked †) were repeated (under nominally identical conditions) to obtain PIV measurements focussed on the near-grid region, which were used to analyse the formation of the jets produced by the oscillating grid and, in particular, the effect the installation of the inner box had on the structure of these jets. This required analysis of the jet structures at different stages during the grid's oscillation and so time averaging was not appropriate, in this case. Instead, the near-grid-region data were analysed by ensemble averaging measurements of the fluid velocity fields taken at specific stages of the grid's oscillation. The ensemble-averaged mean velocity components, henceforth denoted U_1 and U_3, were computed at eight stages of the grid's oscillation, which corresponded to when the grid was located at the points $x_{3,k} = -S\cos(2\pi T_k)$, where $T_k = (k-1)/8$, $k = 1, 2, ..., 8$. That is, $x_{3,1}$ and $x_{3,5}$ correspond, respectively, to the top and bottom of the grid's oscillation. For $Re = 2020$ ($f = 1.6$ Hz) and $Re = 4050$ ($f = 3.2$ Hz) the available ensemble sizes were respectively 390 and 780, and the corresponding ensemble averaged quantities were found to be well converged using these ensemble sizes. We also note that for the case when no inner box

was installed the data below the grid at a given $x_{3,k}$ provides a mirror image of that we would observe above the grid for $x_{3,k+4}$ (*i.e.* when the direction of the grid's motion is reversed). That is, here we principally discuss the flow observed beneath the grid and assume the flow above the grid can be inferred using the symmetry of the apparatus. Figure 2.2 shows the ensemble-averaged mean velocity fields from experiment A1 (with no inner box present). We note that there are regions above and immediately below the grid where data have not been included. There are two main for this: (a) the passage of the light sheet through the tank was blocked by the grid, resulting in regions above the grid being in shadow where the PIV analysis failed; we note, however, that in regions above the grid where reliable data could be obtained it has been included. (b) Very close to the grid (above and below), where the magnitude of the fluid velocity was greatest, the PIV analysis mostly returned spurious velocity vectors, as a result of poor local correlation between interrogation windows in successive images, and so these data have not been included.

2.3 Results

2.3.1 The mean-flow structure in the near-grid region with no inner box installed

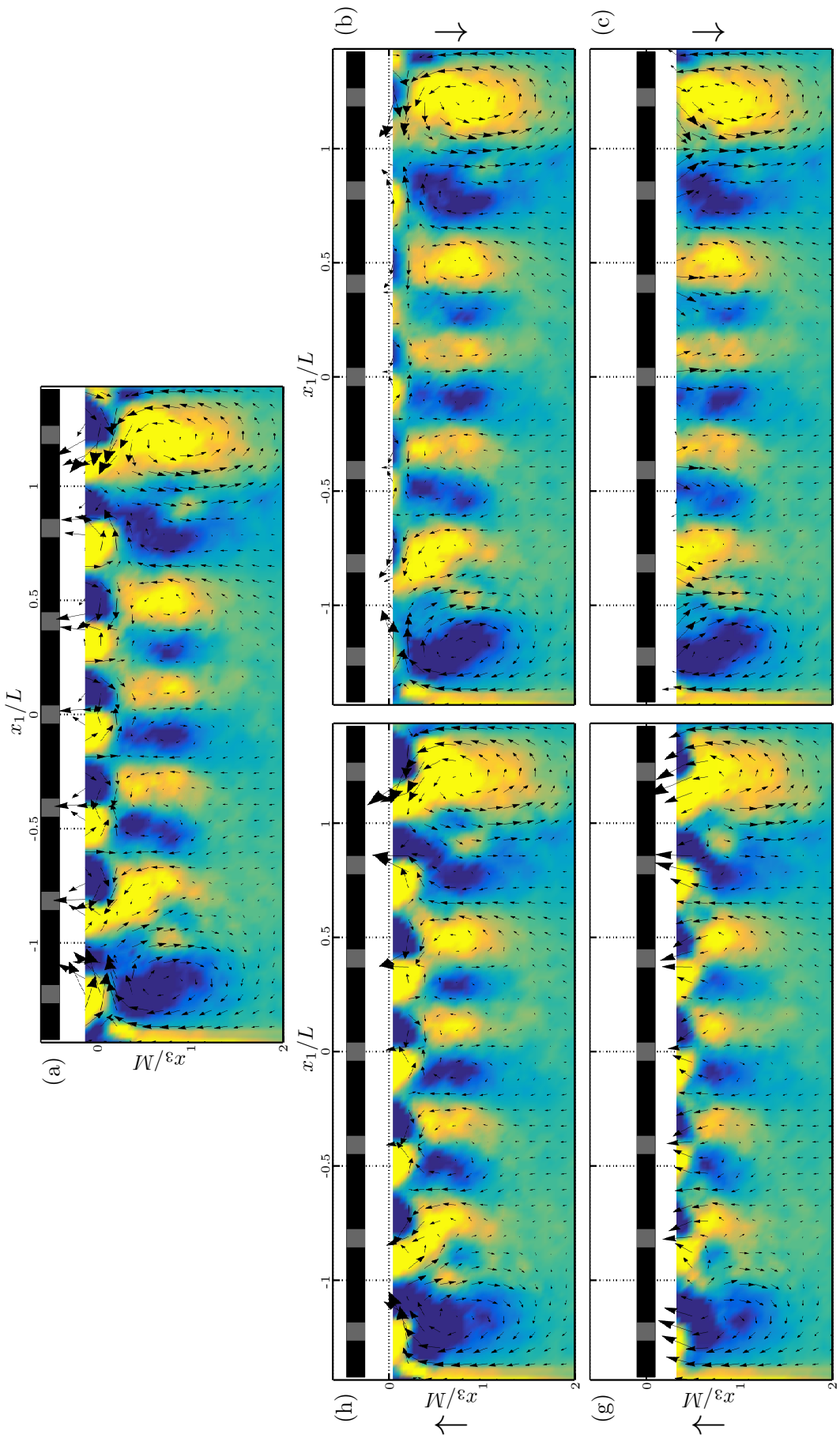
We start by describing the structure of the mean flow for the case when no inner box was installed, and by first focussing attention on the formation of jets in the near-grid region (which, recall, is given by $|x_3| \lesssim 2.5M$). For this we use measurements of the ensemble-averaged mean velocity components (U_1, U_3), calculated at the eight grid locations $x_{3,k}$. Figure 2.2 shows vector plots of U_1/fS and U_3/fS from Experiment A1 ($Re = 2020$), at each $x_{3,k}$, together with corresponding measurements of the ensemble-averaged mean vorticity component Ω_2/f (*i.e.*, Ω_2 was calculated by ensemble averaging measurements of $\omega_2 = \partial u_1/\partial x_3 - \partial u_3/\partial x_1$ at each $x_{3,k}$). The same colour scale for vorticity is used in each plot, which is shown in figure 2.2(e), together with a reference scale for velocity; only every third velocity vector (in each direction) has been shown to avoid an over saturation of data. Figures 2.2(a) and 2.2(e) correspond, respectively, to the top and bottom of the grid's oscillation and the direction of the grid's motion is shown in the remaining plots by the arrow at the side of each plot. The instantaneous position of the grid is also shown in each plot (thick black line), together with the location of the grid intersections (grey squares). The data are plotted against (x_1, x_3), where x_3 has been scaled using the mesh size M and, although no inner box was used in this case, for the purposes of later comparisons x_1 has been scaled with $L = 12.25\,\text{cm}$ (the inner-box half width).

Ignoring for now the data adjacent to the tank sidewalls and, instead, focussing attention on the central region $|x_1/L| \lesssim 0.6$, we see that below the lowest point of the

grid's oscillation (*i.e.* below $x_3/M = S/M = 0.5$) the mean-flow structure consists of a regular array of 'jets' produced by the elements of the oscillating grid, with each jet having comparable strength and consisting of a downward-directed outflow directly below grid intersections, with a corresponding upward-directed return flow induced in the regions below the mesh voids. (The term 'jets' has been widely used in previous studies to describe these mean-flow structures (Turner, 1968; Thompson and Turner, 1975).) The regular structure of the jet array within this central region is best seen in figure 2.2(e) (which corresponds to the lowest point of the grid's oscillation) by the array of counter-rotating vortices that have formed below $x_3/M \approx 0.5$, on either side of the grid intersections. The jets spread, merge and (spatially) decay in the direction normal to and away from the grid, being all but fully decayed by the edge of the near-grid region. It is important to note that these jet structures are an approximately 'steady' feature of the flow. We also stress here that the flow structure described above (and below) is of course not two-dimensional, but three-dimensional; that is, due to the symmetry of the grid (and container) we expect there to be similar structure to the flow in the perpendicular x_2-direction.

The ensemble-averaged fields also show the presence of a regular array of counter-rotating vortex pairs that form periodically in the immediate wake of the grid, *i.e.*, in the region $|x_3/M| \lesssim S/M = 0.5$. For example, at the top of the grid's oscillation (figure 2.2a), following completion of the grid's upstroke, the wake vortices have formed immediately below the grid elements, with each pair having the opposite sense circulation to the vortices associated with the jet structures directly below. Conversely, at the bottom of the grid's stroke (figure 2.2e), following completion of the grid's downstroke, the wake vortices have formed immediately above the grid but instead have the same sense circulation to the vortices associated with the jets. Therefore, as the grid oscillates up and down, intense vortices are shed periodically from grid elements which then form in the immediate wake (above or below) the grid. The sense of circulation within the wake vortices depends upon the grid's direction of the motion—the vorticity within the wake vortices changes sign when the grid's direction changes. In contrast, the sense of circulation within the jet vortices remains constant with time, irrespective of the grid's direction of the motion. The vortices produced in the wake of the grid are subsequently ejected away from the grid within the vertical jets below the wake region. We note that when the downstroke (figures 2.2b-d) and the upstroke (figures 2.2f-h) of the grid are compared we see that, during the grid's descent (when the wake vortices and jet vortices have the same sense circulation) there is a slight but noticeable increase in strength within the vertical jets directly beneath each intersection.

We now consider the structure of the ensemble-averaged mean flow in the regions adjacent to the tank sidewalls, for $|x_1/L| \gtrsim 0.6$. The data in figure 2.2 show that beyond the immediate wake of the grid, for $|x_3/M| > S/M = 0.5$, a single jet has formed


(a)
(b)
(c)
(g)
(h)
x_1/L
$M/\varepsilon x_1$
$\rightarrow$
$\leftarrow$

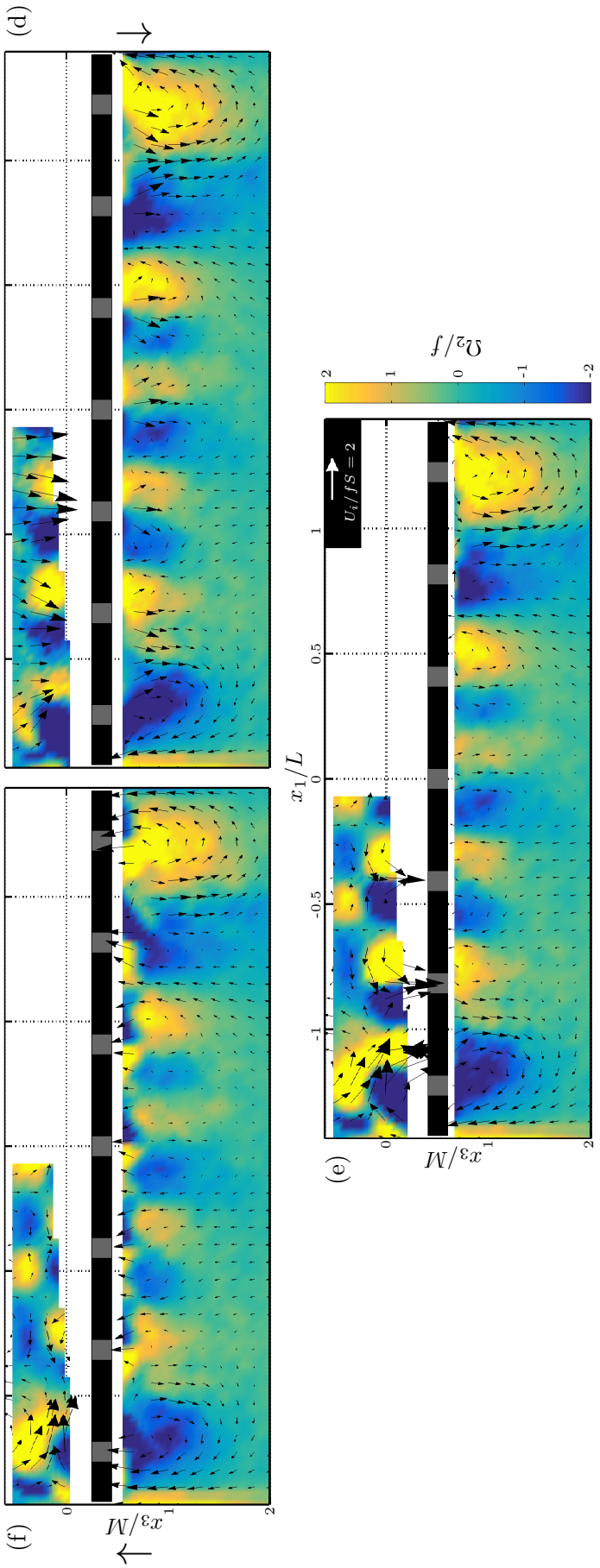


Figure 2.2: Experiment A1 ($Re = 2020$, $f = 1.6\,\mathrm{Hz}$). Vector plots showing the ensemble-averaged mean velocity components U_1/fS and U_3/fS, together with the corresponding ensemble-averaged mean vorticity Ω_2/f, at each of the eight grid locations $x_{3,k}$: (a) $x_{3,1} = -S$, (b) $x_{3,2} = -0.71S$, (c) $x_{3,3} = 0$, (d) $x_{3,4} = 0.71S$, (e) $x_{3,5} = S$, (f) $x_{3,6} = 0.71S$, (g) $x_{3,7} = 0$, (h) $x_{3,8} = -0.71S$. The same colour scale for vorticity has been used in each plot, which is shown in (e), together with a reference velocity scale. To prevent an over saturation of data, only every third velocity vector has been included. In (b-d) and (f-h) the direction of the grid's motion is shown by the arrow at the side of each plot.

below the two outermost grid intersections, on each side of the grid. These 'outer jets' exhibit significantly larger velocities and are approximately twice the size of the jet structures that form below the centre of the grid; that is, the outer and central jets have characteristic widths of order $2M$ and M, respectively. As a result, the stronger outer jets penetrate to a greater depth below the grid before decaying. We also observe that the axis of the outer jets, identified by the strong vertical downward flow, is not coincident with a grid intersection, as is the case for the central jets, but instead is coincident with the midpoint between the two outermost intersections (for example, see figure 2.2e).

The outer jets form as a result of the no-slip and no-penetration conditions at the vertical sidewalls, together with the edge conditions of the grid, combining to give rise to a complicated three-dimensional flow structure in the wake (above or below) the perimeter region of the grid. At this point we stress the inherent limitations in the two-dimensional vertical-plane velocity data reported here; the data do not, of course, fully resolve the features of the three-dimensional flow produced around the perimeter of the grid. However, the two-dimensional velocity data do enable us to show the key structures that result, due to this three-dimensional flow, within the near-grid region. That is, the data do show that as the grid ascends (figure 2.2e-h), we observe an asymmetry in the counter-rotating vortex pair that forms in the wake below the outermost grid intersection (see figures 2.2e to 2.2a). The result is that instead of observing a strong vertical flow in the wake vortices towards the grid intersection, as is the case in the central region (see figure 2.2a), below the outermost intersection we observed a strong flow that is inclined towards the inside of the intersection, which can be seen in figure 2.2(a) in the wake region at $x_1/L \approx \pm 1.17$. We believe that this edge effect, combined with other three-dimensional edge effects and the viscous and no-penetration conditions at the sidewalls results in the merging of the jets below the two outermost grid elements (in the sidewall-normal direction), and ultimately the formation of the single outer jet in this region. The deflection and subsequent merging of the jets identified here has some similarities to the descriptions of jet-switching previously reported when using high-solidity grids (Hopfinger and Toly, 1976).

The formation of the stronger outer jets has significant effects on the structure of the flow. In comparison to the central jets, the outer jets penetrate to a greater depth below the grid before decaying. This greater penetration of outer jets has previously been proposed to induce large scale circulations that affect the entire domain (Drayton, 1993). The data reported here are consistent with this proposal, as illustrated in figure 2.3 which shows a vector plot of the time-averaged mean velocity components $\overline{u_1}/fS$ and $\overline{u_3}/fS$ for Experiment A1 ($Re = 2020$), together with corresponding measurements of the the time-averaged mean vorticity component $\overline{\omega_2}$ (note the different velocity vector scale used in figure 2.3 relative to figure 2.2). These data show that, in the absence of an inner box

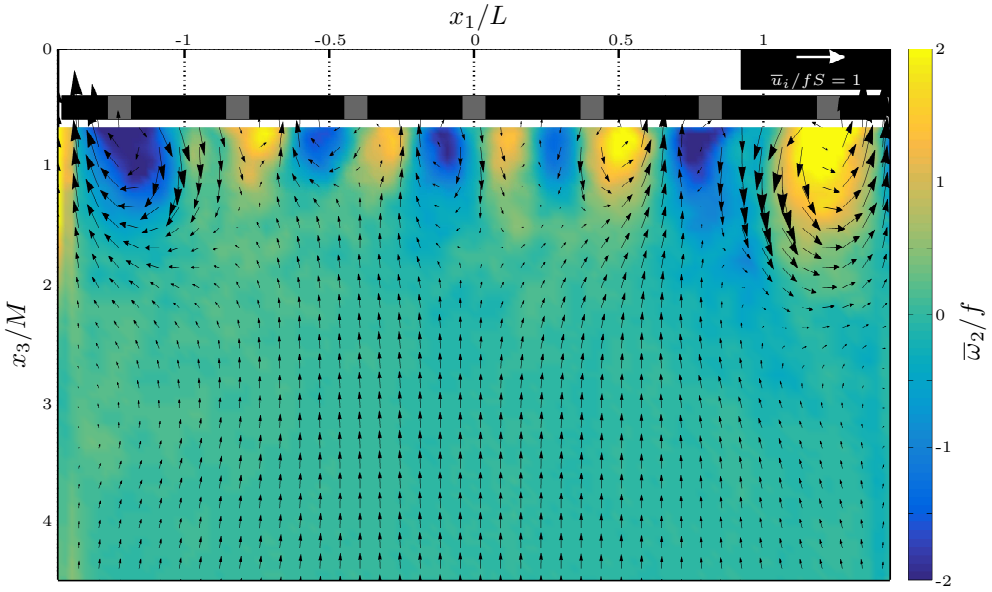
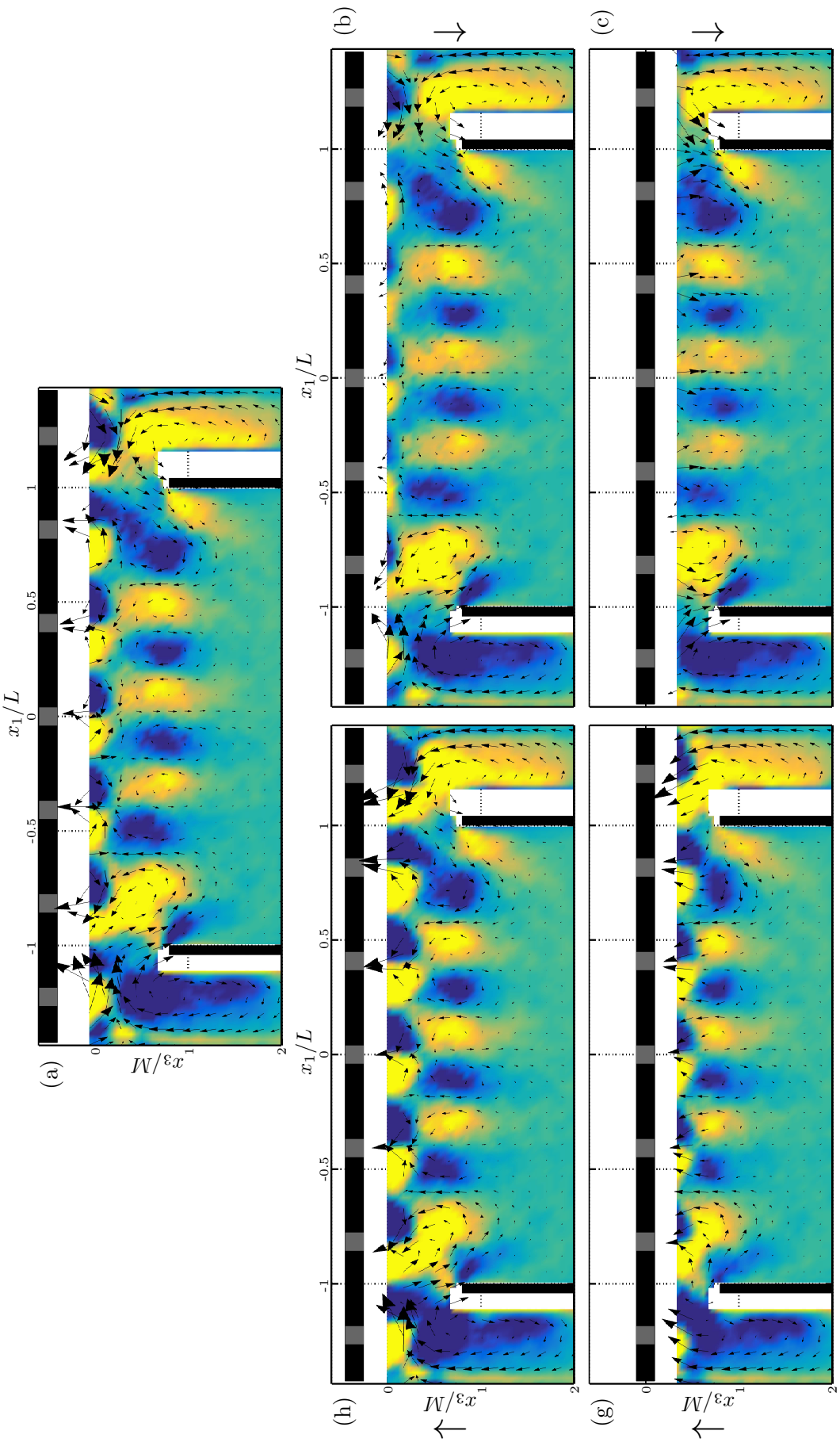


Figure 2.3: Experiment A1 ($Re = 2020, f = 1.6\,\mathrm{Hz}$). Vector plots showing the time-averaged mean velocity components $\overline{u}_1/fS$ and $\overline{u}_3/fS$, together with the corresponding time-averaged mean vorticity component $\overline{\omega}_2/f$. A reference velocity scale and vorticity scale is shown. To prevent over-saturation only every third velocity vector has been included. For reference the grid is shown at the lowest point within its oscillation.

there is a significant (on this plane predominantly upward) time-averaged mean flow induced in both the near-grid and turbulent-diffusive regions. For reference we note that the average values of mean-flow intensity in the turbulent-diffusive region, computed as a spatial average across the region given by $2.5 \leq x_3/M \leq 4.5$ and $|x_1/L| \leq 0.7$, are $|\overline{u}_1|/(\overline{u_1'^2})^{1/2} \approx 0.2$ and $|\overline{u}_3|/(\overline{u_3'^2})^{1/2} \approx 3.5$ for Experiment A1; these values are also representative for the corresponding data obtained in Experiments A2 and A3. Time-averaged mean flow fields indicating the presence of large scale circulations, similar to the data shown in figure 2.3, have also been reported in a range of previous OGT studies (see for example Bennett et al., 2014; McKenna and McGillis, 2004; Dohan and Sutherland, 2002).

2.3.2 The mean-flow structure in the near-grid region with inner box installed

For comparison, figure 2.4 shows data from Experiment B1 ($Re = 2020$), with the inner box installed in the 'optimal' position; for reference, the position of the inner-box sidewalls are shown by the vertical black lines. The ensemble-averaged mean velocity components U_1/fS and U_3/fS are shown at the eight grid locations $x_{3,k}$, together with corresponding measurements of the ensemble-averaged mean vorticity component Ω_2/f. The same scales for velocity and vorticity have been used in figures 2.2 and 2.4 to facilitate a direct comparison. Note that the data for regions above and immediately


(a)
(b)
(c)
(g)
(h)
x_1/L
$\mathcal{N}/\varepsilon x_1$
1
0.5
0
-0.5
-1
0
2

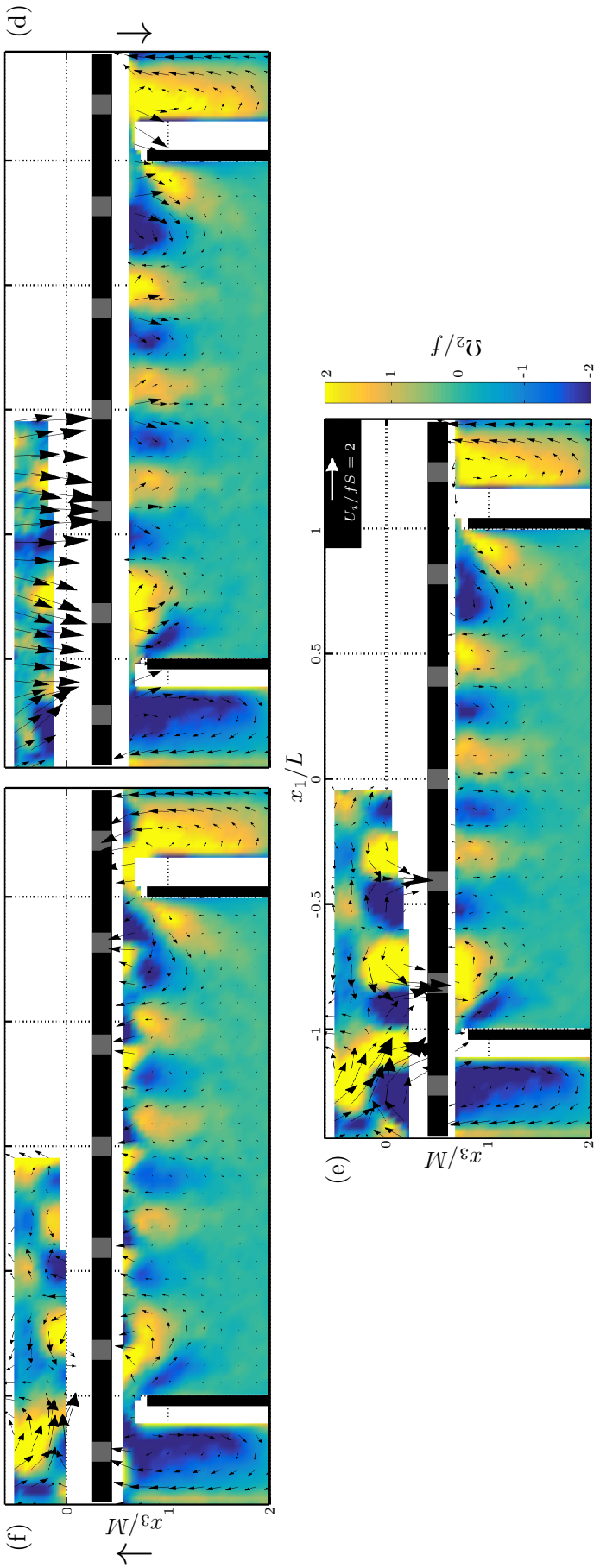


Figure 2.4: Experiment B1 ($Re = 2020$, $f = 1.6\,\mathrm{Hz}$). Vector plots showing the ensemble-averaged mean velocity components U_1/fS and U_3/fS, together with the corresponding ensemble-averaged mean vorticity Ω_2/f, at each of the eight grid locations $x_{3,k}$: (a) $x_{3,1} = -S$, (b) $x_{3,2} = -0.71S$, (c) $x_{3,3} = 0$, (d) $x_{3,4} = 0.71S$, (e) $x_{3,5} = S$, (f) $x_{3,6} = 0.71S$, (g) $x_{3,7} = 0$, (h) $x_{3,8} = -0.71S$. The same colour scale for vorticity has been used in each plot, which is shown in (e), together with a reference velocity scale. To prevent an over saturation of data, only every third velocity vector has been included. In (b-d) and (f-h) the direction of the grid's motion is shown by the arrow at the side of each plot.

below the grid, where the PIV algorithm produced spurious velocity vectors, has not been included. In addition, data immediately outside the inner box sidewalls has not been included in figure 2.4 as a result of substantially reduced image quality in these regions, due to the reflection and refraction of light from the inner box sidewalls, over which the PIV analysis also failed.

The data in figure 2.4 shows that the presence of the inner box has little, if any, affect on the vortices that form in the immediate wake of the grid, where we again observe a regular array of vortex pairs forming periodically below (or above) each intersection, with the same edge effects described above again evident below (or above) the two outermost grid intersections. That is, the mechanisms responsible for the formation of the merged outer jets are still present. However, figure 2.4 shows that below the grid's immediate wake, the presence of the inner-box sidewalls at $|x_1/L| = 1$ blocks the formation of the merged outer jets, instead resulting in large-scale recirculations forming in the compartment between the inner and outer boxes, which extend up to and beyond $x_3 \approx 2M$. (We no further consider the compartment region between the inner and outer containers and henceforth focus attention on the flow conditions within the interior of the inner box.) Notably, similar large-scale recirculations are not induced inside the inner box. Instead, the array of jet structures that form across the interior of the inner box are of a more uniform strength and structure. Below the centre of the grid the jets again consists of a downward-directed outflow directly below grid intersections, with a corresponding upward-directed return flow induced in the regions below the mesh voids. However, the outermost jets within the inner box (at $x_1/L \approx \pm 0.8$) are inclined towards the centre of the grid, exhibiting downward-directed flow between the inner-box sidewall and the nearest grid intersection (at $x_1/L = \pm 0.8$), with a corresponding upward-directed return flow induced in the regions below the mesh voids at $x_1/L = \pm 0.6$. The regular structure of these jets is attributed to how the merged outer jets are blocked by the inner-box sidewalls, which gives rise to flow separation at the top rim of the inner box, resulting in the formation of the jets inclined towards the centre of the grid. Both the inclined and central jets spread, merge and (spatially) decay in the direction normal to and away from the grid, being all but fully decayed by the edge of the near-grid region.

The results of the time-averaged mean flow, shown in figure 2.5, indicate that within the inner box a (non-uniform) mean flow is evident within the turbulent-diffusive region, but is much weaker in comparison to the mean flow observed when no inner box is installed (see figure 2.3). Note that, so that direct comparison can be made, the time-averaged mean flow field shown in figure 2.5 uses the same scales for velocity and vorticity used in figure 2.3. For reference we note that the average values of mean-flow intensity in the turbulent-diffusive region, computed as a spatial average across the region given by $2.5 \leq x_3/M \leq 4.5$ and $|x_1/L| \lesssim 0.5$, are $|\overline{u}_1|/(\overline{u_1'^2})^{1/2} \approx 0.3$ and $|\overline{u}_3|/(\overline{u_3'^2})^{1/2} \approx 0.6$ for Experiment B1 (which are also representative of Experiments B2-B3); comparing

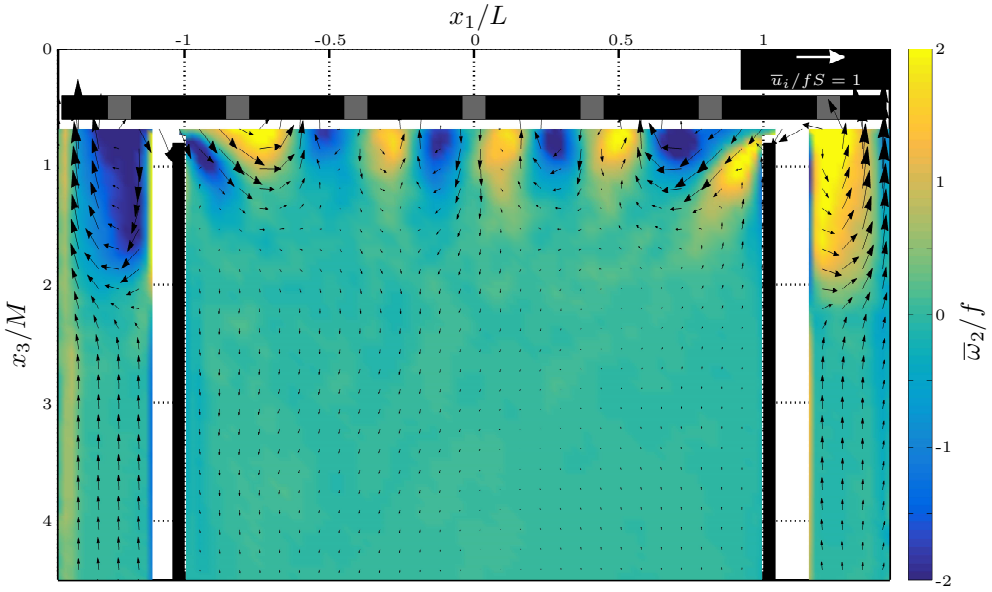


Figure 2.5: Experiment B1 ($Re = 2020, f = 1.6\,\mathrm{Hz}$). Vector plots showing the time-averaged mean velocity components $\overline{u}_i/fS = 1$, together with the corresponding time-averaged mean vorticity component $\overline{\omega}_2/f$. A reference velocity scale and vorticity scale is shown. To prevent over-saturation only every third velocity vector has been included. For reference the grid is shown at the lowest point within its oscillation.

with the corresponding values obtained for Experiment A1 ($|\overline{u}_1|/(\overline{u_1'^2})^{1/2} \approx 0.2$ and $|\overline{u}_3|/(\overline{u_3'^2})^{1/2} \approx 3.5$) shows that the installation of the inner box results in a significant reduction in the magnitude of the (predominantly vertical) mean flow. This result is consistent with Drayton's (Drayton, 1993) proposal that mean flow arises when there is a significant difference in the relative strength of the jets produced by the oscillating grid in different regions of the tank; with the inner box installed, the jets are of approximately equal strength and penetrate to approximately equal depth before breaking down.

2.3.3 Effect of mean flow on turbulent structure

We now describe how the installation of the inner box affects the spatial structure of the turbulence, in both the near-grid and turbulent-diffusive regions. Turbulence is produced in the near-grid region when the individual jets produced by the grid break down, resulting in a conversion of mean kinetic energy to turbulent kinetic energy. The turbulence is sustained within the turbulent-diffusive region primarily by the transport of TKE from the near-grid region, in the grid-normal direction. This process is described by the steady transport equation for turbulent kinetic energy, which may be written as (Hinze, 1975, p. 323)

$$0 = \underbrace{-\overline{u}_k \frac{\partial}{\partial x_k}\overline{u_i' u_i'}}_{A_{ii}^d} \underbrace{-2\overline{u_i' u_k'}\frac{\partial \overline{u}_i}{\partial x_k}}_{\Phi_{ii}} \underbrace{-\frac{\partial}{\partial x_k}\overline{u_i' u_i' u_k'}}_{T_{ii}} \underbrace{-\frac{2}{\rho}\frac{\partial}{\partial x_i}\overline{p' u_i'}}_{\Pi_{ii}^d} \underbrace{+\nu\frac{\partial^2 \overline{u_i' u_i'}}{\partial x_k \partial x_k}}_{D_{ii}} \underbrace{-2\nu\overline{\frac{\partial u_i'}{\partial x_k}\frac{\partial u_i'}{\partial x_k}}}_{\varepsilon_{ii}}. \quad (2.3)$$

The terms A_{ii}^d and Φ_{ii} denote, respectively, transport and production due to the mean flow; T_{ii} and Π_{ii}^d denote, respectively, transport by velocity and pressure fluctuations; D_{ii} and ε_{ii} denote molecular diffusion and viscous dissipation. We now consider how the time-averaged measurements of mean flow, degree of isotropy, rms velocity components and the vertical flux of turbulent energy by turbulent fluctuations are influenced by the physical processes described by dominant terms $(A_{ii}^d, \Phi_{ii}, T_{ii})$ of equation (2.3).

We note that in previous studies the qualitative characteristics of the turbulence produced by an oscillating-grid were not found to exhibit Reynolds number effects across the fairly limited Reynolds number ranges used (typically between 10^3 and 10^4) (see for example Hopfinger and Toly, 1976; Wan Mohtar and Munro, 2013). In line with this observation, the qualitative characteristics of the experimental data reported here were also found to be little different over the range of Reynolds numbers considered ($Re_G = 2020$ to 6070), and so we present here results for the case $Re_G = 4050$, which are representative. The key comparisons are made using data from Experiments A2 (no inner box installed) and B2 (inner box installed in the 'optimal' position); however, for interest, comparison is also shown with data from Experiment C2 with the inner box positioned (as suggested by Drayton, 1993) with its top edge at $x_3 \approx 2.5M$.

Firstly, we consider field measurements of the time-averaged degree of isotropy. The idealised model for OGT assumes the turbulence produced is homogeneous and isotropic in planes parallel to the grid, with $(\overline{u_3'^2})^{1/2}/(\overline{u_1'^2})^{1/2} \approx 1$ within the turbulent-diffusive region. In line with this assumption, previous experimental studies have reported the degree of isotropy to be approximately constant with $(\overline{u_3'^2})^{1/2}/(\overline{u_1'^2})^{1/2} \approx 1.1$ to 1.4 in the turbulent-diffusive region (Hopfinger and Toly, 1976; Hopfinger and Linden, 1982; Kit et al., 1997). However, to our knowledge, field measurements of the (spatially non-uniform) degree of isotropy have not previously been reported in studies of OGT and the structure of the turbulence in the near-grid region is largely unknown. We stress that an understanding of the degree of isotropy of the turbulence is necessary to ensure the validity of subsequent statistical analysis. That is, in previous OGT studies it is common for statistical quantities to be spatially averaged (see for example Hannoun et al., 1988; Cheng and Law, 2001; Orlins and Gulliver, 2003; Wan Mohtar and Munro, 2013; McCorquodale and Munro, 2017a; Bennett et al., 2014)[¶] over regions thought to be approximately homogeneous and isotropic and which are not affected by the presence of the tank side walls. However, few studies have reported measurements that can justify the spatial averages used. At best, previous work has shown spatial distributions of turbulent velocity components over limited regions of the tank (Lucas et al., 2016; McDougall, 1979; Cheng and Law, 2001), which do not show key features of the flow that we identify here.

The colour maps in figure 2.6 show measurements of the time-averaged degree

[¶]N.B. McCorquodale and Munro (2017a) is shown in chapter 3

of isotropy, $(\overline{u_3'^2})^{1/2}/(\overline{u_1'^2})^{1/2}$, from Experiments A2, B2 and C2 (see caption for details). To illustrate the effects of turbulent production due to the mean flow (*i.e.*, the term Φ_{ii} in equation 2.3), in each plot the time-averaged mean velocity components $(\overline{u}_1/fS, \overline{u}_3/fS)$ have been superimposed on top of the isotropy field. The same colour scale for $(\overline{u_3'^2})^{1/2}/(\overline{u_1'^2})^{1/2}$ has been used in each plot, which is shown in figure 2.6(a), together with a reference scale for velocity; again, only every third velocity vector (in each direction) has been shown. For reference, the grid is shown in each plot positioned at the bottom of its oscillation and the vertical black lines indicate the position of the inner-box sidewalls. Clearly, the data shown in figure 2.6 resolve only the central vertical plane inside the container; however, due to the symmetry of the grid and container we anticipate a similar structure (qualitatively) in $(\overline{u_3'^2})^{1/2}/(\overline{u_1'^2})^{1/2}$ in the perpendicular x_2-direction.

The data in figure 2.6(a) shows that in the near-grid region, with no inner box installed, the turbulence is clearly anisotropic; that is, the degree-of-isotropy field is not uniform, but instead exhibits peak values (typically, $(\overline{u_3'^2})^{1/2}/(\overline{u_1'^2})^{1/2} \approx 2$) where the spatial gradients in the (time averaged) mean velocity components are greatest. Inspection of figure 2.6(a) shows that, in the near-grid region, the peak values of $(\overline{u_3'^2})^{1/2}/(\overline{u_1'^2})^{1/2}$ occur roughly below each grid intersection where the individual jets produced by the grid break down. This is attributed to localised anisotropic turbulent production; in these regions the spatial gradients of $\overline{u}_3$ exceed the spatial gradients of $\overline{u}_1$ such that the production of $(\overline{u_3'^2})^{1/2}$ is greater than the production of $(\overline{u_1'^2})^{1/2}$ (*i.e* $\Phi_{33} > \Phi_{11}$). (Recall that the production of TKE is described by the term Φ_{ii}, which is proportional to the mean-flow shear.)

Within the turbulent-diffusive region (*i.e.* $x_3 \gtrsim 2.5M$), where the jet structures have broken down, the turbulence is approximately isotropic, but only over the central region $|x_1/L| \lesssim 0.5$; in this region the degree of isotropy is approximately uniform with $(\overline{u_3'^2})^{1/2}/(\overline{u_1'^2})^{1/2} \approx 0.8$. However, as the sidewalls are approached the turbulence becomes increasingly anisotropic, with $(\overline{u_3'^2})^{1/2}/(\overline{u_1'^2})^{1/2} \gtrsim 2$ in close proximity to the wall. The increase of $(\overline{u_3'^2})^{1/2}/(\overline{u_1'^2})^{1/2}$ in the sidewall region can be understood in light of previous work studying the interaction of zero-mean-shear turbulence with boundaries (Hunt and Graham, 1978; Hannoun et al., 1988; McCorquodale and Munro, 2017a)¶. In particular, in recent work the current authors studied the interaction of OGT with solid impermeable boundary (McCorquodale and Munro, 2017a)¶ and identified that the no-penetration boundary condition acts to inhibit only the boundary-normal turbulent fluctuations (*i.e.*, $(\overline{u_1'^2})^{1/2}$ at the sidewalls) over a layer approximately equal in thickness to the integral length scale of the turbulence. A similar reduction does not occur for the boundary-tangential turbulent fluctuations (*i.e.*, $(\overline{u_3'^2})^{1/2}$); instead the rms boundary-tangential fluctuations are approximately constant across much of the boundary-effected region,

¶N.B. McCorquodale and Munro (2017a) is shown in chapter 3

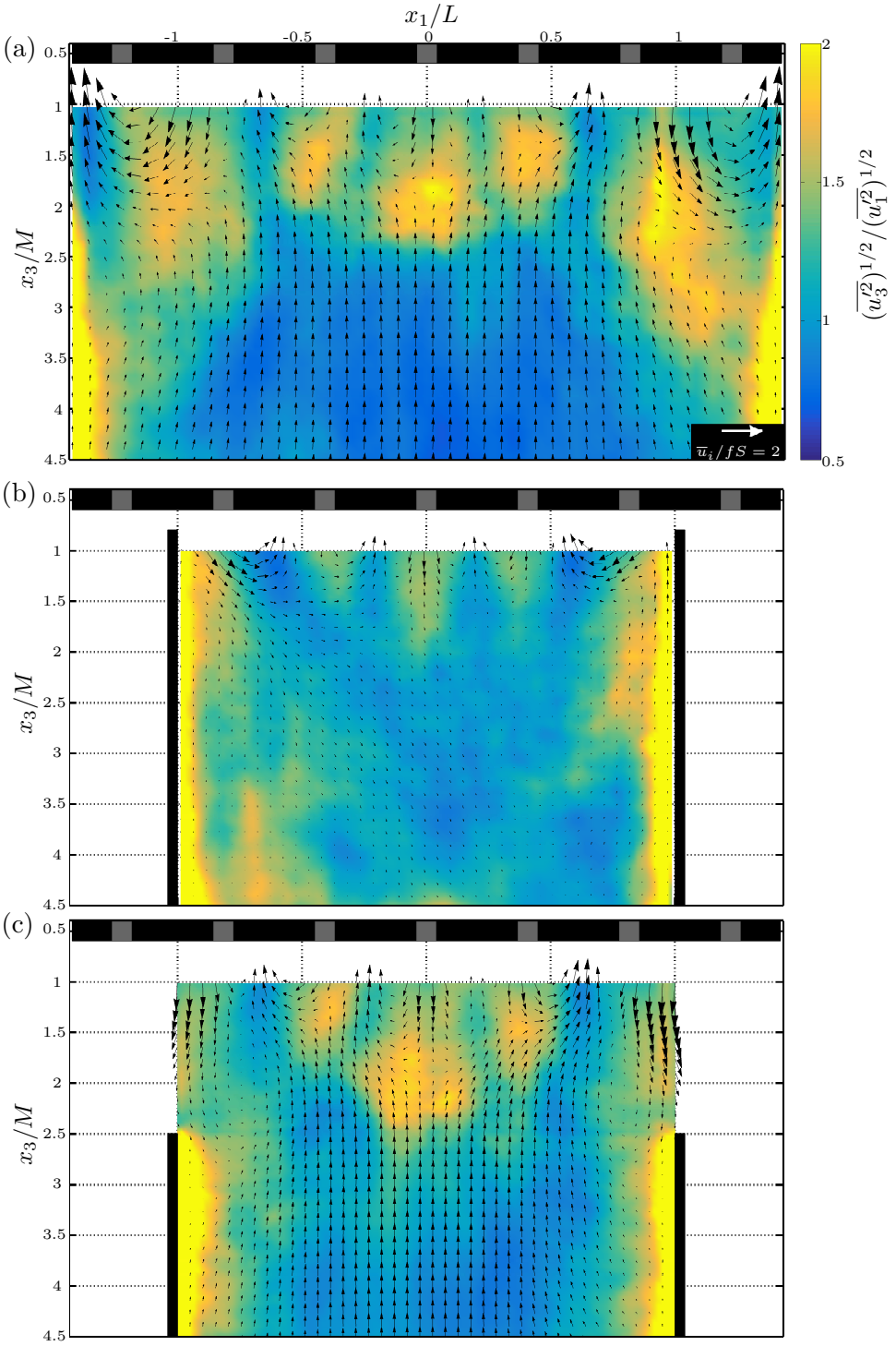


Figure 2.6: Colourmaps showing the degree-of-isotropy field $(\overline{u_3'^2})^{1/2}/(\overline{u_1'^2})^{1/2}$ together with vector plots showing the time-averaged components of mean velocity $\overline{u}_i/fS$. The data shown are (a) Experiment A2 (b) Experiment B2 and (c) Experiment C2. In each case, $Re = 4050$, $f = 3.6\,\mathrm{Hz}$. The same colour scale for isotropy has been used in each plot, which is shown in (a), together with a reference velocity scale. To prevent an over saturation of data, only every third velocity vector has been included. For reference the grid is shown at the lowest point within its oscillation.

giving rise to the increase in anisotropy reported here. The constant magnitude of the boundary-tangential turbulent fluctuations has been attributed primarily to the effects of turbulent transport (T_{ii} in equation 2.3) (McCorquodale and Munro, 2017a)¶ and intercomponent energy transfer, although the nature of this transfer remains contentious (Perot and Moin, 1995a; Bodart et al., 2010; Hunt and Graham, 1978). It is only within the thin viscous sublayer, immediately adjacent to the boundary, that the no-slip condition also acts to inhibit the boundary-tangential turbulent fluctuations (driven by the dissipation of TKE, ε_{ii}) (Perot and Moin, 1995a; McCorquodale and Munro, 2017a)¶, but anisotropy continues to increase even over this region.

For comparison, figure 2.6(b) shows corresponding data obtained with the inner box installed in the 'optimal' position. Again, the turbulence is anisotropic in the near-grid region, although the degree of anisotropy is significantly reduced, with peak values of $(\overline{u_3'^2})^{1/2}/(\overline{u_1'^2})^{1/2} \approx 1.3$. The reduction in anisotropy is attributed to a reduction in the production of $(\overline{u_3'^2})^{1/2}$ (*i.e.* reduction in Φ_{33}) in regions in which the jets break down; the weak time-averaged mean flow in the turbulent diffusive region gives rise to smaller spatial gradients in the mean flow (*i.e.* a reduction in the magnitude of $\partial u_3/\partial x_i$) over these regions relative to when no inner box is installed. Within the turbulent-diffusive region, the turbulence over the central region, $|x_1/L| \lesssim 0.5$, is effectively isotropic, with $(\overline{u_3'^2})^{1/2}/(\overline{u_1'^2})^{1/2} \approx 1$. As the sidewalls are approached, and for the same reasons given above, the turbulence again becomes increasingly anisotropic with peak values of $(\overline{u_3'^2})^{1/2}/(\overline{u_1'^2})^{1/2} \gtrsim 2$ observed close to the wall.

Figure 2.6(c) shows corresponding data obtained from Experiment C2, with the inner box positioned with its top edge at a depth $x_3 \approx 2.5M$ (*i.e.*, with its top edge $2M = 10\,\text{cm}$ below the bottom of the grid's oscillation). These data clearly show that this positioning of the inner box (as suggested by Drayton, 1993) does not inhibit the formation of the merged outer jets below the outermost grid elements. As a result, when the data in figures 2.6(a) and 2.6(c) are compared we observe a similar degree of turbulence anisotropy in the near-grid region and, most importantly, little, if any, reduction in the magnitude of the mean flow throughout the bulk of the fluid. Consequently, we give no further consideration to Experiment C2.

The effect the tank sidewalls have on the degree of isotropy can be seen more clearly in figure 2.7, which shows spatially averaged measurements of $(\overline{u_3'^2})^{1/2}/(\overline{u_1'^2})^{1/2}$ from Experiments A1-A3 and Experiments B1-B3 (see caption for details). Note that the data have been spatially averaged only over those regions in which the field $(\overline{u_3'^2})^{1/2}/(\overline{u_1'^2})^{1/2}$ is approximately homogeneous. That is, in figure 2.7(a) we show $\langle(\overline{u_3'^2})^{1/2}/(\overline{u_1'^2})^{1/2}\rangle_3$ which has been spatially averaged in the x_3 direction (denoted $\langle\cdot\rangle_3$) over the turbulent-diffusive region given by $2.5 \leq x_3/M \leq 4.5$, plotted against the horizontal coordinate x_1, which has been normalised by the tank half width, ζ. (Recall that $\zeta = 17.6\,\text{cm}$

¶N.B. McCorquodale and Munro (2017a) is shown in chapter 3

for experiments A and $\zeta = L = 12.25\,\mathrm{cm}$ for experiments B.) These data confirm that the turbulence produced by the oscillating grid is approximately isotropic only over the central region, $|x_1/\zeta| \lesssim 0.5$; outside of this region the anisotropy of the turbulence increases as the sidewalls are approached. We stress this is a key limitation of OGT that, to our knowledge, has not previously been reported; we first identified and reported this effect in a recent, related study (McCorquodale and Munro, 2017a)[¶], using two grid types (the 7×7 grid used here, with mesh spacing $M = 5\,\mathrm{cm}$, and a 9×9 grid with mesh spacing $M = 3.8\,\mathrm{cm}$). With this limitation in mind, in figure 2.7(b) we show $\langle(\overline{u_3'^2})^{1/2}\rangle_1/\langle(\overline{u_1'^2})^{1/2}\rangle_1$, which has been spatially averaged in the x_1 direction (denoted $\langle\cdot\rangle_1$) across only the central region of the container (*i.e.* $|x_1/\zeta| \lesssim 0.5$), plotted against the vertical coordinate x_3, which has been normalised by the the grid mesh M. These data confirm that with the inner box installed in its 'optimal' position the degree of isotropy is approximately constant over the central region (*i.e.* $|x_1/\zeta| \lesssim 0.5$) of the turbulent-diffusive region. However, note that with no inner box installed the turbulence is weakly anisotropic (*i.e.*, $\langle(\overline{u_3'^2})^{1/2}\rangle_1/\langle(\overline{u_1'^2})^{1/2}\rangle_1 \approx 0.8$) even over the central region. The cause of the loss of isotropy, relative to experiments with the inner box installed, is currently unclear. Note also that here the magnitude of this data are slightly lower than in previous studies of OGT (for example, $\langle(\overline{u_3'^2})^{1/2}\rangle_1/\langle(\overline{u_1'^2})^{1/2}\rangle_1 \approx 1.1 - 1.4$ in Hopfinger and Linden, 1982; Kit et al., 1997; Hopfinger and Toly, 1976; De Silva and Fernando, 1994); we attribute this effect, at least in part, to the fact that the spatial averaging used here excludes the anisotropic sidewall regions where the ratio of $(\overline{u_3'^2})^{1/2}/(\overline{u_1'^2})^{1/2}$ is significantly higher.

Further insight into the effect the installation of the inner box has on the turbulence can be obtained by considering measurements of the rms turbulent velocity components $(\overline{u_1'^2})^{1/2}$ and $(\overline{u_3'^2})^{1/2}$. The spatial distribution of each component exhibits the same key qualitative characteristics, so for brevity we consider here only the vertical velocity component. The colourmaps in figure 2.8 show measurements of $(\overline{u_3'^2})^{1/2}/fS$ from experiment A2 (figure 2.8a) and experiment B2 (figure 2.8b), plotted against x_1/L and x_3/M. To illustrate the effects of turbulent transport due to turbulent fluctuations (*i.e.*, the term T_{ii} in equation 2.3), in each plot the time-averaged turbulent-flux components $\overline{u_1'u_3'u_3'}/(fS)^3$ and $\overline{u_3'u_3'u_3'}/(fS)^3$ have been superimposed on top of colourmaps. We note that the data from each experiment have been divided to show separately the behaviour in the near-grid region (figures 2.8a,i and 2.8b,i) and turbulent-diffusive region (figures 2.8a,ii and 2.8b,ii). In order to better resolve the structure of the flow different colour scales and vector scales have been used in these regions (see caption for details). Only every third vector (in each direction) has been shown to avoid data saturation, and for reference the grid is shown at the lowest point of its oscillation, with the location of the inner-box sidewalls indicated by the vertical black lines.

[¶]N.B. McCorquodale and Munro (2017a) is shown in chapter 3

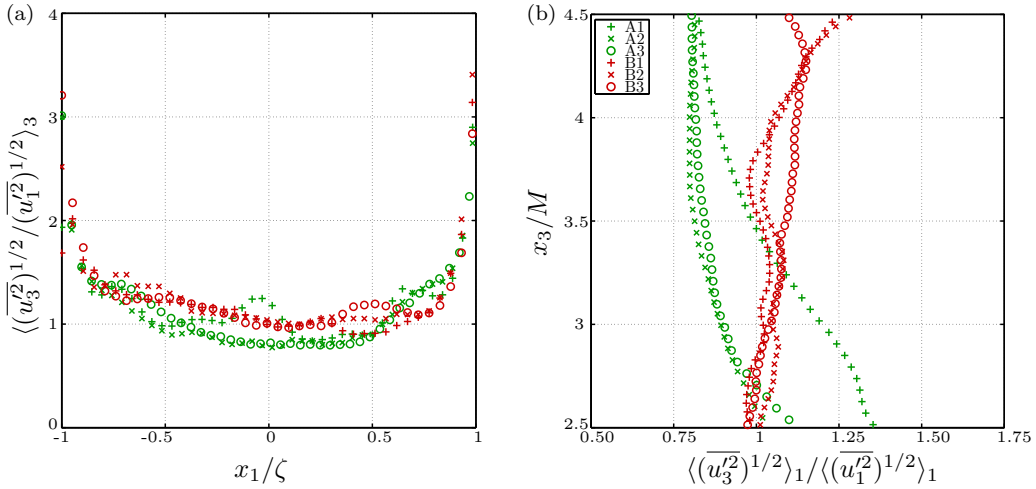


Figure 2.7: (a) Plot showing spatially averaged (in the x_3-direction) measurements of the degree of isotropy $\langle(\overline{u_3'^2})^{1/2}/(\overline{u_1'^2})^{1/2}\rangle_3$ plotted against the horizontal x_1 coordinate which has been scaled by ζ, where ζ is equal to the half-width of the outer-box for Experiments A1-A3 and $\zeta = L$ for Experiments B1-B3. To prevent over-saturation only every third data point has been plotted for each experiment. (b) Plot showing spatially averaged (in the x_1-direction) measurements of the degree of isotropy $\langle(\overline{u_3'^2})^{1/2}\rangle_1/\langle(\overline{u_1'^2})^{1/2}\rangle_1$, plotted against normalised distance below the grid x_3/M. To prevent over-saturation only every second data point has been plotted for each experiment. The data for all conditions are shown separately [see legend in (b), which applies to both plots].

Figure 2.8(a,i) shows that close to the grid (and in the absence of an inner box) peak values of $(\overline{u_3'^2})^{1/2}$ are observed along the axes of the jets that form in this region, with maximum values attained at $x_1/L \approx \pm 1$, coincident with the axis of the merged outer jets. These effects can be attributed to turbulent production as the mean kinetic energy of the jets is converted to TKE; these regions exhibit the largest spatial gradients of mean velocity and consequently the largest values of the production term Φ_{ii}. Note, however, that since the merged outer jets are more energetic than the jets over the central region ($|x_1/L| \lesssim 0.6$) there is greater production of TKE near the edge of the grid than near the centre of the grid. As a result the turbulence produced within the near-grid region is strongly inhomogeneous on horizontal planes.

Further below the grid, as the jet structures spread and break down in the grid-normal direction, $(\overline{u_3'^2})^{1/2}$ exhibits a more uniform structure over the central region of the tank ($|x_1/L| \lesssim 0.65$), as the bottom of the near-grid region is approached. However, over this region a rapid reduction in the magnitude of $(\overline{u_3'^2})^{1/2}$ occurs. This is attributed to the effects of transport of turbulent energy due to the mean flow (A_{ii}^d); the approximately uniform upwards-directed mean flow in the turbulence diffusive region (identified previously in figure 2.3) advects turbulence of low TKE up towards the near-grid region where it interacts with the (more energetic) turbulence produced by grid. Conversely, the merged outer jets do not fully breakdown within the near-grid region,

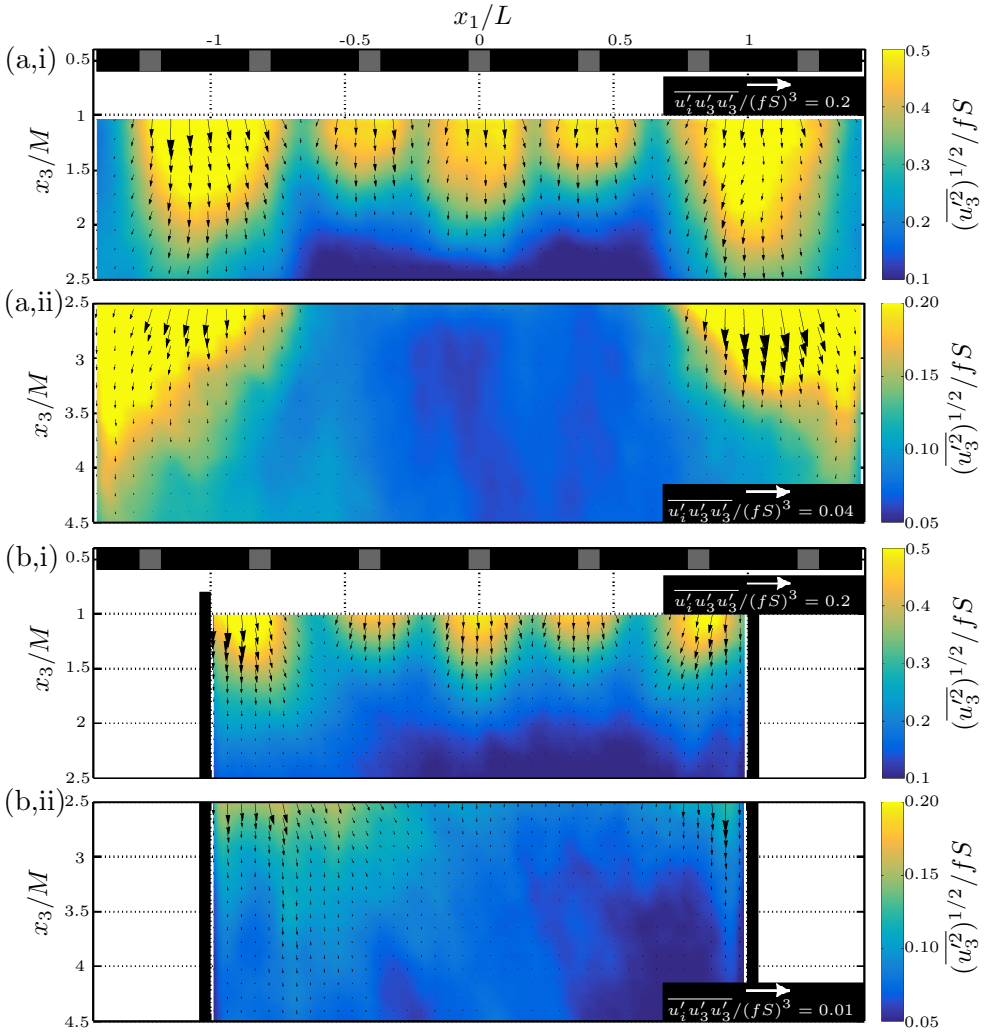


Figure 2.8: Vector plots showing the time-averaged components of turbulent energy flux $\overline{u_i'u_3'u_3'}/(fS)^3$ (where $i = 1, 3$ denote the horizontal and vertical flux respectively), which have been superimposed on top of colourmaps showing the vertical rms velocity field $(\overline{u_3'^2})^{1/2}/fS$. The data are from (a) Experiment A2 and (b) Experiment B2 (with $Re = 4050$ and $f = 3.6\,\mathrm{Hz}$ in both cases). In order to provide a meaningful scale throughout the flow the data for each experiment has been plotted over two sub-figures. Color scales and reference energy flux vectors are provided in each sub-figure; note the different scales used. To prevent an over saturation of data, only every third velocity vector has been included. For reference the grid is shown at the lowest point within its oscillation.

but instead propagate (albeit diminished in strength) to $x_3/M \approx 4$, as shown in figure 2.8(a,ii). Figure 2.8(a,ii) indicates that these outer jets are, at least in part, maintained by the transport of turbulent energy by the turbulent fluctuations (T_{ii}). That is, the larger flux of turbulent energy close to the tank side walls than in the centre of the tank contributes to the inhomogeneity across the horizontal plane that exists in the turbulent diffusive region. In turn, the horizontal inhomogeneity results in concentrated transport of energy close to the tank walls, preserving the structure of the outer jets.

For comparison, figure 2.8(b) shows corresponding data obtained with the inner box installed (in the 'optimal' position). In accordance with the results in figure 2.8(a) (Experiment A2), peak values of $(\overline{u_3'^2})^{1/2}$ are observed along the axes of the jets that form in this region. However, when the individual jets of approximately uniform strength break down, the turbulent production has a more regular structure across the entire width of the inner box. That is, terms of the form $\partial\overline{u}_i/\partial x_j$ are of approximately equal magnitude in regions coincident with each jet, such that the production term Φ_{ii} exhibits a regular structure within the inner box. As a result, figure 2.8(b) indicates the turbulence produced within the near-grid region is more homogeneous than when the inner box was absent. In addition, the weak mean flow within the turbulent-diffusive region gives rise to smaller production terms than for experiment A2 and, in comparison, a slight reduction in the magnitude of $(\overline{u_3'^2})^{1/2}$ throughout the near-grid region. Note, however, that the reduction in mean-flow intensity also inhibits the transport effects due to the mean flow (A_{ii}^d) that were identified for Experiment A2 at the edge of the near-grid region. As a result of the more homogeneous turbulence produced in the near-grid region, the coherent jet structures remain mostly confined to the near-grid region. That is, the turbulent energy flux is significantly reduced in magnitude close to the tank side walls, relative to experiments with no inner box installed (recall that different vector scales for energy flux are used in figures 2.8a,ii and 2.8b,ii), such that T_{ii} is more uniform across horizontal planes. Note however that figure 2.8(b) does indicate that there remains a weak preferential transport of turbulent energy close to the tank walls (relative to the center of the tank). This indicates that some intermittent jet structures may still exist close to the side walls when the inner box is installed, albeit in a much less energetic form than when no inner box is installed. Inspection of the instantaneous velocity fields confirms the presence of intermittent energetic structures in the turbulent-diffusive region that originate from coherent jets in the near-grid region, although these intermittent structures are not confined to regions close to the inner box sidewalls and are also present within the central region of the tank. Example flow fields (time-averaged over a period of 0.3 seconds) illustrating the intermittent energetic structures observed are shown in figure 2.9(a).

Inspection of the measured velocity fields also confirms the presence of 'splats' and 'antisplats' within the turbulent-diffusive region close to the inner box sidewalls. That is, a 'splat' is a conceptualised element of fluid that is blocked as it travels towards the boundary; the blocking of these fluid elements results in high instantaneous dynamic pressure and a corresponding transfer of energy from the boundary-normal velocity component to the boundary-tangential velocity components (Perot and Moin, 1995a). The collision of fluid elements travelling tangential to the boundary has been proposed to give rise to similar events, so-called 'antisplats' (Perot and Moin, 1995a), in which the collision of elements results in high instantaneous dynamic pressure and a transfer of

energy from boundary-tangential velocity components to the boundary-normal velocity component as the fluid elements eject from the boundary. These flow features are of direct interest as the balance of splats and antisplats has been proposed to govern the net intercomponent energy transfer that occurs during the interaction of zero-mean-shear turbulence and a solid impermeable boundary (Perot and Moin, 1995a; Bodart et al., 2010). Consistent with observations of previous studies (Bodart et al., 2010), here antisplats and splats are regularly observed to form simultaneously along adjacent regions of the inner box sidewalls, as shown in figure 2.9(b,c). This observation is thought to be a result of the no-slip condition enforced by solid boundaries; as a splat is blocked by a boundary, the no-slip conditions result in instantaneous shear and the vorticity associated with this shear acts to eject fluid away from the boundary (Bodart et al., 2010; Hunt and Morrison, 2000).

Finally, for experiments A and B we compare measurements of the key turbulence statistics ($(\overline{u_1'^2})^{1/2}$, $(\overline{u_3'^2})^{1/2}$ and $\bar{\ell}$) with the standard model given in equation (2.1). For the purposes of these comparison, attention is restricted to the turbulent-diffusive region (*i.e.*, $2.5M \leqslant x_3 \leqslant 4.5M$), with the anisotropic near-sidewall regions excluded.

Figure 2.10(a) and 2.10(b) show spatially averaged measurements of the $\langle(\overline{u_1'^2})^{1/2}\rangle_1$ and $\langle(\overline{u_3'^2})^{1/2}\rangle_1$, from experiments A and B, plotted against depth x_3; recall that $\langle\cdot\rangle_1$ is used to denote the spatial average in the x_1-direction across the central region of the container, away from the anisotropic sidewall regions (*i.e.*, $|x_1/\zeta| \lesssim 0.5$, where $\zeta = 17.6\,\text{cm}$ for experiments A and $\zeta = L$ for experiments B). The data in figures 2.10(a) and 2.10(b) have been plotted on log scale, in a dimensionless form according to equations (2.1a) and (2.1b). Also shown are errors bar indicating uncertainty within the experimental measurements. That is, uncertainty arises in our measurements as a result of noise inherent within PIV algorithms; a state-of-the-art planar PIV system is capable of measuring fluid velocity with an estimated uncertainty of approximately 1-2% (Westerweel et al., 2013). However, the reliability of velocity measurements is dependent upon the accuracy with which PIV algorithms are able to determine particle displacement between successive images. Accurate particle displacements are only obtained when a distinct peak is identified within the autocorrelation analysis, indicating that there is a strong local correlation between interrogation windows in successive images. The correlation between interrogation windows depends upon a great many factors, including the concentration of seeding particles, the thickness of the light sheet and the velocity shear (Keane and Adrian, 1990). Here the thickness of the light sheet, concentration of seeding particles and interrogation window size were adjusted using established design criteria (Keane and Adrian, 1990) so as to reduce uncertainty. In addition, recall that regions close to the grid and tank side walls in which the PIV analysis mostly returned spurious velocity vectors, as a result of poor local correlation between interrogation windows in successive images, have been discarded.

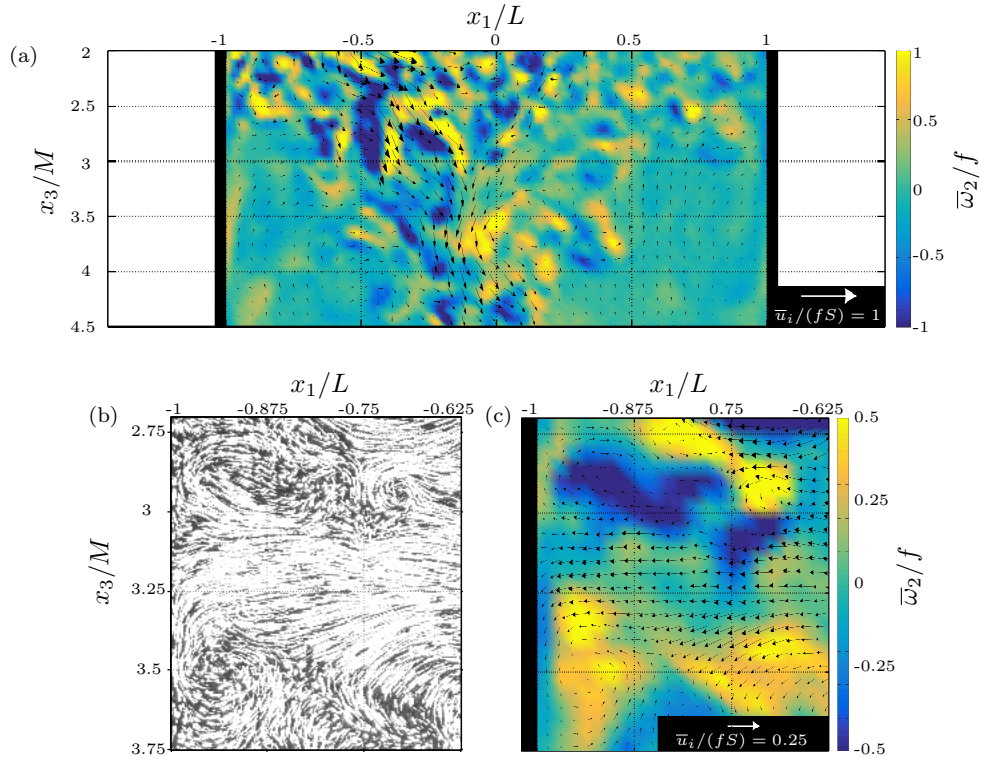


Figure 2.9: Experiment B1 ($Re = 2020, f = 1.6\,Hz$). (a) Vector plot of velocity components $\overline{u}_i/fS$ together with the corresponding vorticity component $\overline{\omega}_2/f$, showing an example of intermittent energetic structures observed within the turbulent-diffusive region. To prevent over-saturation only every third velocity vector has been included. (b) Streak image and (c) corresponding vector plot of velocity components $\overline{u}_i/fS$ together with the corresponding vorticity component $\overline{\omega}_2/f$, showing an example of splat and antisplat formation on the inner box sidewall. The splat (centered at $x_3/M \approx 3.1$) gives rise to two antisplats of opposite vorticity (centered at $x_3/M \approx 2.9$ and 3.5) as it impacts onto the inner box sidewall at $x_1/L = -1$. A reference velocity scale and vorticity scale has been included in each of panels (a) and (c), note the different scales used. Note that in panels (a) and (c) the overbar is used to denote a time average over a period of 0.3 seconds only.

However, a notable source of uncertainty in OGT arises from the variability that occurs across measurements of the flow in experiments repeated under nominally identical conditions. In particular, McKenna and McGillis (2004) showed that the measured magnitude of mean-flow components and turbulent fluctuations vary by as much as 25% and 15%, respectively, across separate experiments performed under the same conditions. These variations between repeat experiments are too large to be attributed to measurement uncertainty alone and must arise, at least in part, from differences in the structure of the flows produced. Estimates of uncertainty associated with this variability within the current apparatus have been determined using data reported by McCorquodale and Munro (2017c)[§]. That is, McCorquodale and Munro (2017c)[§] reported measurements

[§]N.B. McCorquodale and Munro (2017c) is shown in chapter 4

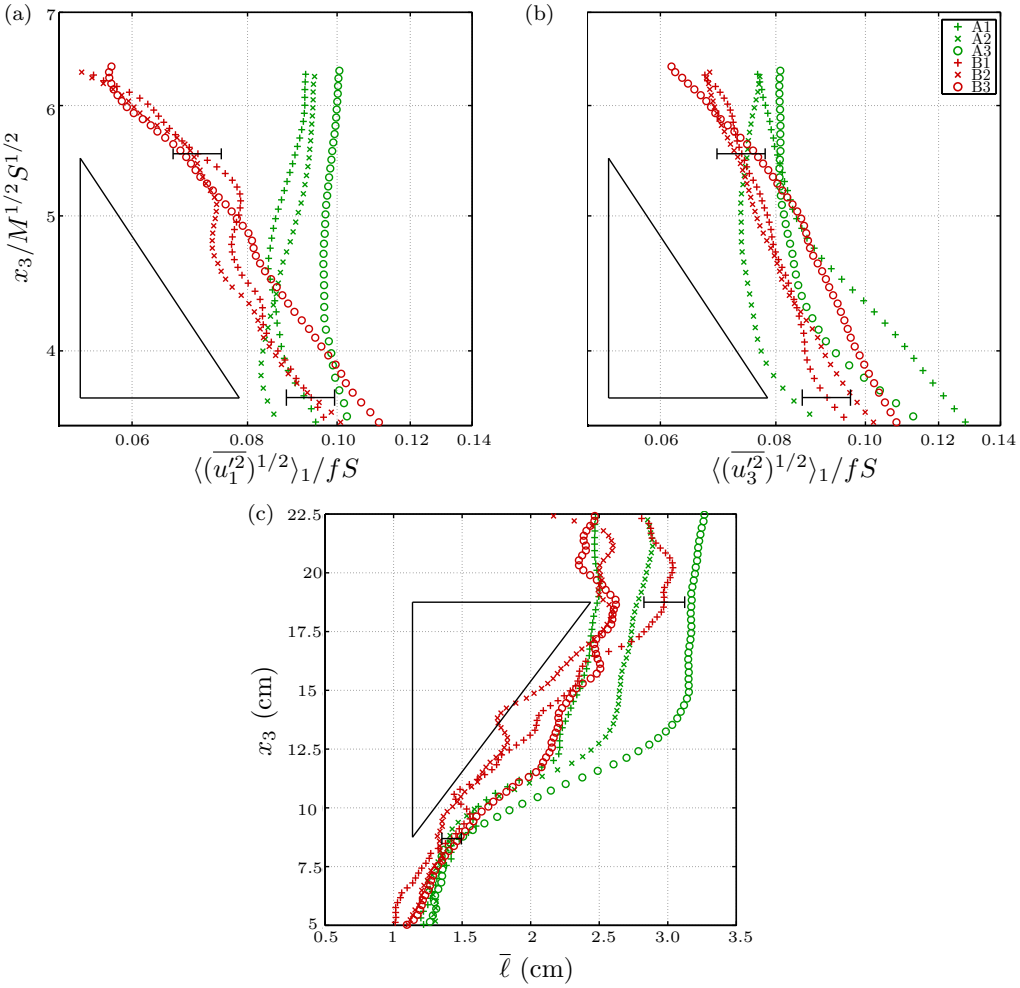


Figure 2.10: (a,b) Spatially averaged (in the x_1-direction) measurements of the rms velocity components $\langle(\overline{u_1'^2})^{1/2}\rangle_1$ and $\langle(\overline{u_3'^2})^{1/2}\rangle_1$ plotted against x_3; the quantities have been scaled in accordance with equation (2.1). The slope in each plot shows the spatial decay $\propto x_3^{-1}$. (c) Computed values of the time-averaged integral length scale, $\overline{\ell}$ plotted against normalised distance below the grid x_3. The slope shows the equation (2.1c) with empirical constant $C_2 = 0.13$. The data for all conditions are shown separately [see legend in (b), which applies to all plots]. In each plot two error bars are shown for condition B1 only; these error bars are representative of all conditions.

of five ensembles of experiments repeated under nominally identical conditions. The standard deviations of the corresponding measurements of $\langle(\overline{u_1'^2})^{1/2}\rangle_1$ and $\langle(\overline{u_3'^2})^{1/2}\rangle_1$, denoted $\sigma_{u_1'}$ and $\sigma_{u_3'}$, computed across each ensemble were given by $\sigma_{u_1'} \approx 0.06\langle(\overline{u_1'^2})^{1/2}\rangle_1$ and $\sigma_{u_3'} \approx 0.06\langle(\overline{u_3'^2})^{1/2}\rangle_1$. These estimates of uncertainty are shown as the error bars in figure 2.10(a) and 2.10(b). To prevent oversaturation, error bars are shown for condition B1 only; these error bars are representative of all conditions.

The data in figure 2.10(a) and 2.10(b) show that with no inner box installed (Experiments A1-A3), equation (2.1) is a poor fit for the observed spatial decay of $(\overline{u_1'^2})^{1/2}$ and $(\overline{u_3'^2})^{1/2}$. Recall, however, that equation (2.1a) is derived from equation (2.3) under the

assumptions of zero mean flow ($A^d_{ii} = \Phi_{ii} = 0$), homogeneity (in planes parallel to the grid) and negligible viscous transport ($D_{ii} = 0$); under these conditions the turbulent transport (T_{ii}) is a dominant term. However, the data in figure 2.3 show that, with no inner box installed, the time-averaged mean flow is not negligible in the the turbulent-diffusive region, which contradicts the underlying assumptions, resulting in a poor fit; previous studies have shown that a significant mean flow can reduce the exponent of the spatial decay of $(\overline{u_1'^2})^{1/2}$ and $(\overline{u_3'^2})^{1/2}$ from approximately -1 to -0.5 (Hopfinger and Toly, 1976). In contrast, with the inner box installed in the 'optimal' position (Experiments B1-B3) the reduction in mean-flow intensity within the turbulent diffusive region results in turbulence that is in accordance with the underlying approximations made, such that the spatial decay of $(\overline{u_1'^2})^{1/2}$ and $(\overline{u_3'^2})^{1/2}$ is well described by equation (2.1). In addition, the error bars in figure 2.10(a) and 2.10(b) indicate that the degree of scatter within measured values of $\langle(\overline{u_1'^2})^{1/2}\rangle_1$ and $\langle(\overline{u_3'^2})^{1/2}\rangle_1$ across experiments B1-B3 can be understood in the context of uncertainty arising from flow variability.

The velocity measurements were also used to estimate the longitudinal integral length scale. We followed the approach used previously (Kit et al., 1997; McCorquodale and Munro, 2017a)[¶] by defining the integral length scale as the integral of the autocorrelation function of $u_1'(x_1, x_3, t)$, over the spatial lag up to which the autocorrelation function first crosses zero. The autocorrelation function, at spatial lag χ, is defined as

$$r_u(x_3, t; \chi) = \frac{c_u(x_3, t; \chi)}{c_u(x_3, t; \chi = 0)}, \tag{2.4a}$$

where

$$c_u(x_3, t; \chi) = \frac{1}{\zeta} \int_{-\zeta/2}^{\zeta/2} u_1'(x_1, x_3, t)\, u_1'(x_1 + \chi, x_3, t)\, \mathrm{d}x_1. \tag{2.4b}$$

Recall that ζ is used to denote the half-width of the outer-box for Experiments A1-A3 or the half-width of the inner box for Experiments B1-B3; that is, equation (2.4b) is an integral over the central region of the tank. The time-averaged integral length scale is then given by

$$\overline{\ell}\,(x_3) = \frac{1}{T} \int_0^T \int_0^{\chi_0} r_u(x_3, t; \chi)\, \mathrm{d}\chi\, \mathrm{d}t \tag{2.5}$$

where χ_0 denotes the spatial lag at which the autocorrelation function first becomes zero, and T is the sampling period (which, recall, here was 240 s). The corresponding estimates for $\overline{\ell}$ are shown in figure 2.10(c), plotted against the vertical coordinate x_3. The data have been plotted in dimensional form according to equation (2.1c). (For reference we recall that the turbulent-diffusion region is given by $x_3 \gtrsim 2.5M = 12.5\,\mathrm{cm}$.) Also shown are error bars, indicating the uncertainty within measured values of $\overline{\ell}$, computed using the same approach used to estimate uncertainty in measurements of $\langle(\overline{u_1'^2})^{1/2}\rangle_1$ and $\langle(\overline{u_3'^2})^{1/2}\rangle_1$. To prevent oversaturation, error bars are shown for condition B1 only; these error bars are representative of all conditions. These data show that with the

[¶]N.B. McCorquodale and Munro (2017a) is shown in chapter 3

inner box installed in the 'optimal' position (*i.e.* Experiments B1-B3) the growth of the longitudinal integral length scales are well described by equation (2.1c) using a value of $C_2 \approx 0.13$, which is consistent with previously reported values (Thompson and Turner, 1975; De Silva and Fernando, 1994; Kit et al., 1997). In addition, the error bars in figure 2.10(c) indicate that the degree of scatter within measured values of $\overline{\ell}$ across experiments B1-B3 can also be understood in the context of uncertainty arising from flow variability. We note that we have not applied a 'virtual origin correction' to the data (a process whereby the origin of the x_3 co-ordinate is redefined as the point at which the best agreement with (2.1) occurs), as although this analysis tool has been previously used in OGT (Hopfinger and Toly, 1976; Kit et al., 1997; Thompson and Turner, 1975) it provides no additional physical insight here. However, with no inner box installed (*i.e.* Experiments A1-A3) equation (2.1c) is a poor fit for the measured values of the longitudinal integral length scale.

2.4 Discussion

We have shown that the installation of an inner box in a position that inhibits the formation of the (dominant) merged outer jets can result in a significant reduction in the magnitude of the mean-flow velocity produced by OGT, but that the installation of an inner box does not completely eliminate mean flow. Hence, here we consider limitations in the use of an inner box.

Firstly, we note that the installation of the inner box in the position designated 'optimal' here was chosen as the configuration that was most effective at reducing the intensity of the mean flow during preliminary testing of inner boxes installed at different depths beneath the grid. However, in light of variations in mean flow reported in previous studies using different apparatus (Dohan and Sutherland, 2002; McKenna and McGillis, 2004; Bennett et al., 2014) (and variations in the parameters M and S used), we do not presume that the optimal position identified here is necessarily optimal (or practical) for all OGT apparatus. We stress, however, that the results presented here do indicate that installation within the near-grid region is necessary to inhibit the merging of outer jets that otherwise induce large-scale circulations. For a given apparatus, it is likely that some form of sensitivity analysis will be necessary to determine the optimal position of the inner box within the near-grid region; the grid stroke may be a limiting factor in this analysis, noting that only a relatively small grid stroke was used here.

Secondly, we consider sources, other than those identified as dominant here, that contribute to the mean flow. Recall that with no inner box installed we attributed the origin of the observed mean flow to the presence of merged outer jets that are more energetic than the jets produced below the centre of the grid, but that the installation of the inner box was found to inhibit the merged outer jets. The resulting mean flow

velocities were shown to be significantly reduced but not insignificant; we observed $|\overline{u}_3|/(\overline{u_3'^2})^{1/2} \approx 0.6$ in the turbulent-diffusive region when the inner box was installed in its 'optimal' position.

Drayton (1993) also observed intense outer jets and proposed these were a dominant factor in the generation of mean flow in OGT. However, Drayton (1993) suggested the intense outer jets arose as a result of the Coanda effect. Correspondingly, jets with axes initially coincident with the outermost grid intersections were proposed to be deflected towards the boundary and subsequently merge in the boundary-tangential direction. This represents a distinctly different jet structure than that observed in the experiments reported here. However, recall that the intense outer jets reported by Drayton (1993) had a wall normal thickness of approximately $2M$, which is consistent with results shown in figure 2.3 and suggests that in Drayton's study a merging of jets normal to the tank walls must also occur (in addition to jet merging in the boundary-tangential direction). Thus, both this study and that of Drayton (1993) exhibit a number of similar features regarding the jet-merging process. Consequently, in light of these similarities and noting the limitations inherent when using 2D data to analyse a clearly 3D flow, it is possible that the Coanda effect identified by Drayton (1993) may contribute to the jet-merging process identified here. Indeed, note that the data in figure 2.8(a,ii) indicate that the axes of the intermittent energetic outer jets were deflected towards the container sidewalls within the turbulent-diffusive region. This observation is consistent with the Coanda effect and indicates that this phenomenon may contribute to mean flow in OGT. In addition, when the inner box is installed (in its optimal position), although the formation of intense intermittent outer turbulent jets in the turbulent-diffusive region is inhibited (see figure 2.8), there remains a weak preferential transport of turbulent energy close to the tank walls (relative to the center of the tank) in these experiments. However, in this case (*i.e.* for Experiments B1-B3) the absence of energetic jet structures close to the tank walls in the turbulent diffusive region indicates that Coanda effects are also inhibited and therefore that the contribution of this effect to the observed mean flow may be small in these experiments. This can be attributed to the inclined angle at which the grid-induced jets at $x_1/L \approx \pm 0.8$ initially propagate (see figure 2.4) within the near-grid region; the Coanda effect is inhibited when the separation between the jet and the boundary increases to an oblique angle (Song et al., 2000).

In addition, the steady Reynolds momentum equation, which takes the form (Tennekes and Lumley, 1972, p.32)

$$\overline{u}_j \frac{\partial \overline{u}_i}{\partial x_j} = -\frac{1}{\rho}\frac{\partial \overline{p}}{\partial x_i} + \frac{\partial}{\partial x_j}\left(-\overline{u_i' u_j'}\right) + \nu \frac{\partial^2 \overline{u}_i}{\partial x_j \partial x_j}. \tag{2.6}$$

indicates that mean flow can be induced as a result of spatial gradients in the Reynolds-stresses induced by the grid's oscillation (Fernando and De Silva, 1993; Drayton, 1993). It has been proposed that designing a grid such that the tank walls act as a plane of

symmetry to the grid minimises spatial gradients in the Reynolds stress tensor (away from the grid) and therefore may reduce mean flow present in OGT (Fernando and De Silva, 1993). However, spatial gradients in the Reynolds stress tensor cannot be eliminated close to the sidewalls as a result of inhibiting boundary conditions imposed (see figure 2.6), which may induce mean flow even when the inner box is installed in its optimal position. It appears this effect may be an unavoidable result of the boundary conditions imposed by the use of a finite-sized container for OGT (Drayton, 1993). This effect is discussed in greater detail in Drayton (1993) and in a broader context the study of Nagata et al. (2006).

Use of a rigid lid in the current apparatus inhibits other phenomenon that have been reported to give rise to mean flow in OGT, such as oscillation of a free surface (due to standing waves from grid forcing) (Drayton, 1993) and convection rolls driven by evaporation from the free surface (Honey et al., 2014; Voropayev and Fernando, 1996). Intense mean flow has also been reported in tanks with a large depth-to-width aspect ratio (Dohan and Sutherland, 2002), which were attributed to the production of quasi-two-dimensional turbulence (anisotropy at large scales) which could promote large scale circulating cells (Dohan and Sutherland, 2002). However, this does not appear to be of significance here; that is, the installation of the inner box increases the aspect ratio of the region of interest but significantly reduces the intensity of the mean flow.

2.5 Conclusions

We have presented experimental data describing a mechanism for the inception of mean flow in OGT, the means by which the magnitude of the mean flow can be reduced by use of an 'inner box' and the corresponding effect this has on the structure of the turbulence produced. Visualisation of the mean flow close to an oscillating grid, using 2D PIV data, indicates that the grid generates a regular structure of jets (away from the tank side walls) that break down to promote turbulence, confirming the recognised structure of OGT. However, a combination of grid edge effects and sidewall effects (viscous and no-penetration) cause a deflection, and subsequent merging in the boundary-normal direction, of the jets produced below the perimeter region of the grid. These merged outer jets are more intense than those produced at the centre of the grid and give rise to large-scale circulations within the container.

Installation of an opened-ended inner box, positioned symmetrically below the grid with its sidewalls equidistant between the two outermost grid intersections and with its top edge 1 cm below the bottom of the grid's oscillation, was shown to inhibit the formation of the these merged outer jets and reduce mean flow velocities within the inner box. Remaining sources of mean flow within the inner box are sufficiently weak that turbulent fluctuations are the dominant component of the flow; measurements indicated

that the 'mean flow intensity' (the ratio of the mean flow velocity component to the rms velocity component) was reduced from approximately 3.5 for experiments with no inner box installed to approximately 0.6 when the inner box was installed. Contrary to previous suggestions (Drayton, 1993), the positioning of the inner box with its top edge located further below the grid has been shown to be less effective at reducing the intensity of the observed mean flow.

Analysis of the spatial distribution of turbulent energy and turbulent energy flux indicates that close to the sidewalls of the container OGT is strongly anisotropic and inhomogeneous. However, the correct installation of the inner box results in turbulence that is a good approximation to homogeneous and isotropic conditions, on horizontal planes parallel to the grid, over the central 50% of the inner box's width. Data are also presented to evaluate whether the installation of an inner box results in turbulence, within the turbulent diffusion-region, that is in good accordance with the widely used idealised model. Results indicate that the degree of isotropy, the spatial decay of the rms turbulent velocity components and integral length scale are well described by the standard empirical model (equation 2.1) when the inner box is installed, but that the intense mean flow in experiments conducted with no inner box installed can result in turbulence for which equation (2.1) is a poor description.

We anticipate that this simple amendment to reduce the mean flow present in OGT can be readily used in future work that utilises OGT to isolate the effects of turbulent fluctuations from those of the mean flow.

Acknowledgements

The authors acknowledge Jim Meakin and Steve Lawton for technical support with the experimental apparatus. MWM acknowledges financial support through an Engineering and Physical Sciences Research Council Studentship (number 1510466).

References

Al-Homoud, A. and Hondzo, M. (2007). Energy dissipation estimates in oscillating grid setup: LDV and PIV measurements. *Environ Fluid Mech*, 7:143–158.

Bennett, S. J., Hou, Y., and Atkinson, J. F. (2014). Turbulence suppression by suspended sediment within a geophysical flow. *Environ Fluid Mech*, 14:771–794.

Bodart, J., Cazalbou, J. B., and Joly, L. (2010). Direct numerical simulation of unsheared turbulence diffusing towards a free-slip or no-slip surface. *J. Turbul.*, 11(48):1–18.

Brumley, B. H. and Jirka, G. H. (1987). Near-surface turbulence in a grid-stirred tank. *J. Fluid Mech.*, 183:235–263.

Brunk, B. K., Koch, D. L., and Lion, L. W. (1998). Observations of coagulation in isotropic turbulence. *J. Fluid Mech.*, 371:81–107.

Cheng, N. S. and Law, A. W. K. (2001). Measurements of turbulence generated by oscillating grid. *J. Hydraul. Eng.*, 127:201–208.

Dalziel, S. B. (2006). Digiflow user guide: http://www.damtp.cam.ac.uk/lab/digiflow/.

De Silva, I. P. D. and Fernando, H. J. S. (1994). Oscillating grids as a source of nearly isotropic turbulence. *Phys. Fluids*, 6:2455–2464.

De Silva, I. P. D. and Fernando, H. J. S. (1998). Experiments on collapsing turbulent regions in stratified fluids. *J. Fluid Mech.*, 358:29–60.

Di Marco, A., Mancinelli, M., and Camussi, R. (2015). Pressure and velocity measurements of an incompressible moderate Reynolds number jet interacting with a tangential flat plate. *J. Fluid Mech.*, 770:247–272.

Dickinson, S. C. and Long, R. R. (1983). Oscillating-grid turbulence including effects of rotation. *J. Fluid Mech.*, 126:315–333.

Dohan, K. and Sutherland, B. R. (2002). Turbulence time scales in mixing box experiments. *Exp. Fluids*, 33:709–719.

Drayton, M. J. (1993). *Eularian and Lagrangian Studies of Inhomogeneous Turbulence Generated by an Oscillating Grid.* PhD thesis, King's College, University of Cambridge.

Fernando, H. J. S. and De Silva, I. P. D. (1993). Note on secondary flows in oscillating grid, mixing box experiments. *Phys. Fluids*, 5:1849–1851.

Fernando, H. J. S. and Long, R. R. (1983). The growth of a grid-generated turbulent mixed layer in a two-fluid system. *J. Fluid Mech.*, 133:377–395.

Fernando, H. J. S. and Long, R. R. (1985). On the nature of the entrainment interface of a two-layer fluid subjected to zero-mean-shear turbulence. *J. Fluid Mech.*, 151:21–53.

Hannoun, I. A., Fernando, H. J. S., and List, E. J. (1988). Turbulence structure near a sharp density interface. *J. Fluid Mech.*, 189:189–209.

Hannoun, I. A. and List, E. J. (1988). Turbulent mixing at a shear-free density interface. *J. Fluid Mech.*, 189:211–234.

Hinze, J. O. (1975). *Turbulence.* McGraw-Hill, 2nd edition.

Honey, R. E., Hershberger, R., Donnelly, R. J., and Bolster, D. (2014). Oscillating-grid experiments in water and superfluid helium. *Phys Rev E*, 89:053016.

Hopfinger, B. J. and Linden, P. F. (1982). Formation of thermoclines in zero-mean-shear turbulence subjected to a stabilizing buoyancy flux. *J. Fluid Mech.*, 11:157–173.

Hopfinger, B. J. and Toly, J. A. (1976). Spatially decaying turbulence and its relation to mixing across density interfaces. *J. Fluid Mech.*, 78(1):155–175.

Hunt, J. C. R. and Graham, J. M. R. (1978). Free-stream turbulence near plane boundaries. *J. Fluid Mech.*, 84(2):209–235.

Huppert, H. E., Turner, J. S., and Hallworth, M. A. (1995). Sedimentation and entrainment in dense layers of suspended particles stirred by an oscillating grid. *J. Fluid*

Mech., 289:263–293.

Keane, R. D., and Adrian, R. J. (1990). Optimization of partilce image velocimeters. Part 1: Double pulsed systems. *Meas. Sci. Technol.*, 1:1202–1215.

Kim, D. S., Yoon, S. H., Lee, D. H., and Kim, K. C. (1996). Flow and heat transfer measurements of a wall attaching offset jet. *Int. J. Heat Mass Transfer.*, 39:2907–2913.

Kit, E., Fernando, H. J. S., and Brown, J. A. (1995). Experimental examination of Eulerian frequency spectra in zero-mean-shear turbulence. *Phys. Fluids*, 7(5):1168–1170.

Kit, E. L. G., Strang, E. J., and Fernando, H. J. S. (1997). Measurement of turbulence near shear-free density interfaces. *J. Fluid Mech.*, 334:293–314.

Lucas, S., Moulin, F., and Guizien, K. (2016). Oscillating grid mesocosm for studying oxygen dynamics under controlled unsteady turbulence. *Limnol. Oceanogr.: Methods*, 14:1–13.

Masaló, I., Guadayol, Ò., Peters, F., and Oca, J. (2008). Analysis of sedimentation and resuspension processes of aquaculture biosolids using an oscillating grid. *Aquacultural Engineering*, 38:135–144.

McCorquodale, M. W. and Munro, R. J. (2017a). Experimental study of oscillating-grid turbulence interacting with a solid boundary. *J. Fluid Mech.*, 813:768–798.

McCorquodale, M. W. and Munro, R. J. (2017c). Analysis of intercomponent energy transfer in the interaction of oscillating-grid turbulence with an impermeable boundary. *Submitted to: Phys. Fluids.*

McDougall, T. J. (1979). Measurements of turbulence in a zero-mean-shear mixed layer. *J. Fluid Mech.*, 94(3):409–431.

McGrath, J. L., Fernando, H. J. S., and Hunt, J. C. R. (1997). Turbulence, waves and mixing at shear-free density interfaces. Part 2. laboratory experiments. *J. Fluid Mech.*, 347:235–261.

McKenna, S. P. and McGillis, W. R. (2004). Observations of flow repeatability and secondary circulation in an oscillating grid-stirred tank. *Phys. Fluids*, 16(9):3499–3502.

Medina, P., Sánchez, M. A., and Redondo, J. M. (2001). Grid stirred turbulence: Applications to the initiation of sediment motion and lift-off studies. *Phys. Chem. Earth (B)*, 26(4):299–304.

Miozzi, M., Lalli, F., and Romano, G. P. (2010). Experimental investigation of a free-surface turbulent jet with coanda effect. *Exp. Fluids*, 49:341–353.

Nagata, K., Wong, H., Hunt, J. C. R., Sajjadi, S. G., and Davidson, P. A. (2006). Weak mean flows induced by anisotropic turbulence impinging onto planar and undulating surfaces. *J. Fluid Mech.*, 556:329–360.

Nokes, R. I. (1988). On the entrainment rate across a density interface. *J. Fluid Mech.*, 188:185–204.

Orlins, J. J. and Gulliver, J. S. (2003). Turbulence quantification and sediment resuspension in an oscillating grid chamber. *Exp. Fluids*, 34:662–677.

Perot, B. and Moin, P. (1995). Shear free turbulent boundary layers, Part 1, physical insights into near-wall turbulence. *J. Fluid Mech.*, 295:199–227.

Sawyer, R. A. (1960). The flow due to a two-dimensional jet issuing parallel to a flat plate. *J. Fluid Mech.*, 9:543–561.

Song, H. B., Yoon, S. H., and Lee, D. H. (2000). Flow and heat transfer characteristics of a two-dimensional oblique wall attaching offset jet. *Int. J. Heat Mass Transfer.*, 43:2395–2404.

Tennekes, H. and Lumley, J. L. (1972). *A first course in turbulence*. MIT press, 1st edition.

Thompson, S. M. and Turner, J. S. (1975). Mixing across an interface due to turbulence generated by an oscillating grid. *J. Fluid Mech.*, 67(2):349–368.

Turner, J. S. (1968). The influence of molecular diffusivity on turbulent entrainment across a density interface. *J. Fluid Mech.*, 33(4):639–656.

Voropayev, S. I. and Fernando, H. J. S. (1996). Propagation of grid tubulence in homogneneous fluids. *Phys. Fluids*, 8:2435–2440.

Wan Mohtar, W. H. M. and Munro, R. J. (2013). Threshold criteria for incipient sediment motion on an inclined bedform in the presence of oscillating-grid turbulence. *Phys. Fluids*, 25:015103.

Xuequan, E. and Hopfinger, E. J. (1986). On mixing across an interface in stably stratified fluid. *J. Fluid Mech.*, 166:227–244.

Chapter 3

Experimental study of oscillating-grid turbulence interacting with a solid boundary

This chapter is comprised of an article published by the Journal of Fluid Mechanics. Article reference:

> McCorquodale, M. W. and Munro, R. J. (2017). Experimental study of oscillating-grid turbulence interacting with a solid boundary. *Journal of Fluid Mechanics*, 813:768-798.

For copyright reasons the published paper is not reproduced here in its final form, instead the raw material of the paper is exactly reproduced within this chapter with the exception of the following amendments:

1. Section and figure numbers are amended to include a chapter reference to ensure consistency across the thesis.
2. Reference to journal details (publisher, volume, page numbers, DOI etc) have not been included
3. Contact details for corresponding authors have not been included
4. Dates of submission, revision and acceptance have not been included
5. Footnotes are included to facilitate references to other chapters of the thesis

Nomenclature

C_1, C_2, C_3, C_u, C_w	Empirical constants
f	Grid oscillation frequency
H	Distance between false-floor and grid's mean position
k_w	Wavenumber
ℓ	Longitudinal integral length scale
ℓ_w	Transverse integral length scale
ℓ_0	Reference integral length scale
l_f	Characteristic length scale used by Bodart et al. (2010)
L	Half-width of inner box
M	Mesh spacing
n	Number of repeats of an experiment
p, P, p'	Instantaneous/(time-averaged) mean/fluctuating pressure
$\overline{q'^2} \equiv \overline{u_i' u_i'}/2$	Turbulent kinetic energy per unit mass
$\overline{q_0'^2}$	Regression best fit of $\overline{q'^2}$
$\overline{q_{0,\ell_0}'^2}$	Value of $\overline{q_0'^2}$ evaluated at $\xi = \ell_0$
$Re \equiv u\ell/\nu$	Turbulent Reynolds number
$Re_G \equiv MSf/\nu$	Grid Reynolds number
$Re_T \equiv \overline{q'^4}/\nu\varepsilon$	Reynolds number
r_u, r_w, c_u	Autocorrelation functions
S	Grid stroke
t	Time
T	Sampling period (4 minutes)
u_i	Instantaneous velocity component
$u_i' \equiv u_i - U_i$	Turbulent velocity component
$U_i \equiv \overline{u}_i$	(Time-averaged) mean velocity component
$u \equiv \overline{u_1'^2}^{1/2}$, $v \equiv \overline{u_2'^2}^{1/2}$, $w \equiv \overline{u_1'^3}^{1/2}$	Root-mean-square turbulent velocity component
u_0, v_0, w_0	Regression best fit of u, v, w
u_{0,ℓ_0}	Value of u_0 evaluated at $\xi = \ell_0$
x_1, x_2, x_3	Co-ordinate system with origin at center of grid's mean position
$\gamma, \gamma_u, \gamma_w$	Empirical constant
δ_s	Thickness of boundary-affected region
ε	Dissipation per unit mass
ν	Kinematic viscosity
$\xi \equiv H - x_3$	Distance normal to and above false floor
ρ	Density

$\sigma \equiv \overline{u_3' u_3' u_3'}/w^3$	Skewness of u_3'
χ	Variable denoting spatial lag used within autocorrelation analysis
A_{ij}^d	Transport due to the mean flow
Φ_{ij}	Production due to the mean flow
T_{ij}	Transport by velocity fluctuations
Π_{ij}^d	Transport by pressure fluctuations
Π_{ij}^s	Pressure-strain correlation (Intercomponent energy transfer)
D_{ij}	Molecular diffusion
ε_{ij}	Viscous dissipation
$\overline{p}$	Time-average of quantity p
$\lvert p \rvert$	Magnitude of quantity p
$\langle p \rangle_i$	Spatial average of quantity p in the ith direction

Experimental study of oscillating-grid turbulence interacting with a solid boundary

Mark W. McCorquodale[1] **and R. J. Munro**[1]

[1]Faculty of Engineering, The University of Nottingham, Nottingham NG7 2RD, UK

The interaction between oscillating-grid turbulence and a solid, impermeable boundary (positioned below, and aligned parallel to the grid) is studied experimentally. Instantaneous velocity measurements, obtained using two-dimensional particle imaging velocimetry in the vertical plane through the centre of the (horizontal) grid, are used to study the effect of the boundary on the root-mean-square velocity components, the vertical flux of turbulent kinetic energy (TKE) and the terms in the Reynolds stress transport equation. Identified as a critical aspect of the interaction is the blocking of a vertical flux of TKE across the boundary-affected region. Terms of the Reynolds stress transport equations show that the blocking of this energy flux acts to increase the boundary-tangential turbulent velocity component, relative to far-field trend, but not the boundary-normal velocity component. The results are compared with previous studies of the interaction between zero-mean-shear turbulence and a solid boundary. In particular, the data reported here are in support of viscous and 'return-to-isotropy' mechanisms governing the intercomponent energy transfer previously proposed, respectively, by Perot & Moin [*J. Fluid Mech.*, vol. 295, 1995, pp. 199–227] and Walker *et al.* [*J. Fluid Mech.*, vol. 320, 1996, pp. 19–51], although we note that these mechanisms are not independent of the blocking of energy flux and draw parallels to the related model proposed by Magnaudet [*J. Fluid Mech.*, vol. 484, 2003, pp. 167–196].

3.1 Introduction

In the study of turbulent flows the interaction of turbulence with a solid boundary has long been a topic of interest. Uzkan and Reynolds (1967) noted that the presence of a boundary acts both directly, in inhibiting the turbulent fluctuations in the vicinity of the boundary, and indirectly, through the production of new turbulence, by assisting in the maintenance of mean velocity gradients. As a result, Uzkan and Reynolds (1967) sought to isolate the first, direct, effect on the turbulent fluctuations, in doing so giving rise to the study of the interaction of zero-mean-shear isotropic turbulence with a solid boundary. This simplified interaction benefits from eliminating the effects of mean shear that could mask other more subtle aspects of the interaction. However, nearly 50 years later the study of this problem continues and several issues remain contentious. Here, we report results from experiments using oscillating-grid turbulence to explore the

interaction of turbulence with a solid boundary and cast further light on the interaction between zero-mean-shear turbulence and a boundary.

The earliest studies of the interaction of a solid boundary with a zero-mean-shear isotropic turbulent field are by Uzkan and Reynolds (1967) and Thomas and Hancock (1977). Both used similar 'moving belt' configurations. Here, a turbulent flow in an open channel, generated using a fixed vertical grid positioned normal to the horizontal mean flow direction, flows over a horizontal wall that moves at the same speed (and in the same direction) as the mean-flow. The turbulence adjacent to the moving boundary is free to evolve as it is advected downstream. The boundary-normal root-mean-square (rms) turbulent velocity, $w = (\overline{u_3'^2})^{1/2}$, was found to be monotonically reduced in magnitude to zero from its free-stream value over a distance from the boundary of approximately one integral length scale (Thomas and Hancock, 1977). At low Reynolds number ($Re_T \equiv \overline{q'^4}/\nu\varepsilon \approx 90$; $\overline{q'^2}$ denotes turbulent kinetic energy per unit mass, ν denotes kinematic viscosity and ε denotes dissipation per unit mass), Uzkan and Reynolds (1967) found that the boundary-tangential rms turbulent velocity, $u = (\overline{u_1'^2})^{1/2}$ was monotonically reduced by the presence of the wall. In contrast, at higher Reynolds number ($Re_T \approx 2000$) Thomas and Hancock (1977) reported a near-boundary increase in u relative to its free-stream value as a result of the boundary, that persisted as the flow travelled downstream.

Hunt and Graham (1978) used rapid distortion theory (RDT) to attempt to address the differences in observations made, by splitting the region of flow influenced by the boundary into two distinct layers; an inner viscous layer adjacent to the boundary and an outer inviscid layer above, denoted the 'source region'. Within the source region, RDT predicted that u was amplified and w was reduced. In contrast, in the inner viscous layer all components of the turbulent velocity were predicted to reduce monotonically to zero (Hunt and Graham, 1978). However, amplification of u in the source region was predicted under the assumption that the viscous effects were confined to the viscous sub-layer with small boundary-normal thickness when compared to the integral length scale of turbulence (*i.e.* at large Reynolds number), such that in the source layer viscous effects could be ignored over short times. This assumption implies that the theory is valid only for short times over which the turbulence does not decay significantly. In addition, nonlinear effects develop over long time periods, such as straining of small eddies by larger eddies near the boundary, leading to a breakdown of the assumptions made in the original RDT. As a consequence, it can be argued that the model is not valid at large times (Aronson et al., 1997; Perot and Moin, 1995a). Hunt (1984) proposed a nonlinear correction to the tangential turbulent velocities predicted by Hunt and Graham (1978) to account for the straining of small eddies near the boundary. The theory has been proposed to be valid, subject to the nonlinear correction, under the assumption that the mean rate of energy dissipation is approximately constant with height. In addition,

enstrophy budgets, estimating the vortical corrections to the original theory, further predict that in the limit of large Reynolds number the theory proposed by Hunt and Graham (1978) is applicable even at large times (Magnaudet, 2003).

Similar results to those proposed by Hunt and Graham (1978) and Hunt (1984) have been reported in experimental studies using oscillating-grid turbulence (OGT). In this case a horizontal grid within a cuboid tank is oscillated vertically at fixed frequency and amplitude. Under ideal conditions, the turbulence produced is statistically stationary, homogeneous and isotropic in planes parallel to the grid, with negligible mean flow (De Silva and Fernando, 1994). The turbulence is, however, inhomogeneous in planes normal to the grid; that is, the rms velocity components u and w decay with increasing distance normal to the grid. Hence, when interacting with a horizontal boundary, the boundary induced effects are superimposed onto pre-existing inhomogeneity in the boundary-normal direction. Measurements of OGT impinging upon a horizontal boundary made by McDougall (1979) exhibited a monotonic reduction of u at low Reynolds number ($Re \equiv u\ell/\nu \approx 40$; ℓ denotes integral length scale), while Hannoun et al. (1988) observed amplification of u at higher Reynolds number ($Re \approx 120$). Using OGT, measurements showing amplification of tangential turbulent velocities have also been observed at a sharp density interface between two fluids (Brumley and Jirka, 1987; Kit et al., 1997) and at a sediment boundary (Wan Mohtar and Munro, 2013).

The problem has also been studied using numerical simulation (Biringen and Reynolds, 1981; Perot and Moin, 1995a; Bodart et al., 2010). Perot and Moin (1995a) used direct numerical simulation (DNS) to study the instantaneous insertion of a boundary into a field of zero-mean, homogeneous, isotropic turbulence. They found that following boundary insertion a peak in u was observed that was rapidly dissipated for Re_T between 50 and 375. The cause of the initial peak in u was attributed to the process of rapid boundary insertion, where in order to preserve continuity, suddenly imposing the wall blocking condition ($w = 0$) resulted in pressure increases and redistribution of turbulent kinetic energy. The rapid dissipation of the peak in u was attributed to viscous damping. Similar results were also reported in the experimental study of Aronson et al. (1997) using a 'moving belt' configuration for Re_T between 325 and 425. Most recently Bodart et al. (2010) reported a DNS study of zero-mean-shear turbulence produced in a cubic domain by a random forcing field within a thin horizontal layer equidistant from two opposite, horizontal, boundaries of the cube. The turbulence decayed vertically across the region between the source layer and the boundary, in a manner comparable to OGT. Bodart et al. (2010) reported that u was monotonically reduced by the presence of the boundary, but that it attains an approximately constant value across a proportion of the boundary-affected region. (In this study, $Re_T = 100$ at the edge of the source layer.)

The structure of the turbulence in the boundary-affected region is thought to be the result of the interaction of a viscous and a kinematic response. The kinematic condition,

often referred to as wall blocking, was the focus of Hunt & Graham's RDT and is due to the 'blocking' of a fluid element as it travels towards a boundary. Hunt and Graham (1978) propose that this kinematic condition results in a net transfer of energy from w to u. Notably, this kinematic condition acts on w for distances approximately of order of the integral length scale of the turbulence, and so acts at a greater distance from the boundary than the viscous condition acts on all velocity components. This gives rise to the two-layer structure discussed—the viscous sub-layer and outer source layer.

In contrast, Perot and Moin (1995a) argue that the underlying physics is governed by the behaviour of a viscous response. Their discussion focused on an imbalance between 'splats' and 'antisplats'. A splat can be considered to be a conceptualised element of fluid that is blocked as it travels towards the boundary. Conversely a region of fluid moving away from the boundary may be referred to as an 'antisplat', which is produced by the collision of fluid elements travelling along the boundary (Chu and Falco, 1988). In an inviscid fluid, the blocking of a splat would result in fluid elements that move tangential to the boundary until an antisplat occurred without loss of turbulent kinetic energy, with little overall intercomponent energy transfer. However, in a viscous fluid, energy is dissipated as the fluid element travels along the boundary. This results in less energy input into the antisplat than that of the splat; referred to as 'splat-antisplat imbalance' (Perot and Moin, 1995a). This model suggests there is no significant net energy transfer from w to u, as energy is dissipated, resulting in no amplification of u, in contradiction to the kinematic process outlined in Hunt and Graham (1978).

The transport equations for the Reynolds stress tensor are key to understanding energy transfer in a turbulent flow (see Tennekes and Lumley, 1972, p. 63). For turbulence interacting with a boundary the pressure-strain term has been found to be critical, and represents intercomponent energy transfer. Previous analyses of the pressure-strain term have indicated that close to the wall energy is transferred from w^2 to u^2 such that there is increasing anisotropy (Perot and Moin, 1995a; Aronson et al., 1997; Bodart et al., 2010). However, it has been conjectured that it is unlikely for there to be sufficient intercomponent energy transfer to cause a peak in u due to the increased levels of diffusion and dissipation as the boundary is approached (Perot and Moin, 1995a; Aronson et al., 1997). In contrast, further from the wall (but within the source layer) the pressure-strain term has been reported to reverse sign (Perot and Moin, 1995a; Aronson et al., 1997; Bodart et al., 2010), indicating a transfer of energy from u^2 to w^2. Importantly, this energy transfer occurs in a region where $u > w$ (and where viscous effects are significantly reduced) and so has previously been described as a 'return-to-isotropy'. We stress that, here, 'return-to-isotropy' is used only to describe specifically this intercomponent energy transfer (from u^2 to w^2, where $u > w$) and does not encompass a temporal evolution in turbulent statistics towards isotropy. This effect has been argued to arise as a result of the blocking condition (Walker et al., 1996); as

the boundary is approached, and w is blocked, we observe an increasing anisotropy and it is this anisotropy that drives the energy transfer.

The results of Reynolds stress budgets reported by Bodart et al. (2010) also support the importance of the pressure-strain term. However, Bodart et al. (2010) suggest that energy transfer is not governed by viscous effects and stress anisotropy, but instead by the skewness of the velocity fluctuations normal to the boundary ($\overline{u_3' u_3' u_3'}/w^3$), giving rise to a net energy transfer from w^2 to u^2 in the boundary-affected region. Whilst the authors acknowledged the role of viscosity in acting to remove energy from the antisplat generation process they suggest that this effect is minor in the context of their flow that displays strong inhomogeneity in the boundary-normal direction. A link between energy transfer and skewness of the boundary-normal velocity component was also proposed in the RDT study by Magnaudet (2003). However, an underlying physical mechanism to explain how a far-field inhomogeneity gives rise to a transfer of energy from w^2 to u^2 in the boundary-affected region has not been proposed.

It has also been suggested that Reynolds number effects are significant in determining the statistical spatial structure of u and w (Hunt and Graham, 1978), although recent studies have not identified a clear dependence on Reynolds number (Aronson et al., 1997; Perot and Moin, 1995a). Furthermore, Perot and Moin (1995a) argue—in line with their proposal that viscous effects govern intercomponent energy transfer—that there is no significant Reynolds number dependency. However, the generally moderate range of Reynolds numbers (Re_T between 50 and 425) used in these studies limit their applicability at higher Reynolds numbers. Hence, it remains unclear what effect, if any, Reynolds number plays in the interaction of zero-mean-shear turbulence with a solid impermeable boundary.

In this paper we study the interaction between oscillating-grid turbulence and a solid, planar boundary positioned below the grid, aligned with its plane parallel to the grid. The turbulent flow produced is homogeneous in planes parallel to the grid, but inhomogeneous in the grid-normal direction, with mean-flow components that are small compared to the fluctuations. Section 2 describes the experimental set-up and the techniques used to measure the flow. In section 3 we present experimental results characterising the turbulence produced in regions away from the boundary and in section 4 describe how the rms turbulent velocity components are affected by the presence of the boundary. In section 5 we present results describing the turbulent kinetic energy (TKE) in the boundary-affected region, including for the vertical flux of TKE and terms of the transport equations for the Reynolds stress tensor, which provide evidence of the mechanisms governing the interaction. In section 6 we discuss these mechanisms in light of the previously published literature on the interaction of zero-mean-shear turbulence with a solid boundary. Conclusions are made in section 7.

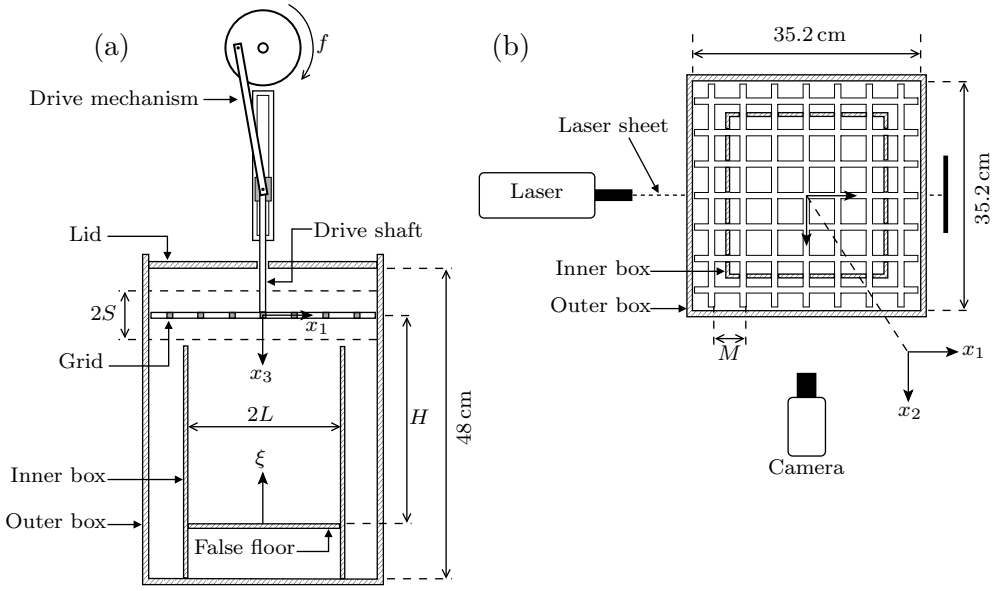


Figure 3.1: Sketches showing the key components of the experimental set-up. (a) A side view showing the positioning of the reciprocating drive mechanism, the horizontal grid, the false floor and the inner and outer boxes. (b) A plan view showing the position of the inner box relative to the grid's mesh, and the position of the camera relative to the vertical laser-sheet. Also shown are the coordinate directions (x_1, x_2, x_3), and the vertical height normal to the false floor, denoted $\xi = H - x_3$.

3.2 Experiments

A schematic view of the experimental set-up is shown in figure 3.1. The experiments were conducted in a transparent acrylic box with internal dimensions $35.2\,\mathrm{cm} \times 35.2\,\mathrm{cm} \times 50\,\mathrm{cm}$, henceforth denoted the 'outer box' (see figure 3.1). A rigid acrylic lid was suspended horizontally 2 cm below the top of the outer box, which was filled with a salt water solution of uniform density $\rho = 1.028\,\mathrm{g/cm^3}$ to the height of the lid's underside (*i.e.* the total water depth was 48 cm). The salt used was NaCl. The grid was attached to the base of a stainless steel drive shaft (of 1 cm diameter) and suspended inside the outer box with the plane of the grid horizontal (see figure 3.1a). The drive shaft passed through a circular hole of 2.6 cm diameter in the centre of the lid. The vertical oscillatory motion of the shaft and grid was driven by using a cam and linear bearing to convert the rotary motion of a motorised flywheel to reciprocating vertical motion of the drive shaft, as shown in figure 3.1(a). The frequency of the grid oscillation, f, was controlled by using a potentiometer to vary the current across the motor, and was varied between 1.6 Hz and 5.4 Hz. The stroke, S, defined as equal to the amplitude of the grid's motion, was varied by changing the radius of the flywheel; strokes of $S = 2.5\,\mathrm{cm}$ and 3.0 cm were used. These ranges for f and S are in line with those used in previous OGT studies (Hopfinger and Linden, 1982; Thompson and Turner, 1975; Hopfinger and Toly, 1976; McDougall, 1979; Wan Mohtar and Munro, 2013).

Two grids were used for this study, henceforth referred to as the coarse and fine grids. Both grids were of stainless steel construction, with a clearance of approximately 0.3 cm between the grid's perimeter and the internal side walls of the outer box. The coarse grid consisted of an array of 7×7 bars, with square cross-section of 1 cm width, and with mesh spacing $M = 5$ cm. Figure 3.1(b) shows a plan view of the coarse grid, and the corresponding mesh spacing (M). This grid type has been widely used in previous OGT studies (Thompson and Turner, 1975; Hopfinger and Toly, 1976; Hopfinger and Linden, 1982; Nokes, 1988). The fine grid consisted of a 9×9 array of bars, with square cross-section of 0.6 cm width, and mesh spacing $M = 3.8$ cm. The corresponding solidities were 36.4% and 28.7% for the coarse and fine grids respectively. The edge conditions of both grids were chosen such that tank side walls were planes of symmetry—this condition is known to help reduce the magnitude of secondary flows (De Silva and Fernando, 1994).

A small degree of secondary mean flow is inherent in OGT experiments. However, the installation of an open-ended 'inner box' has previously been shown to reduce the large-scale circulations that give rise to these secondary flows (Dickinson and Long, 1983; Hopfinger and Toly, 1976). This approach was adopted here. Two interchangeable inner boxes were used, one for each grid. Each open-ended inner box was fixed centrally on plan at the base of the tank so that the vertical walls were equidistant between the outermost and second-outermost bars of the grid, as shown in figure 3.1(b) (for the coarse grid). The grid was then positioned so that when at the bottom of its stoke it was 1 cm above the top of the inner box (see figure 3.1a). The inner boxes were constructed from 0.5 cm thick transparent acrylic with internal dimensions 24.5 cm $\times$ 24.5 cm $\times$ 26.5 cm (for the coarse grid) and 26.1 cm $\times$ 26.1 cm $\times$ 26.5 cm (for the fine grid). We will henceforth let $2L$ denote the internal width of the inner box, as shown in figure 3.1(a). Additional experiments (not reported here)* indicated that the inner box reduced, but did not eliminate, the large-scale circulations—a similar effect was reported in the studies by Dickinson and Long (1983) and Hopfinger and Toly (1976). We also stress that the asymmetrical positioning of the grid at the top of the domain did not have a significant effect on the mean flow.

A solid false-floor plate, spanning the interior of the inner tank, was inserted parallel to the grid and at a depth H below the grid's mean position (see figure 3.1a). It is known that OGT is anisotropic at distances less than $2.5M$ below the grid (Hopfinger and Toly, 1976). Hence, values of H ranging between $4M$ and $5.1M$ were used to ensure that the region where the turbulence was affected by the plate—henceforth referred to as the 'boundary-affected region'—did not extend into the near-grid, anisotropic region. A tight fit was ensured between the plate and the inner box by use of thin neoprene seals, set into the perimeter of the plate. As a result, the fluid flow between the edge of the plate and the inner tank was negligible.

i.e. The experiments reported in chapter 2.

Here we report results from a total of 31 experiments. Table 3.1 shows the values of H used for each combination of M, S and f considered (see caption for details). The grid Reynolds number (Re_G) is defined as

$$Re_G = MSf/\nu; \tag{3.1}$$

varying M, S and f as outlined in table 3.1, corresponded to Re_G between 1520 and 8100, which is a relatively broad range in comparison to previous studies using OGT. For example, previous studies of the interaction of OGT with a boundary used Re_G between 250 and 6660 (Brumley and Jirka, 1987; Hannoun et al., 1988; Kit et al., 1997; McDougall, 1979). Further increases in Re_G were not possible; proportionately more intense mean flows (in comparison to the magnitude of the fluctuations) are known to arise at higher grid oscillation frequency (McDougall, 1979), such that turbulence produced is a poor approximation to zero-mean-shear turbulence.

Measurements of instantaneous fluid velocities were obtained using two-dimensional particle imaging velocimetry (PIV), applied to the vertical plane through the centre of the grid, in the region inside the inner box spanned by the grid and the false floor. Small, neutrally buoyant tracer particles (Pliolite with diameter range 75 to 125 μm) were added to the water volume and thoroughly stirred. A thin light sheet was used to illuminate the particles located within the central, vertical plane. The light sheet was produced by a 100 Hz pulsed laser (Dantec Dynamics NANO L Power 50-100, Class 4). As the grid oscillated, the motion of the illuminated particles, as they were advected by the turbulent flow, was recorded using a high-speed digital camera positioned to point horizontally into the inner tank's interior, and aligned perpendicular to the plane of the vertical light sheet (see figure 3.1b). The camera's capture was synchronised with the pulse of the laser, so the images were recorded at 100 frames per second (at 1280×1024 pixel resolution). PIV calculations were performed in Digiflow (Dalziel, 2006), using square interrogation windows of 13×13 pixels, overlapped to achieve 8 pixel spacing between velocity vectors. This resulted in a physical spacing between velocity vectors of approximately 0.2 cm. Measurements were made only after the grid had been oscillating (at a fixed frequency and stroke) for 15 min to ensure turbulence was fully established. OGT is statistically stationary and so the statistical properties of the flow were analysed using time averages. Hence, in each experiment velocity data were captured for a period of 4 min; analysis of the data showed that the time-averaged mean and rms velocity components were well converged over this period.

The velocity data were calculated and analysed relative to the right-handed coordinate system (x_1, x_2, x_3); here, x_3 denotes vertical depth below the mid-height of the grid's oscillation, and (x_1, x_2) are the horizontal coordinates relative to the centre of the grid (see figure 3.1). The corresponding velocity components are denoted (u_1, u_2, u_3); the two components measured using the PIV set-up described above are $u_1(x_1, x_3, t)$ and $u_3(x_1, x_3, t)$, in the central plane at $x_2 = 0$. We use the conventional Reynolds

M	S	f (Hz)											
(cm)	(cm)	*1.6*	*2.2*	*2.4*	*2.6*	*3.1*	*3.4*	*3.5*	*3.8*	*4.3*	*4.6*	*5.4*
3.8	*2.5*	$4.1M$	-	$4.1M^{\ddagger_1}$, $4.9M^{\ddagger_1}$	-	-	-	$4.1M$	-	-	-	-
3.8	*3.0*	-	-	-	-	$4.3M$	-	$4.3M$, $5.1M$	-	$4.2M$	-	$4.3M^{\dagger_4\ddagger_2}$
5.0	*2.5*	$4.1M^{\dagger_5\ddagger_3}$	$4.2M$, $4.9M$	-	$4.1M$, $4.9M$	-	$4.1M^{\dagger_4\ddagger_4}$	-	$4.2M$, $4.9M$	-	-	-
5.0	*3.0*	-	-	-	-	-	-	$4.2M$, $5.0M$	-	-	$4.2M$, $5.1M$	$4.3M$

Table 3.1: A summary of the experimental conditions considered. Each entry shows the value of H (relative to the mesh size, M) used for the various combinations of M, S and f considered. Three of the experiments listed were repeated either $n = 4$ or 5 times, which are indicated by the $\dagger_n$ superscript. In total 31 experiments were performed. A representative subset of the experiments are used in subsequent sections (to avoid an over saturation of points when plotting data), which we have indicated using the $\ddagger_1$, $\ddagger_2$, $\ddagger_3$, $\ddagger_4$ superscripts; these four experimental conditions correspond to Reynolds numbers of $Re_G = 2308$,6155, 2024 and 4218, respectively.

decomposition $u_i = U_i + u_i'$, where $u_i'(\mathbf{x}, t)$ denote the fluctuating components and $U_i(\mathbf{x}) = \overline{u_i}$ the time-averaged mean components (the overbar notation is used throughout to denote time averaging). In the calculation of second-order quantities, the raw measured values of u_1 and u_3 were used; we note that calculations of power spectra from time series at various points within the flow did not indicate the presence of harmonic-like signatures due to grid forcing in the measured velocity components. We also introduce the coordinate $\xi = H - x_3$, which denotes vertical height above the false floor (see figure 3.1a). This coordinate is used only for convenience when plotting and comparing data; we stress that all velocities (and derivatives of velocities) were calculated in terms of the right-handed coordinates (x_1, x_2, x_3).

OGT has been used in numerous experimental studies and consistently found to produce turbulence with mean-flow components that are small compared to the fluctuations (McDougall, 1979; Hopfinger and Linden, 1982; Xuequan and Hopfinger, 1986; Brumley and Jirka, 1987; Fernando and De Silva, 1993). For a grid consisting of square bars, the turbulence produced is well described by the standard model

$$u = C_1 S f \left(\frac{x_3}{M^{1/2} S^{1/2}} \right)^{-\gamma}, \tag{3.2a}$$

$$w = C_2 u, \tag{3.2b}$$

$$\overline{\ell} = C_3 x_3, \tag{3.2c}$$

$$\overline{u_1' u_2'} \approx \overline{u_1' u_3'} \approx 0, \tag{3.2d}$$

with $\gamma \approx 1$. In the above $u \equiv (\overline{u_1'^2})^{1/2}$, $v \equiv (\overline{u_2'^2})^{1/2}$, $w \equiv (\overline{u_3'^2})^{1/2}$, which are henceforth used to denote time-averaged rms velocity components. Symmetry means that $u \approx v$ is assumed. We stress that the model is only valid for $x_3 \gtrsim 2.5M$. Previous studies have shown that the coefficients γ, C_1, C_2 and C_3 are sensitive to the experimental configuration used, with values typically reported to be $\gamma = 0.8$ to 1.5, $C_1 = 0.2$ to 0.5, $C_2 = 1.1$ to 1.4 and $C_3 = 0.1$ to 0.25 (Thompson and Turner, 1975; Hopfinger and Toly, 1976; McDougall, 1979; Hopfinger and Linden, 1982; De Silva and Fernando, 1994; Kit et al., 1997; Nokes, 1988; Atkinson et al., 1987). The validity of equations (3.2) depends on a number of additional conditions (Fernando and De Silva, 1993): the grid solidity should be less than 40%; the grid oscillation frequency should be less than 7 Hz; the grid should be designed to ensure that tank wall's act as a plane of symmetry. All of these conditions are satisfied with the current apparatus. Data from preliminary testing of the apparatus (for Re_G between 2050 and 8100), in the absence of the false-floor plate, indicated good agreement with the standard OGT model (equation 3.2). The spatial structure of OGT of this type is well established and so we omit the presentation of these data here, and instead refer the reader to previous studies for illustrations (see for example Thompson and Turner, 1975; Hopfinger and Toly, 1976; Kit et al., 1997).

3.3 Turbulence measurements within the bulk interior region

We now describe the turbulence measurements obtained from experiments with the false floor installed. Recall, the floor plate was positioned horizontally at a depth H (between $4M$ and $5.1M$) below the grid's mean position (see figure 3.1a). We show in section 3.4 that the boundary induced effects are mostly confined to a layer of height δ_s above the plate, wherein the turbulence is affected by the kinematic blocking condition. At this stage we loosely note that δ_s is of the order of the integral length scale of the turbulence; we define this relationship more closely in section 3.4.2. To begin, however, we first describe the spatial structure of the turbulence within the 'bulk interior' of the flow, corresponding to the region above the boundary-affected layer (*i.e.* $\xi \geqslant \delta_s$) and below the near-grid, anisotropic region (*i.e.* $x_3 \geqslant 2.5M$).

We note that, previous measurements of OGT have shown a dependence on the grid geometry (De Silva and Fernando, 1994), characterised by grid mesh size M. Slight differences in the turbulence statistics are also observed in the experiments reported here, using mesh sizes $M = 3.8\,\text{cm}$ and $5.0\,\text{cm}$. Hence, where differences in turbulent statistics were evident between the two grids used, the results have been identified separately.

3.3.1 Side wall effects

OGT is typically reported to be homogeneous and isotropic in planes parallel to the grid. However, the effect the tank side walls have on the turbulence is not well understood. To assess this effect we consider the degree of isotropy, $\langle w/u \rangle_3$, across the horizontal width of the tank, spatially averaged over the vertical direction (between $\xi \geqslant \delta_s$ and $x_3 \geqslant 2.5M$), where $\langle \cdot \rangle_3$ is henceforth used to denote the vertical average over this range. The results obtained are shown in figure 3.2(a), plotted against the horizontal coordinate x_1, which has been scaled by the half-width of the inner box (L). We stress that the data shown in figure 3.2(a) are representative of measurements at all depths x_3 within the bulk interior region and that the spatial averaging, $\langle \cdot \rangle_3$, has been used here only to reduce minor scatter. The data indicate a slight dependency on the grid used and so have been shown separately—the solid lines correspond to data obtained using the fine grid, the broken lines to data using the coarse grid (see legend). To avoid over saturation, the data in figure 3.2(a) are profiles obtained by averaging the results from all the experiments performed for each grid type (12 experiments for the fine grid and 19 experiments for the coarse grid), over the range of f and S considered.

To further assess this effect, we also considered the magnitude of the individual rms velocity components across the horizontal width of the tank. That is, the measured rms velocity fields $u(x_1, x_3)$ and $w(x_1, x_3)$ were normalised by the corresponding profiles spatially averaged across the horizontal x_1-direction, here denoted by $\langle u \rangle_1(x_3)$ and

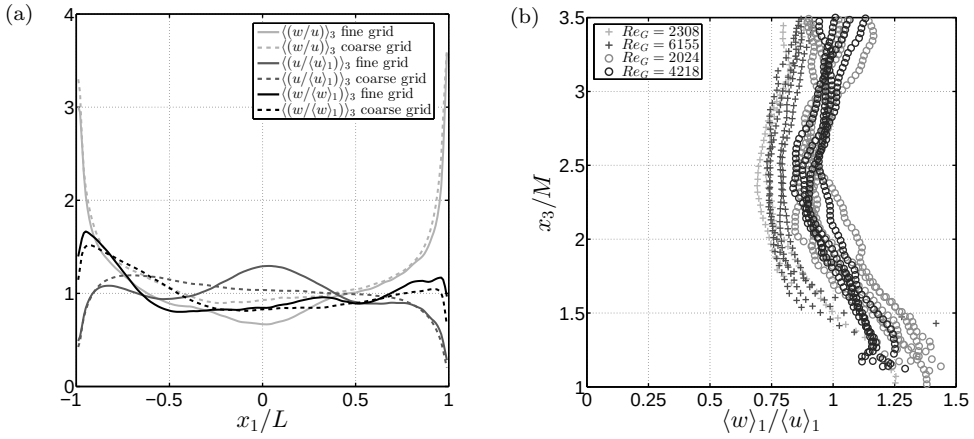


Figure 3.2: (a) Normalised profiles $\langle u/\langle u\rangle_1\rangle_3$, $\langle w/\langle w\rangle_1\rangle_3$ (homogeneity) and the isotropy parameter $\langle w/u\rangle_3$, each spatially averaged in x_3 and plotted against the horizontal x_1 coordinate, which has been scaled by the half-width of the inner box, L. Data obtained using the fine and coarse grids are shown separately (see legend). (b) Measurements of the isotropy parameter $\langle w\rangle_1/\langle u\rangle_1$ plotted against x_3/M (which, recall, have been spatially averaged across the central 50% of the inner box's width). The data shown are from the representative subset of experiments (indicated by the ‡ superscripts in table 3.1) for $Re_G = 2024$, 2308, 4218 and 6155 (see legend). For each Re_G, data from the n repeats are shown, where $n = 2$, 4 or 5 (see table 3.1). The data obtained using the coarse and fine grids are shown separately, indicated by the circles and crosses respectively.

$\langle w\rangle_1(x_3)$. A feature of this normalisation is to remove the effects of velocity decay in the x_3-direction. The normalised fields were then spatially averaged in the x_3-direction (i.e. $\langle(u/\langle u\rangle_1)\rangle_3$ and $\langle(w/\langle w\rangle_1)\rangle_3$) to reduce minor scatter. The normalised rms velocity components are also shown in 3.2(a), also averaged over all experiments (by grid type).

Figure 3.2(a) shows that the tank side walls have a significant effect, rendering the turbulence anisotropic in regions close to the walls. However, across the central 50% of the tank's width, the data indicate that the turbulence is approximately isotropic and homogeneous. Hence, throughout the remainder of this paper our attention is focused on this central region and the side wall (anisotropic) regions are ignored in the calculation of turbulent statistics, so that all spatial averaging in the x_1-direction (denoted $\langle\cdot\rangle_1$) is henceforth taken over the central 50% region, only. In contrast to the current results, McDougall (1979) reported significant variations in turbulent velocities across a horizontal plane, even far from the side walls. However, the measurements of McDougall (1979) were taken at $x_3 = 2M$, in a region in which jets produced by the action of the oscillating grid are known to have not fully broken down (Hopfinger and Toly, 1976; Atkinson et al., 1987). To our knowledge, the presence of anisotropic side wall regions has not previously been reported in studies of OGT.

3.3.2 Degree of isotropy

The horizontally averaged isotropy parameter, $\langle w\rangle_1/\langle u\rangle_1$, is shown in figure 3.2(b), plotted against x_3/M, and is approximately constant and close to 1 within the bulk interior region ($\xi \geqslant \delta_s$, $x_3 \geqslant 2.5M$). There is a slight dependency on grid type, and so the data obtained using the fine and coarse grids are shown separately (see figure caption). For the coarse grid, $\langle w\rangle_1/\langle u\rangle_1 \approx 1$, however for the fine grid, $\langle w\rangle_1/\langle u\rangle_1 < 1$ and slowly tends to 1 as x_3 increases. The data do not show any clear dependence on Reynolds number, Re_G. We note that the magnitude of these data are slightly lower than in the literature (for example, $\langle w\rangle_1/\langle u\rangle_1 \approx 1.1 - 1.4$ in Hopfinger and Linden, 1982; Kit et al., 1997; Hopfinger and Toly, 1976; De Silva and Fernando, 1994). This is most likely a result of excluding the anisotropic side wall regions in the current results, where the ratio w/u is significantly larger (see figure 3.2a).

3.3.3 Spatial decay of the rms velocity components

A defining aspect of OGT is the decrease in magnitude of the rms velocity components with increasing depth below the grid. In section 3.2 we noted that in the absence of the floor plate the measured rms velocity components are well described by the standard model (3.2). With the plate inserted, the measurements of u and w exhibited a similar spatial decay away from the grid and so again we sought to fit to the data power laws of the form

$$u = C_u S f \left(\frac{x_3}{M^{1/2}S^{1/2}}\right)^{-\gamma_u}, \tag{3.3a}$$

$$w = C_w S f \left(\frac{x_3}{M^{1/2}S^{1/2}}\right)^{-\gamma_w}, \tag{3.3b}$$

in the bulk interior region $\xi \geqslant \delta_s$, $x_3 \geqslant 2.5M$. For each experiment a single value of each of the coefficients C_u, C_w and exponents γ_u, γ_w were obtained using a regression best fit. Figure 3.3(a) shows typical examples of the regressions fits applied to measurements of the rms velocity component u; the results are shown for four separate experiments, but performed under nominally identical conditions with $Re_G = 4218$. The goodness of fit and degree of scatter evident for these data are representative of all the experiments. A similar goodness of fit (and scatter) were found for the vertical rms velocity component (w). The fitted values of γ_u and γ_w, for each of the 31 experiments, are shown in figure 3.3(b), plotted against corresponding Reynolds number Re_G. Figure 3.3(b) indicates that the fitted decay exponents exhibit significant departure in magnitude relative to the idealised model ($\gamma_u = \gamma_w = 1$), with no apparent dependence on Re_G; this effect is most notable for the vertical rms velocity component, and when the fine grid was used. Moreover, the data in figure 3.3(b) show that repeating experiments under nominally identical conditions can result in variations in the resulting decay exponent. This is not unexpected; for example, McKenna and McGillis (2004) showed that the magnitude of

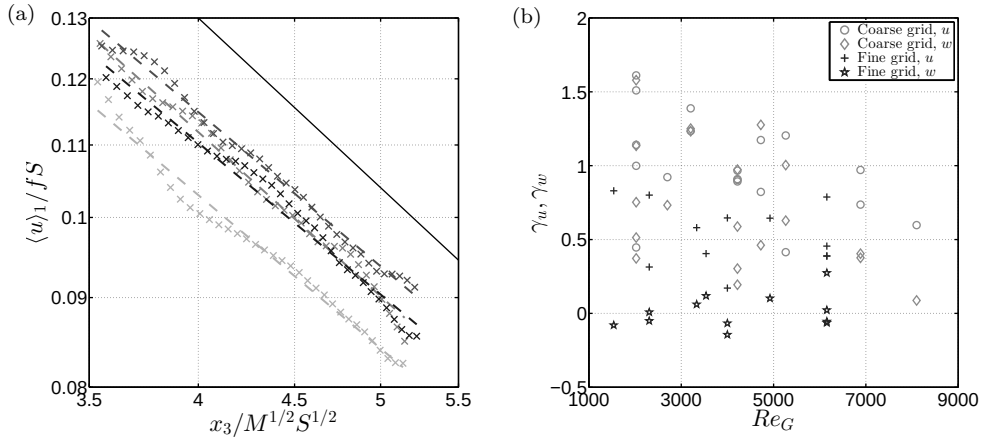


Figure 3.3: Plots showing the results of fitting the decay laws in equation (3.3) to the experimental data. (a) Measurements of u (crosses) compared with the corresponding regression best fit of equation (3.3a) (broken lines). The results are shown from four separate experiments, but each performed under nominally identical conditions with $Re_G = 4218$. The fits were performed in the bulk interior region (with $x_3 > 2.5M$ and $\xi > \delta_s$). For comparison, a decay exponent equal to 1 is also shown, by the solid line. (b) The fitted exponents γ_u, γ_w from each of the 31 experiments, plotted against grid Reynolds number Re_G.

turbulent fluctuations may vary by as much as 15% from separate experiments performed under the same conditions.

3.3.4 Mean flow

The mean flow is an integral aspect of OGT and, as noted in section 3.2, the presence of the inner box reduced but did not eliminate the large circulations that give rise to the mean flow. The mean flow within OGT has been studied in detail in numerous previous studies (see for example De Silva and Fernando, 1994; McKenna and McGillis, 2004; McDougall, 1979; Dohan and Sutherland, 2002), and the qualitative characteristics of the mean flow observed with our apparatus are little different to those reported in these studies. In particular, the mean flow is not symmetrical, being most intense close to the grid (and tank walls) and decaying with distance below the grid. Plots showing typical mean-flow fields observed in OGT can be found, for example, in McKenna and McGillis (2004)*.

The effect the presence of the floor plate had on the magnitude of the secondary flow was assessed using the inverse turbulence intensities $\langle |U_1|/u \rangle_1$ and $\langle |U_3|/w \rangle_1$ (as previously used by Variano and Cowen, 2008), which are shown in figure 3.4 plotted against scaled height ξ/δ_s above the plate. Recall that δ_s denotes a thin layer adjacent to the plate within which the boundary induced effects, on the turbulence statistics, are mostly confined. As the plate surface at $\xi = 0$ is approached, the vertical intensity

*Recall that typical mean-flow fields observed within the current apparatus are shown in chapter 2.

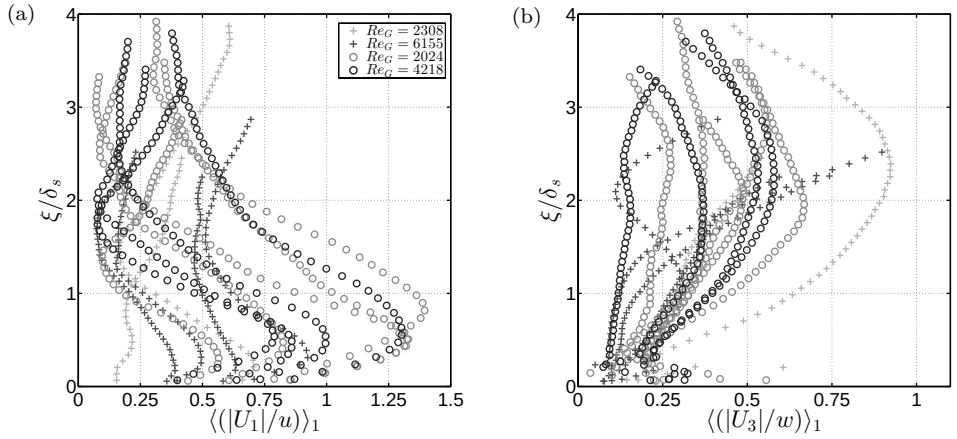


Figure 3.4: Plots showing the inverse turbulence intensities $\langle|U_1|/u\rangle_1$ and $\langle|U_3|/w\rangle_1$ plotted against height above the plate ξ, which has been scaled by the δ_s, the thickness of the boundary-affected region. The data shown are from the representative subset of experiments (indicated by the ‡ superscripts in table 3.1) for $Re_G = 2024$, 2308, 4218 and 6155 [see legend in (a)]. For each Re_G, data from the n repeats are shown, where $n = 2$, 4 or 5 (see table 3.1).

$\langle|U_3|/w\rangle_1$ is reduced towards zero, whereas the horizontal intensity $\langle|U_1|/u\rangle_1$ typically exhibits an increase to a peak value, before reducing at the boundary. Note that figure 3.4 indicates that the measured intensities $\langle|U_1|/u\rangle_1$ and $\langle|U_3|/w\rangle_1$ show no apparent dependence on Re_G, over the range of Re_G considered. Most importantly, figure 3.4 shows that in general the turbulence is of comparable or greater magnitude than mean flow components. Although the results indicate the presence of mean shear—such that the turbulence is not strictly zero-mean shear—the levels are sufficiently small in magnitude to allow meaningful comparisons to be made with previous studies based on zero-mean-shear conditions. The small levels of mean shear do result in production of TKE, although we will show in section 3.5.2 that the level of production is small.

3.4 Turbulence measurements in the boundary-affected region

We now focus attention on describing the turbulence characteristics (integral length scale and rms velocity components) in the boundary-affected region and compare our results to those available within the literature. The mechanisms that give rise to these results are explored in the subsequent sections.

3.4.1 Integral length scales

Estimates for integral length scales were obtained from the velocity measurements by computation of autocorrelation coefficients. We followed the approach used previously by Kit et al. (1997) by defining the integral length scale as the integral of the autocorrelation

function of $u_1'(x_1, x_3, t)$, over the spatial lag up to which the autocorrelation function first crosses zero. The autocorrelation function, at spatial lag χ, is defined as

$$r_u(x_3, t; \chi) = \frac{c_u(x_3, t; \chi)}{c_u(x_3, t; \chi = 0)}, \tag{3.4a}$$

where

$$c_u(x_3, t; \chi) = \frac{1}{L} \int_{-L/2}^{L/2} u_1'(x_1, x_3, t)\, u_1'(x_1 + \chi, x_3, t)\, \mathrm{d}x_1. \tag{3.4b}$$

Recall, L denotes the half-width of the inner box. The time-averaged integral length scale is then given by

$$\overline{\ell}\,(x_3) = \frac{1}{T} \int_0^T \int_0^{\chi_0} r_u(x_3, t; \chi)\, \mathrm{d}\chi\, \mathrm{d}t \tag{3.5}$$

where χ_0 denotes the spatial lag at which the autocorrelation function first becomes zero and T is the sampling period (which, recall, here was 4 min).

In previous studies of the interaction of zero-mean-shear turbulence with a boundary, a reference length scale ℓ_0 has been used (Hunt and Graham, 1978; Perot and Moin, 1995a). In these studies the turbulence beyond a boundary-affected region is homogeneous with a corresponding constant value of integral length scale, and so naturally this far-field integral length scale was used for ℓ_0. The situation is potentially more complex for OGT, as the integral length scale $\overline{\ell}$ is expected to depend on x_3 in the far field. Figure 3.5(a) shows the computed values of $\overline{\ell}$ obtained from the current data, which are plotted against height, ξ, above the plate. Beyond the boundary-affected region, for $\xi > 3$ cm, the data for $\overline{\ell}$ are relatively constant, taking values between 2 cm and 2.5 cm, but exhibit a significant degree of scatter. The data at heights $\xi < 3$ cm, increase slightly, before rapidly reducing at $\xi \approx 0.75$ cm. The level of scatter in the data made it difficult to identify a trend for $\xi > 3$ cm. Hence, the approach taken here was to define the reference integral length scale ℓ_0 to be the peak value attained by $\overline{\ell}$ (in the near-boundary region). This length scale remains physically intuitive; at this distance from the boundary the maximum integral eddy size first feels the effect of the wall. No link between the magnitude of ℓ_0 (or $\overline{\ell}$) and Reynolds number Re_G was observed.

We can more clearly consider the effect of the boundary on the integral length scales by considering the data shown in figure 3.5(b), of $\overline{\ell}/\ell_0$ plotted against scaled height ξ/ℓ_0. For $\xi < \ell_0$ integral length scales increase to a maximum, before reducing rapidly as the boundary is approached. However, the level of increase in $\overline{\ell}/\ell_0$ varies significantly between experiments and appears slightly larger for the fine grid than the coarse grid and so the data obtained using the coarse and fine grids are shown separately (see figure caption for details). A slight increase in $\overline{\ell}$ was also reported in the results of Thomas and Hancock (1977), and these data are also shown in Figure 3.5(b) (see legend).

Figure 3.6(a) shows corresponding measurements of the time-averaged transverse integral length scale, $\overline{\ell}_w$, which were obtained using equation (3.5), with r_w used in place

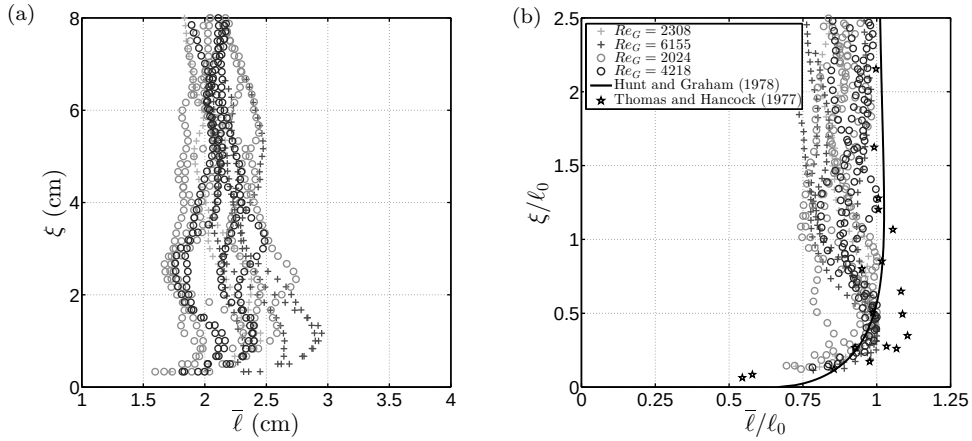


Figure 3.5: (a) Computed values of the time-averaged integral length scale, $\overline{\ell}$, plotted against height ξ. (b) The same data but scaled by the reference integral length scale, ℓ_0, from each experiment. The data obtained using the coarse and fine grids are shown separately, indicated by the circles and crosses, respectively. The data shown are from the representative subset of experiments (indicated by the ‡ superscripts in table 3.1) for $Re_G = 2024$, 2308, 4218 and 6155 [see legend in (b)]. For each Re_G, data from the n repeats are shown, where $n = 2$, 4 or 5 (see table 3.1). Also shown in (b) are corresponding experimental data from Thomas and Hancock (1977) and a prediction based on RDT by Hunt and Graham (1978) (see legend).

of r_u, which is defined using equation (3.4) with u_3' in place of u_1'. In figure 3.6(a), $\overline{\ell}_w$ is scaled by $\overline{\ell}$ and plotted against ξ/ℓ_0, and shows that the far-field value of $\overline{\ell}_w$ is indicative of quasi-isotropic turbulence; recall that for isotropic turbulence $\overline{\ell}_w/\overline{\ell} = 0.5$ (Pope, 2000). $\overline{\ell}_w$ deviates from its far-field value at $\xi \approx \ell_0$, initially appearing to reduce to zero at the boundary in line with the prediction of inviscid RDT analysis of Hunt and Graham (1978) and in approximate agreement with the results of Thomas and Hancock (1977) and Kit et al. (1997) which are also shown in figure 3.6 (see legend). This reduction is expected at a solid boundary; at a distance $\xi < \ell_0$ from the boundary, eddies of size greater than ξ will have been blocked, such that remaining eddies are of wavenumber $k_w > \xi^{-1}$. Note that the rapid reduction in $\overline{\ell}_w$ within the boundary-affected region as a result of the blocking condition renders the integral length scales anisotropic. In addition, figures 3.5 and 3.6(a) indicate that both $\overline{\ell}/\ell_0$ and $\overline{\ell}_w/\overline{\ell}$ are independent of Reynolds number, over the Reynolds number range considered.

3.4.2 Root-mean-square velocity data

Measured values of the degree of isotropy are shown in figure 3.6(b), plotted against scaled height ξ/ℓ_0. We note there is no apparent dependence on Reynolds number, Re_G, but there is a slight dependence on the grid type used, and so the data obtained using coarse and fine grids are shown separately (see figure caption for details). These data can be used as an indicator of the thickness of the boundary-affected region by noting the point at which values deviate from those in the far field. Figure 3.6(b) shows a rapid increase

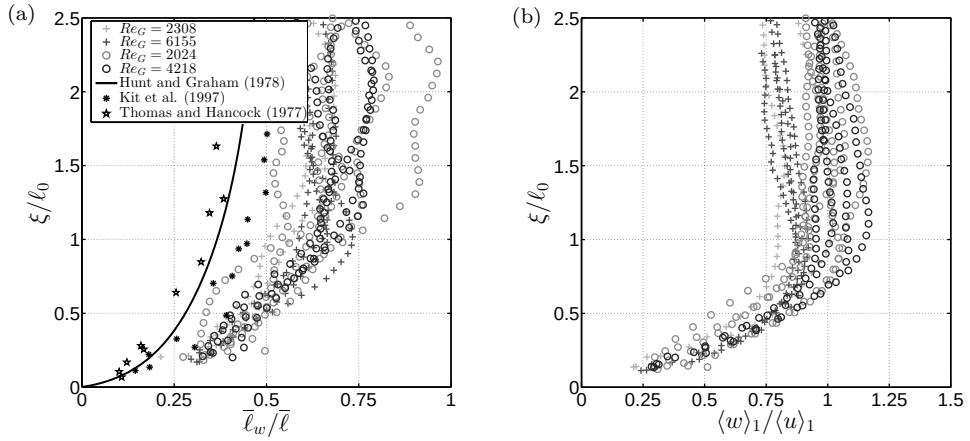


Figure 3.6: (a) Computed values of the time-averaged transverse integral length scale, $\overline{\ell}_w$, scaled by $\overline{\ell}$ and plotted against scaled height ξ/ℓ_0. Also shown are corresponding experimental data from Thomas and Hancock (1977) and Kit et al. (1997), and a prediction based on RDT by Hunt and Graham (1978) (see legend). (b) Measurements of the degree of isotropy $\langle w\rangle_1/\langle u\rangle_1$, plotted against normalised height ξ/ℓ_0. The data obtained using the coarse and fine grids are shown separately, indicated by the circles and crosses, respectively. In both plots the data shown are from the representative subset of experiments (indicated by the ‡ superscripts in table 3.1) for $Re_G = 2024$, 2308, 4218 and 6155 [see legend in (a)]. For each Re_G, data from the n repeats are shown, where $n = 2$, 4 or 5 (see table 3.1).

in anisotropy occurs at $\xi/\ell_0 \approx 1$, departing from the far-field trend. This is in accordance with the results of the integral length scales shown in figures 3.5 and 3.6(a). We therefore conclude that the boundary-affected region extends up to $\xi/\ell_0 \approx 1$, and henceforth throughout the remainder of this paper assume that the boundary-affected region has thickness $\delta_s = \ell_0$. We also note that the grid Reynolds number is approximately linearly proportional to the turbulent Reynolds number $Re \equiv u\overline{\ell}/\nu$ evaluated at a given distance below the grid; at the edge of the boundary-affected region $\xi = \delta_s$ we obtain values of turbulent Reynolds number between 35 and 485.

In order to consider the effect of the boundary on the rms velocity components for $\xi < \delta_s$ (recalling that for $\xi > \delta_s$, u and w decay with increasing x_3), we normalise results by corresponding values we would expect in the absence of the boundary. The expected values were determined from best fits of the power laws in equation (3.3), denoted by u_0 and w_0, applied to the measurements of $\langle u\rangle_1$ and $\langle w\rangle_1$ in the region above the boundary-affected layer, $\xi > \delta_s$ (shown in figure 3.3a). This method of normalisation is similar to that used by Hannoun et al. (1988) and Kit et al. (1997), who normalise data by local values measured in corresponding experiments conducted in the absence of a boundary.

Figures 3.7(a) and 3.7(b) show measurements of the normalised rms velocity components $\langle w\rangle_1/w_0$ and $\langle u\rangle_1/u_0$, plotted against scaled height ξ/ℓ_0. For the boundary-normal component (w), shown in figure 3.7(a), we observe a monotonic reduction of the nor-

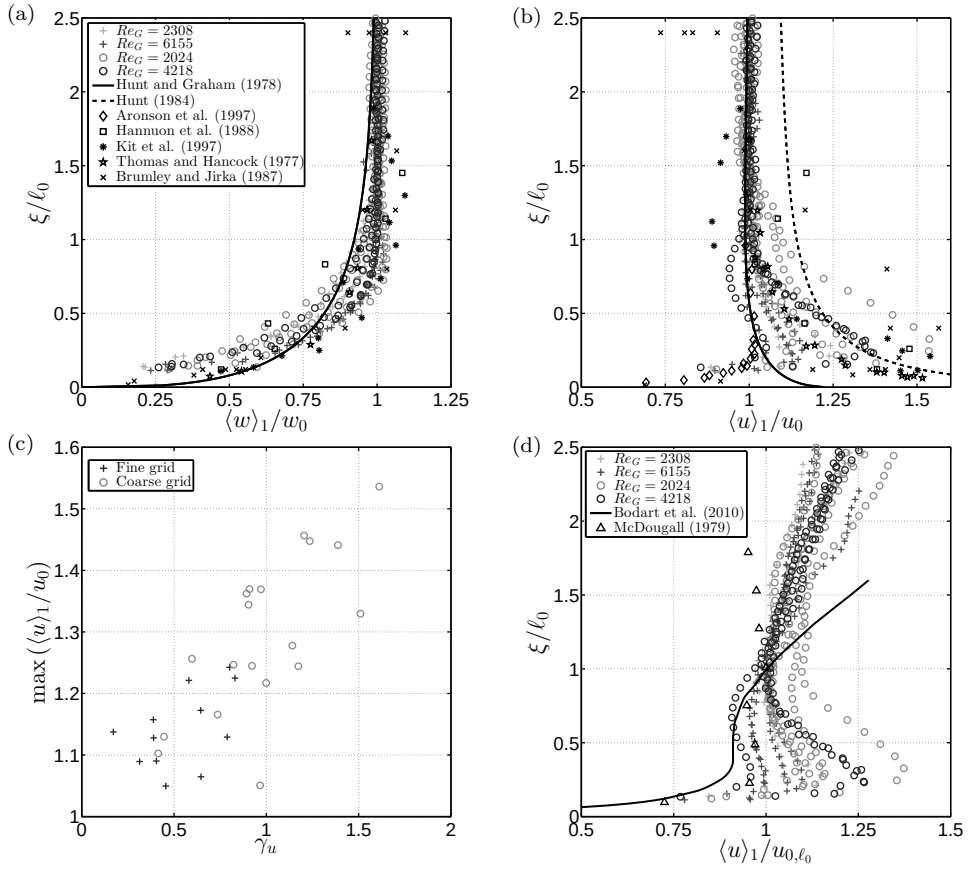


Figure 3.7: (a,b) Plots showing the scaled rms velocity components $\langle w\rangle_1/w_0$ and $\langle u\rangle_1/u_0$, plotted against scaled height ξ/ℓ_0. The data shown are from the representative subset of experiments (indicated by the ‡ superscripts in table 3.1) for $Re_G = 2024$, 2308, 4218 and 6155 [see legend in (a), which applies to both plots]. For each Re_G, data from the n repeats are shown, where $n = 2$, 4 or 5 (see table 3.1). Also shown are corresponding experimental data (Aronson et al., 1997; Hannoun et al., 1988; Kit et al., 1997; Thomas and Hancock, 1977; Brumley and Jirka, 1987) and predictions based on RDT (Hunt and Graham, 1978; Hunt, 1984) (see legend). (c) Plot showing $\max(\langle u\rangle_1/u_0)$ for each experiment, plotted against decay exponent γ_u (from equation 3.3a). Data are shown for all 31 experiments, with the data obtained using the coarse and fine grids shown separately [see legend]. (d) Measurements of the rms velocity component $\langle u\rangle_1$, plotted against scaled height ξ/ℓ_0. In this case, $\langle u\rangle_1$ has been normalised by the value of u_0 evaluated at $\xi = \ell_0$, denoted u_{0,ℓ_0}. The data shown are from the representative subset of experiments, with $Re_G = 2024$, 2308, 4218 and 6155 (see legend). Also shown are corresponding experimental data from McDougall (1979) and results of simulations by Bodart et al. (2010) (see legend).

malised velocity as the boundary is approached, which is independent of Reynolds number. Quantitative agreement is obtained with a range of studies (see legend) investigating the interaction of zero-mean-shear turbulence (Hunt and Graham, 1978; Hannoun et al., 1988; Kit et al., 1997; Thomas and Hancock, 1977; Brumley and Jirka, 1987). We stress that these previous studies cover a range of boundary types (density interface, free surface and solid boundary) and are for turbulence that is homogeneous beyond the

boundary-affected region, as well as for spatially decaying turbulence.

In contrast, measurements of the boundary-tangential component (u), shown in Figure 3.7(b), exhibit a greater level of scatter and provide a lesser degree of quantitative agreement with previous studies. In the current results values of u were amplified within the boundary-affected region, attaining a maximum at $\xi/\ell_0 \approx 0.25$ before rapidly reducing as $\xi \to 0$. Results show qualitative agreement with a range of studies utilising turbulence that spatially decays in the x_3 direction (Hannoun et al., 1988; Kit et al., 1997; Brumley and Jirka, 1987). In contrast, although the RDT proposed by Hunt and Graham (1978) predicts amplification of the velocity component outside the viscous sub-layer, RDT under-predicts the amplification observed. The modified RDT proposed by Hunt (1984) provides a better approximation of the amplification observed for the coarse grid. Poor agreement is obtained with the study of Aronson et al. (1997). However, the results of Aronson et al. (1997) and Thomas and Hancock (1977) were obtained from studies in which turbulence was homogeneous beyond the boundary-affected region. The results of Thomas and Hancock (1977) display features similar to the current results, however, we note their results have been questioned in light of frictional heating of the apparatus (Aronson et al., 1997).

We stress that the amplification of $\langle u \rangle_1/u_0$ does not exhibit a clear dependence on Reynolds number, instead figure 3.7(c) shows that the maximum amplification of $\langle u \rangle_1/u_0$ is weakly correlated with the decay rate of the velocity component γ_u, which may mask any Reynolds number effects, over the fairly narrow range of Reynolds number considered here. This is an important point and goes some way to address the disparity in results previously reported in the literature. Specifically, the previous studies that have identified $u/u_0 \leqslant 1$ are for the case where the far-field turbulence is homogeneous (Aronson et al., 1997; Perot and Moin, 1995a), which correspond to the case $\gamma_u = \gamma_w = 0$. In contrast, a number of studies that have predicted $u/u_0 > 1$ for $\xi < \delta_s$ are for the case of inhomogeneous far-field turbulence, with $\gamma_u, \gamma_w \neq 0$ (Hannoun et al., 1988; Kit et al., 1997; Brumley and Jirka, 1987). As such, these data suggest that the trend of u/u_0 for $\xi < \delta_s$ depends crucially on the nature of the turbulence itself (homogeneous versus inhomogeneous); this effect is considered further in section 3.5. Note that there is a clear grid dependence in the data shown in figure 3.7(c), which can be understood by noting that the rate of spatial decay of rms velocity was lower in experiments using the fine grid than the coarse grid (see section 3.3.3 and figure 3.3b).

In addition to the data normalisation described above using u_0 and w_0, it is also informative to consider the measurements of $\langle u \rangle_1$ scaled by the characteristic value of u_0 at the edge of the boundary-affected region, at $\xi = \ell_0$, henceforth denoted u_{0,ℓ_0}. Figure 3.7(d) shows the measurements of $\langle u \rangle_1$ scaled by u_{0,ℓ_0}, which indicate that, on average, $\langle u \rangle_1/u_{0,\ell_0} \gtrsim 1$ in the region for $\xi < \ell_0$, before rapidly reducing as the boundary is approached. Bodart et al. (2010) also presented results using this method of

normalisation that showed u in the boundary-affected region increasing from the far-field trend and attaining an approximately constant value, before reducing rapidly to zero as the boundary is approached. In plotting the results of Bodart et al. (2010)—shown by the solid line in figure 3.7(d)— we have assumed that the thickness of the boundary-affected region is $\delta_s \approx \ell_0 \approx 0.36 l_f$ (based on their figure 3b), where l_f denotes the characteristic length scale used by Bodart et al. (2010). Constant values of u in the boundary-affected region were also obtained in the results of McDougall (1979), which are also shown in figure 3.7(d) (see legend). Note however that given that both the studies of Bodart et al. (2010) and McDougall (1979) feature u decaying spatially with increasing distance normal to the source (in our notation, the x_3-direction), a tendency for u to attain a constant value in the boundary-affected region implies that u is amplified relative to the far-field trend. Hence, the results from these studies are in agreement with our results shown in 3.7(b), but opposed to the results of Aronson et al. (1997) and Perot and Moin (1995a) from homogeneous turbulence.

3.5 Turbulent kinetic energy in the boundary-affected region

3.5.1 Turbulent kinetic energy and turbulent kinetic energy flux

We have established that, in the current experiments, $\langle u \rangle_1 / u_0 > 1$ (such that $\langle u \rangle_1 \gtrsim u_{0,\ell_0}$) and $\langle w \rangle_1 / w_0 < 1$ in the boundary-affected region. It is tempting to attribute these results to intercomponent energy transfer from the w^2 component to u^2 component. Measurements of TKE, here defined as $\overline{q'^2} = \overline{u_i' u_i'}/2 \approx (2\overline{u_1' u_1'} + \overline{u_3' u_3'})/2$ (assuming $v \approx u$), are shown in figure 3.8, plotted against scale height ξ/ℓ_0. Two methods of normalisation have been used: figure 3.8(a) shows $\langle \overline{q'^2} \rangle_1$ scaled by $\overline{q_0'^2}$, which denotes the trend expected in the absence of the boundary, obtained from a best fit applied to the data above the boundary-affected region; figure 3.8(b) shows $\langle \overline{q'^2} \rangle_1$ scaled by $\overline{q_{0,\ell_0}'^2}$, which denotes the value of $\overline{q_0'^2}$ evaluated at the edge of the boundary-affected region, at $\xi = \ell_0$. Crucially, figure 3.8(a) shows that the values of $\langle u \rangle_1 / u_0 > 1$ observed in figure 3.7(b) cannot be due only to intercomponent energy redistribution since there is also an increase in TKE within the boundary-affected region relative to the far-field trend. Figure 3.8(b) shows that on average TKE is in fact approximately constant across the boundary-affected region, but that for some experiments $\langle \overline{q'^2} \rangle_1 / \overline{q_{0,\ell_0}'^2} > 1$. Figure 3.8 also shows that there is no clear Reynolds number dependency in the data, instead indicating that the TKE is typically higher in the data obtained using the coarse grid, compared to that obtained with the fine grid, which are shown separately (see figure caption for details).

A likely contributory factor to the increase in TKE is a net production or advection of TKE in this region by the mean flow (which is shown to be the case in section 3.5.2

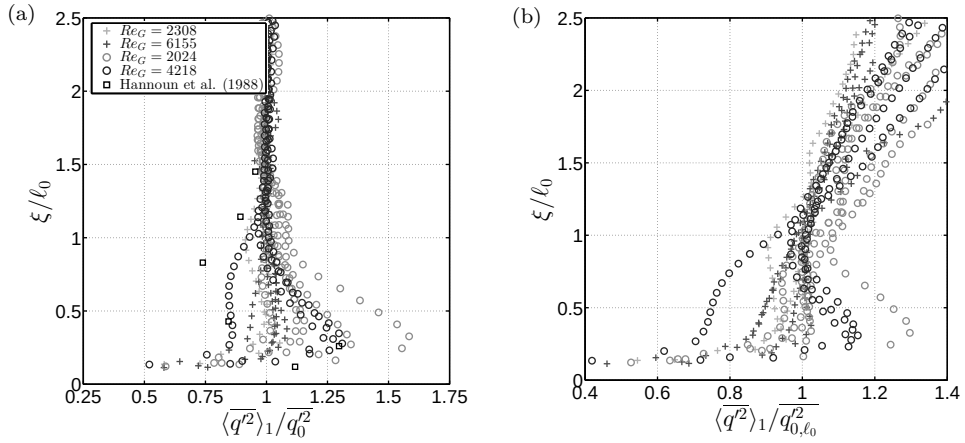


Figure 3.8: (a) Measurements of TKE $\langle\overline{q'^2}\rangle_1$, plotted against scaled height ξ/ℓ_0. Here, $\langle\overline{q'^2}\rangle_1$ has been normalised by the decay $\overline{q_0'^2}$ based on the far-field trend. (b) Shows the same data but with $\langle\overline{q'^2}\rangle_1$ scaled by the value of $\overline{q_0'^2}$ at the height $\xi/\ell_0 = 1$, denoted $\overline{q_{0,\ell_0}'^2}$. The data shown are from the representative subset of experiments (indicated by the ‡ superscripts in table 3.1) for $Re_G = 2024$, 2308, 4218 and 6155 [see legend in (a), which applies to both plots]. For each Re_G, data from the n repeats are shown, where $n = 2$, 4 or 5 (see table 3.1). Also shown are data taken from Hannoun et al. (1988).

below), however the small levels of mean flow typically present in OGT suggest that another mechanism may be, at least partially, responsible for this result. We therefore consider the vertical flux of TKE produced by the oscillation of the grid. Measurements of the vertical flux of TKE, $\langle\overline{u_3'q'^2}\rangle_1$, are shown in figure 3.9(a), plotted against scaled height ξ/ℓ_0. The data have been scaled by their expected values in the absence of the boundary, denoted $(\overline{u_3'q'^2})_0$, obtained by finding a best fit of the form $\langle\overline{u_3'q'^2}\rangle_1 \propto x_3^{-\gamma}$ applied to the data above the boundary-affected region. This normalisation is in line with the method used in section 3.4.2. Under idealised conditions one would expect $\gamma = 3$; however, given the deviations in γ_u and γ_w from 1, the average of the fitted values for γ was 2.4. Hannoun et al. (1988) applied a similar method and reported $\langle\overline{u_3'q'^2}\rangle^{1/3}/u \approx \text{const.}$

The data in figure 3.9(a) show a significant reduction in energy flux in the boundary-affected region ($\xi/\ell_0 < 1$) relative to the far-field trend and are in good agreement with measurements reported previously by Hannoun et al. (1988), which are also shown in figure 3.9(a) (see legend). These results led Hannoun et al. (1988) and Kit et al. (1997) to conclude that the additional energy that would otherwise propagate past the false-floor plate (in its absence) was instead trapped in the boundary-affected region and was the cause of the amplified TKE measured in this region. The current results support this interpretation and indicate that this effect contributes to the observed values of $\langle\overline{q'^2}\rangle_1/\overline{q_0'^2} > 1$. However, the increase in $\langle\overline{q'^2}\rangle_1/\overline{q_{0,\ell_0}'^2} > 1$ cannot be explained by turbulent transport, since in isolation the vertical flux of kinetic energy by turbulent transport would result in $\langle\overline{q'^2}\rangle_1 \approx \overline{q_{0,\ell_0}'^2}$; values of $\langle\overline{q'^2}\rangle_1/\overline{q_{0,\ell_0}'^2} > 1$ would cause re-adjustment of

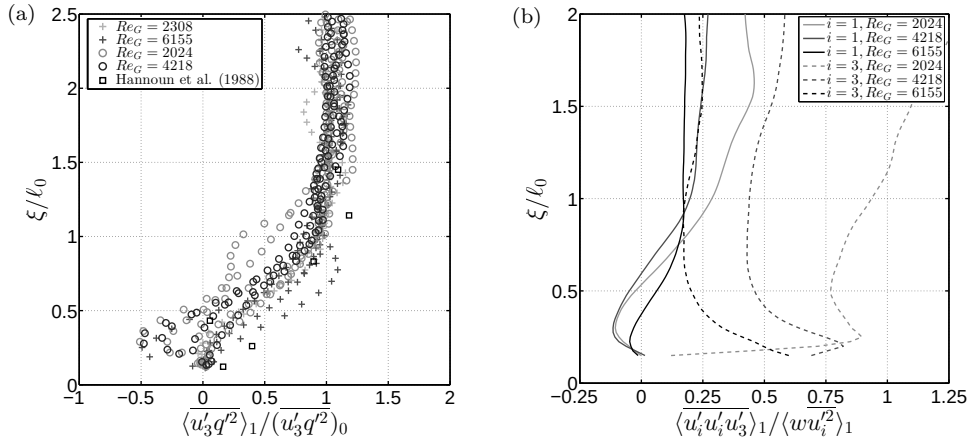


Figure 3.9: (a) Measurements of the vertical flux of TKE, $\langle\overline{u_3'q'^2}\rangle_1$, plotted against scaled height ξ/ℓ_0. The data have been normalised by the trend expected in the absence of the floor plate, denoted $(\overline{u_3'q'^2})_0$. The data shown are from the representative subset of experiments (indicated by the ‡ superscripts in table 3.1) for $Re_G = 2024$, 2308, 4218 and 6155 (see legend). For each Re_G, data from the n repeats are shown, where $n = 2$, 4 or 5 (see table 3.1). Also shown are data taken from Hannoun et al. (1988). (b) Measurements of correlation coefficients $\langle\overline{u_i'u_i'u_3'}\rangle_1/\langle w\overline{u_i'^2}\rangle_1$ for $i = 1$ and $i = 3$ (with the summation convention dropped), plotted against scaled height ξ/ℓ_0. The data are shown are from the representative subset of experiments, for $Re_G = 2024$, 4218 and 6155 (see legend).

the flow beyond the boundary-affected region and an increase in $\overline{q_0'^2}$. We stress that this effect is not a Reynolds number effect. Instead, in section 3.5.2 we show there is a significant increase in advection of u^2 by the mean flow into the central region of the tank for $\xi/\ell_0 < 0.3$, and that this is a major contributing factor to the increase in TKE over this region.

To better understand the vertical flux of TKE in the boundary-affected region we have decomposed $\langle\overline{u_3'q'^2}\rangle_1$ into its component $\langle\overline{u_3'u_1'^2}\rangle_1$, $\langle\overline{u_3'^3}\rangle_1$ and in figure 3.9(b) plotted the correlation coefficients $\langle\overline{u_3'u_1'^2}\rangle_1/\langle wu^2\rangle_1$ and $\langle\overline{u_3'^3}\rangle_1/\langle w^3\rangle_1$ against scaled height ξ/ℓ_0. We note that, as far as we are aware, these measurements are the first reported of this type for OGT. In figure 3.9(b) the notation $\langle\overline{u_i'u_i'u_3'}\rangle_1/\langle w\overline{u_i'^2}\rangle_1$ has been used (with the summation convention dropped) so that the correlation coefficients are given by $i = 1$ and $i = 3$. To avoid oversaturation, the data shown are from only three Reynolds numbers ($Re_G = 2024$, 4218 and 6153) and each data profile (see figure legend) is an average of measurements taken from four (or five) repeated experiments performed under each of these conditions (see table 3.1 for details).

The correlation coefficient $\langle\overline{u_3'^3}\rangle_1/\langle w^3\rangle_1$ of the vertical flux of w^2—which is the 'skewness' of u_3'—is shown in figure 3.9(b) (denoted by the broken lines), and is positive far from the boundary, which indicates a flux of energy away from the grid transported by turbulent fluctuations. As the boundary is approached we observe a gradual increase in magnitude of skewness at $\xi/\ell_0 \approx 0.5$, with a sharper increase at $\xi/\ell_0 \approx 0.3$, before

attaining a maximum value close to the wall. Here an increasing positive skewness physically represents an increasing imbalance between energy associated with turbulent motions towards the boundary, which are increasingly energetic, relative to the energy of turbulent motions away from the boundary. There are two possible effects that could lead to a relative depletion of energy from the vertical component of the turbulent motions away from the plate. (i) It is possible that there is a net intercomponent energy transfer from w^2 to u^2 at the boundary. (ii) Alternatively, it is possible that energy of turbulent motions near the boundary is depleted by viscous effects (splat-antisplat imbalance). In isolation it is not possible to determine which effect is prevalent in this case.

The correlation coefficient $\langle\overline{u_3' u_1'^2}\rangle_1/wu^2$, of the vertical flux of u^2, is shown in figure 3.9(b) (by the solid lines), and is also positive far from the boundary, indicating a flux of energy away from the grid. In contrast to the vertical flux of w^2, on approach to the boundary the vertical flux of u^2 is small but becomes negative, indicating that there is a small net flux of u^2 away from the boundary associated with antisplats. In light of the flux of w^2, the negative flux of u^2 appears to suggest that the effect (i) (above) is prevalent at the boundary, such that antisplats have greater horizontal velocities than splats in the near-wall region as a result of intercomponent energy transfer. However, recall that over this region there was also an increase in $\langle\overline{q'^2}\rangle_1/\overline{q_{0,\ell_0}'^2}$, shown in figure 3.8(b), due to advection by the mean flow; this is a major contributing cause to the more energetic antisplats found in the current results. Hence, it appears that the small upwards flux of u^2 observed for $\xi < 0.5\ell_0$ here is not necessarily a result of (i), but is actually a result of a departure from the zero-mean-shear condition. Recall also that in this region $u > w$ (see figure 3.6b). Hence, as the boundary is approached the vertical flux of TKE is dominated by trends in the vertical flux of $\overline{u_1'^2}$. Hence, it is this reversing orientation of vertical flux of $\langle\overline{u_3' u_1'^2}\rangle_1$ that results in the small upwards flux of $\langle\overline{u_3' q'^2}\rangle_1$ close to the boundary.

Overall, as a result of the blocking of the vertical flux of TKE we observe a net flux of energy into the boundary-affected region. This results in values $\langle u\rangle_1/u_0 > 1$ without the presence of intercomponent energy transfer, since the vertical flux of u^2 that would otherwise arise in the region occupied by the boundary is halted. This will constitute a major factor in the difference in results of u/u_0 and w/w_0 reported in the studies of Aronson et al. (1997) and Perot and Moin (1995a) when compared to studies utilising OGT; these studies represent fundamentally different conditions. Although we have not considered the transport of TKE by viscous or pressure effects here, they are considered in section 3.5.2 below and do not invalidate the previous conclusions.

3.5.2 Reynolds stress and turbulent kinetic energy balances

The steady form of the Reynolds stress transport equations may be written as (see Hinze, 1975, p. 323)

$$0 = \underbrace{-U_k \frac{\partial}{\partial x_k}\overline{u_i' u_j'}}_{A_{ij}^d} \underbrace{-\overline{u_j' u_k'}\frac{\partial U_i}{\partial x_k} - \overline{u_i' u_k'}\frac{\partial U_j}{\partial x_k}}_{\Phi_{ij}} \underbrace{-\frac{\partial}{\partial x_k}\overline{u_i' u_j' u_k'}}_{T_{ij}}$$
$$\underbrace{-\frac{1}{\rho}\left(\frac{\partial}{\partial x_i}\overline{p' u_j'} + \frac{\partial}{\partial x_j}\overline{p' u_i'}\right)}_{\Pi_{ij}^d} + \underbrace{\overline{\frac{1}{\rho}p'\left(\frac{\partial u_j'}{\partial x_i} + \frac{\partial u_i'}{\partial x_j}\right)}}_{\Pi_{ij}^s} + \underbrace{\nu\frac{\partial^2 \overline{u_i' u_j'}}{\partial x_k \partial x_k}}_{D_{ij}} \underbrace{-2\nu\overline{\frac{\partial u_i'}{\partial x_k}\frac{\partial u_j'}{\partial x_k}}}_{\varepsilon_{ij}}. \quad (3.6)$$

The terms A_{ij}^d and Φ_{ij} denote, respectively, transport and production due to the mean flow; T_{ij} and Π_{ij}^d denote, respectively, transport by velocity and pressure fluctuations; Π_{ij}^s is the intercomponent energy redistribution due to the correlation between fluctuating strain and pressure fields; D_{ij} and ε_{ij} denote molecular diffusion and viscous dissipation. Recall that within the inner box's central region—the region of interest—the turbulence is approximately homogeneous on horizontal planes and so $\overline{u_i' u_j'} \approx 0$ for $i \neq j$. Hence, we only consider the transport equations for the Reynolds stresses $\overline{u_1' u_1'}$, $\overline{u_2' u_2'}$ and $\overline{u_3' u_3'}$ (*i.e.* u^2, v^2 and w^2), and the transport equation for TKE which is obtained from the trace of (3.6) noting that $\overline{u_i' u_i'}/2 = \overline{q'^2}$ denotes the TKE. We note that, as far as we are aware, the current results are the first attempt to evaluate (3.6) using data obtained from OGT.

A direct evaluation of (3.6) was not possible, requiring instantaneous measurements of pressure fluctuations and of all three velocity components. Hence, a number of simplifying assumptions were made to allow estimation of certain terms: (i) Based on the symmetry of the experimental set-up, the time-averaged statistical properties of the flow were assumed to be symmetric in the x_1- and x_2-directions. (ii) The turbulence was assumed to be approximately homogeneous in horizontal planes. (iii) The approximations $\overline{(\partial u_1'/\partial x_2)^2} \approx 2\overline{(\partial u_1'/\partial x_1)^2}$ and $\overline{(\partial u_3'/\partial x_2)^2} \approx \overline{(\partial u_3'/\partial x_1)^2}$ were used in calculation of the dissipation terms—relationships which are known to hold for homogeneous, isotropic turbulence (see Pope, 2000, p. 134). Under these assumptions, the relevant terms in (3.6) involving velocity components (and derivatives of velocity components) were calculated from the two-dimensional PIV data obtained in the central (x_1, x_3)-plane. When evaluating the velocity derivatives, the no slip and impermeability conditions ($u_i = 0$) were applied at $\xi = 0$. We note that limitations in the resolution of the PIV method (a resolution of approximately 0.2 cm) is insufficient to capture all scales of turbulent motion and may lead to underestimation of some terms (primarily the diffusion D_{ij} and dissipation ε_{ij} terms) in equation 3.6.

It was not possible to directly estimate the terms Π_{ij}^s and Π_{ij}^d involving pressure fluctuations. These terms were instead estimated from a balance of the remaining

terms in (3.6), the approach used previously by Aronson et al. (1997). Firstly, noting that $\Pi^s_{ii} = 0$ (by continuity) allows estimation of Π^d_{ii} from a balance of the remaining terms in the equation (3.6) for $i = j$. Secondly, using the property that the turbulence is approximately homogeneous in horizontal planes means that $\Pi^d_{11} \approx \Pi^d_{22} \approx 0$ and $\Pi^d_{ii} \approx \Pi^d_{33}$, which enables estimation of Π^s_{11} and Π^s_{33} from the equations (3.6) for $\overline{u'_1 u'_1}$ and $\overline{u'_3 u'_3}$.

The scheme outlined above inevitably produced significant scatter in the results. In an effort to reduce scatter we show here the results for three experimental conditions, with $Re_G = 2024$, 4218 and 6155 (spanning the range of Reynolds numbers considered here). Each experiment was repeated four (or five) times (see table 3.1) and the results obtained from each were averaged, which are shown in figure 3.10, plotted against scaled height ξ/ℓ_0. Note also that the data shown are averaged in the x_1-direction (*i.e.* $\langle\cdot\rangle_1$). In figure 3.10 the left-hand column of data show terms from the TKE budget equation ($\overline{u'_i u'_i}$), while the central and right-hand columns of data show the terms from the u^2 and w^2 budgets. To facilitate comparison, the data have been normalised by the magnitude of the corresponding component of energy dissipation evaluated at the height $\xi = \ell_0$ (denoted $|\varepsilon_{ii}|_{\ell_0}$, $|\varepsilon_{11}|_{\ell_0}$, $|\varepsilon_{33}|_{\ell_0}$ in the caption and figure labels). The top, second and third row of data in figure 3.10 are for $Re_G = 2024$, 4218 and 6155, respectively. We now consider separately the data for the budgets for TKE, u^2 and w^2.

Terms of the TKE budget

The terms for the TKE budget are shown in figure 3.10(a-c), at the three Reynolds numbers. Within the boundary-affected region ($\xi/\ell_0 < 1$), but for $\xi/\ell_0 > 0.3$, the data show that the budget is dominated by comparatively high levels of turbulent transport (T_{ii}). Over this region T_{ii} increases in magnitude, indicating a source of energy in this region. This is a direct result of the blocking of vertical energy flux—note that T_{ii} is the derivative of TKE flux previously considered in section 3.5.1. Across this region dissipation (ε_{ii}) is approximately constant. Hence, it appears that the increase in T_{ii} is the primary cause of the increase in $\langle\overline{q'^2}\rangle_1/\overline{q'^2_0}$ observed over the region $0.3 < \xi/\ell_0 < 1$, shown in figure 3.8(a). In contrast, for $\xi/\ell_0 < 0.3$ the data show that T_{ii} clearly reduces to approximately zero as the energy flux close to the wall is approximately zero. As a consequence, turbulent transport no longer acts as a source of energy in this near-boundary region.

Within the boundary-affected region we also observe an increase in Π^d_{ii} for $\xi/\ell_0 < 0.3$, and at the higher two Reynolds numbers the data exhibit a distinct peak before reducing as the boundary is approached. The results for Π^d_{ii} show good qualitative agreement with data reported in the previous studies by Bodart et al. (2010) and Perot and Moin (1995a). The profile of Π^d_{ii} across the boundary-affected region indicates that higher instantaneous pressure is correlated with turbulent fluctuations incident towards the boundary; that is,

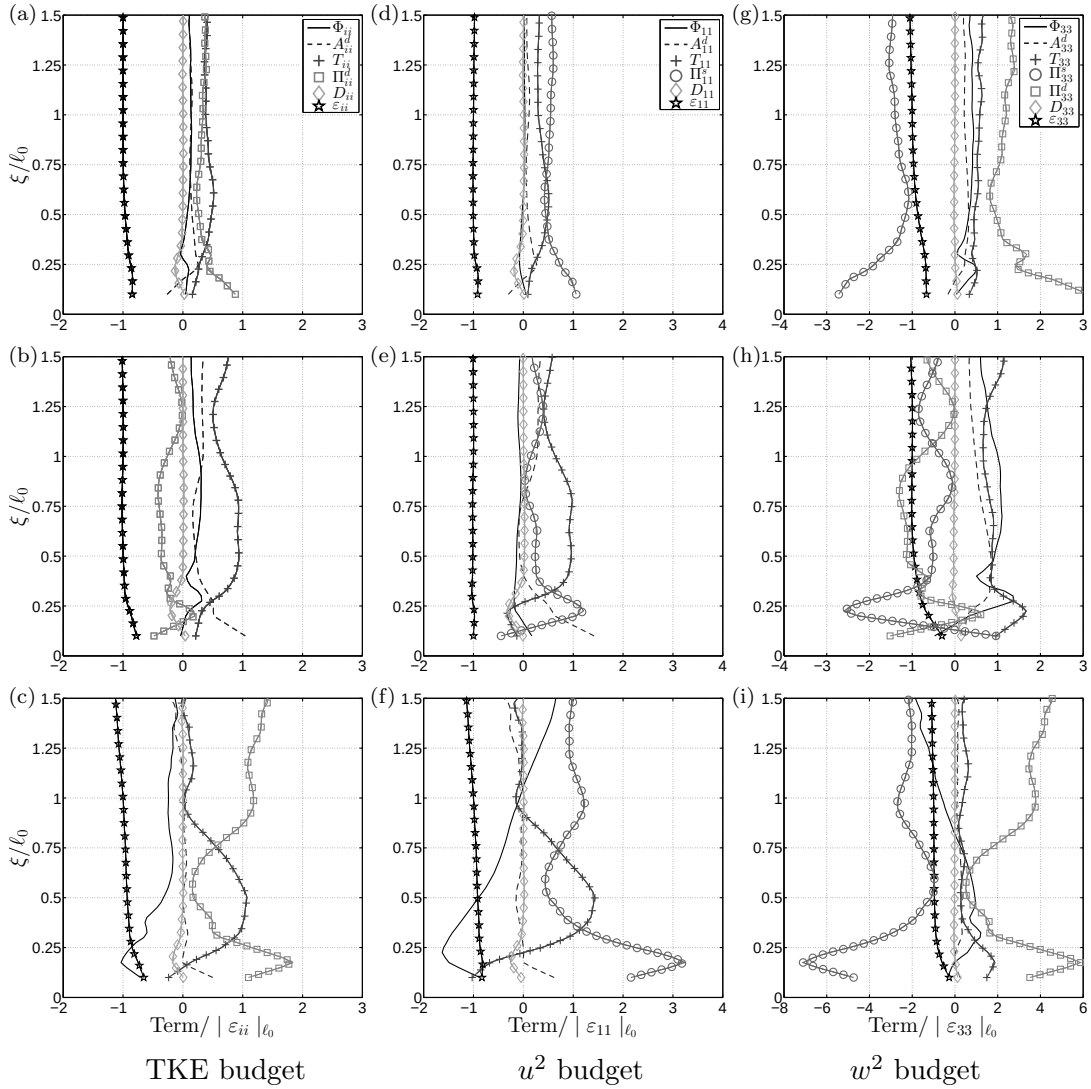


Figure 3.10: Measurements of terms in the transport equations (3.6) for TKE (a-c), for u^2 (d-f), and for w^2 (g-i). Different symbols have been used to denote each term, which are shown in the legends in the top row of plots. Each term has been spatially averaged in the x_1-direction (*i.e.* $\langle\cdot\rangle_1$), and has been normalised by the magnitude of the corresponding component of dissipation evaluated at the edge of the boundary-affected region, $|\varepsilon_{ij}|_{\ell_0}$. Panels (a,d,g) correspond to a grid Reynolds number of $Re_G = 2024$, (b,e,h), to $Re_G = 4218$ and (c,f,i) to $Re_G = 6155$. Recall that $\Pi_{ii}^s = 0$ by continuity and that $\Pi_{11}^d \approx 0$, since turbulence is approximately homogeneous on horizontal planes.

here the turbulence is homogeneous only in planes parallel to the grid, and so $\Pi_{ii}^d = \Pi_{33}^d$ (note that in figure 3.10, the magnitudes of Π_{ii}^d and Π_{33}^d are not the same as they have been normalised differently, by $|\varepsilon_{ii}|_{\ell_0}$ and $|\varepsilon_{33}|_{\ell_0}$, respectively). This correlation between high pressure events and fluid elements incident towards the boundary can be understood by considering that splats are more energetic than antisplats, so result in a greater instantaneous pressure. For $\xi/\ell_0 \lesssim 0.2$, the values of Π_{ii}^d reduce as the transport of pressure fluctuations by the turbulent velocity must tend to zero at the limit of the wall.

The data for dissipation of TKE (ε_{ii}) show that TKE is lost throughout the domain (due to deformation work done by viscous stresses). Previous studies (using DNS) have suggested that TKE dissipation increases significantly as the boundary is approached (Bodart et al., 2010; Perot and Moin, 1995a), however, the PIV data reported here did not resolve scales sufficiently close to the boundary to validate this proposal. In addition, figure 3.10 indicates that the transport of turbulent kinetic energy by viscous diffusion (D_{ii}) is negligible beyond the viscous sublayer ($\xi/\ell_0 > 0.3$). However, in previous studies D_{ii} has been shown to increase very close to the wall due to the rapid reduction of velocities in this region (Bodart et al., 2010; Perot and Moin, 1995a). Hence, viscous diffusion provides a source of turbulent kinetic energy to sustain turbulence in the near-wall region, sourced from the outer viscous sub-layer and blocking layer.

The results show that Φ_{ii} (responsible for extraction of kinetic energy by turbulent fluctuations from the mean flow) is small except for the case $Re_G = 6155$. That is, for the low and medium Reynolds number cases, the total gain of TKE from the mean flow is negligible. The increase in Φ_{ii} (for $\xi/\ell_0 < 0.6$) evident at $Re_G = 6155$, indicates a Reynolds number effect, although it is unclear if this is a result of mechanisms governing the interaction of turbulence with the plate or not. However, A^d_{ii} (responsible for the transport of kinetic energy by the mean flow) exhibits a significant increase in magnitude for $\xi/\ell_0 < 0.25$; this is most likely a contributing factor to the increase in $\langle\overline{q'^2}\rangle_1/\overline{q^2_{0,\ell_0}}$ observed as the boundary is approached (shown previously in figure 3.8b), together with the upwards flux of u^2 discussed in section 3.5.1. We conclude that although the effects of convection and production have not been eliminated in the current apparatus, their effects are comparatively small overall.

Terms of the Reynolds stress budget for u^2

The terms of the transport equation for $\overline{u'_1u'_1} = u^2$ are shown in figure 3.10(d-f), which exhibit similar traits to the data for the TKE budget (discussed above). The turbulent transport term, T_{11}, has a significant effect; note that for turbulence that is approximately homogeneous in horizontal planes, $T_{11} \approx \partial\overline{u'_1u'_1u'_3}/\partial x_3$ (*i.e.* the vertical flux of u^2), since $\partial\overline{u'_1u'_1u'_1}/\partial x_1,\ \partial\overline{u'_1u'_1u'_2}/\partial x_2 \approx 0$. The increase in T_{11} evident in figure 3.10(d-f) for $0.3 < \xi/\ell_0 < 1$ is due to the presence of the floor plate, which acts to halt the vertical flux of TKE. A similar, but less significant, increase in T_{11} was found by Bodart et al. (2010). In contrast, in the studies by Perot and Moin (1995a) and Aronson et al. (1997) the T_{11} term was not a dominant component of the transport equation, however this difference is reconciled due to the homogeneous nature of turbulence in the x_3-direction used in those studies.

The pressure-strain term, Π^s_{11}, is also significant. For $\xi > \ell_0$, Π^s_{11} is small and approximately constant, due primarily to the constant degree of isotropy in this region (see figure 3.6); where the turbulence is approximately isotropic above the boundary-affected

region, we expect little net intercomponent energy transfer. However for $0.3 < \xi/\ell_0 < 1$, the data for Π_{11}^s show a gradual and slight reduction, which indicates a reduction in energy transfer from w^2 to u^2 relative to far-field trend. It is worth noting that negative values of Π_{11}^s would indicate a transfer of energy from the energy rich u^2 component to the energy poor w^2 component, an effect that was observed in the results reported by Aronson et al. (1997), Bodart et al. (2010) and Perot and Moin (1995a) and has been denoted as a 'return-to-isotropy' energy transfer. However, note that for $0.3 < \xi/\ell_0 < 1$ it is T_{11} that represents the dominant source of energy, and so the increased levels of $\langle u \rangle_1/u_0$ observed over this region (see figures 3.7b and 3.7(d)) are primarily due to transport processes and not intercomponent redistribution. As a result, we propose that the near-constant values of $\langle u \rangle_1/u_{0,\ell_0} \approx 1$ for $\xi < \ell_0$ shown in figure 3.7(d) and reported by Bodart et al. (2010) and McDougall (1979) are primarily the result of turbulent transport of TKE. In addition, noting that in the study of Bodart et al. (2010) there is no mean flow, we propose that our values of $\langle u \rangle_1/u_{0,\ell_0} > 1$ for $\xi < \ell_0$ (not observed by Bodart et al., 2010; McDougall, 1979) are a result of the mean flow present in the current experiment.

For $\xi/\ell_0 < 0.3$ the balance is dominated by rapid reduction in T_{11} coinciding with an increase in Π_{11}^s, which signifies that the dominant mechanism governing the budget changes from being turbulent transport to energy redistribution. The significant increase in the pressure-strain term (Π_{11}^s), forming a positive peak, indicates that energy is transferred from the energy poor w^2 component to the energy rich u^2 component; a peak in Π_{11}^s close to the wall was also observed in the studies by Perot and Moin (1995a), Aronson et al. (1997) and Bodart et al. (2010).

Terms of the Reynold stress budget for w^2

The terms of the transport equation for $\overline{u_3' u_3'} = w^2$ are shown in figure 3.10(g-i). For turbulence that is approximately homogeneous in planes parallel to the boundary, the turbulent transport term $T_{33} \approx -\partial(\overline{u_3' u_3' u_3'})/\partial x_3$, which is the gradient of the vertical flux of w^2, previously considered in section 3.5.1. In contrast to the observations for T_{11}, the data show that T_{33} remains approximately constant in the region $0.3 < \xi/\ell_0 < 1$, but increases and attains a peak value in the near-boundary region $\xi/\ell_0 < 0.3$, and reduces towards zero as the boundary is approached. A similar near-boundary peak was observed by Perot and Moin (1995a) (for spatially homogenous turbulence in the far field), but notably not in the study by Bodart et al. (2010), using inhomogeneous turbulent conditions more comparable to those reported here. In contrast to the tangential component, in this case the near-wall peak observed in the current results indicates increasing skewness towards the boundary. This is also the case for the results of Perot and Moin (1995a). We can view this peak as being due to a net diffusion of energy into the near-boundary region, as there is lack of energetic antisplats to transport energy out

again.

The key contrasts between the data in the u^2 and w^2 transport equations can be summarised as follows. At the edge of the boundary-affected region the transport equation of u^2 is dominated by changes in T_{11}; the blocking condition ($w = 0$ at $\xi = 0$) halts the vertical flux of $\overline{u_1' u_1' u_3'}$ towards the boundary, giving rise to observed increase in $\langle u \rangle_1 / u_0$. In contrast, at the edge of the boundary-affected region the transport equation of w^2 is dominated by changes in Π_{33}^d; changes in T_{33} are less significant. This differences arises since at $\xi \approx \ell_0$ the kinematic blocking condition acts upon w^2 manifesting itself in the pressure field, but does not act directly upon u^2. We stress that, as far as we are aware, similar conclusions have not previously been proposed.

3.6 Discussion

In this section we attempt to reconcile the results previously presented to propose the underlying mechanisms governing the interaction of OGT with a solid impermeable boundary. Firstly, the behaviour of energy flux and turbulent transport terms gives us an indication of the role of viscosity in the near-wall behaviour of the turbulence. This aspect of the mechanism can be explained using the splat-antisplat disequilibrium model (see, for example, Perot and Moin, 1995a). The increasing positive measurements of the skewness in u_3' (henceforth denoted $\sigma = \overline{u_3'^3}/w^3$) for $\xi/\ell_0 < 1$ (shown by the broken lines in figure 3.9b), indicate that on average motions towards the boundary (splats) are more energetic than motions away from the boundary (antisplats), and this increased skewness occurs over the region $0.2 \lesssim \xi/\ell_0 \lesssim 0.5$, where viscous effects are significant. In addition, positive values of pressure transport (Π_{33}^d) adjacent to the boundary indicate that over this region there is also a correlation between high instantaneous pressure events and fluid motions incident towards the boundary. This can be interpreted as splats resulting in a greater instantaneous pressure than antisplats on average, which indicates that splats are more energetic than antisplats. Hence, there is greater energy transfer from w^2 to u^2 in the splat process in comparison to the energy transfer from the u^2 to w^2 in the antisplat process. The near-wall ($\xi/\ell_0 \lesssim 0.3$) peaks in magnitude of Π_{11}^s and Π_{33}^s evident in 3.10(d-i) also show this to be the case. This splat-antisplat imbalance increases to a maximum at the edge of the viscous sub-layer, at $\xi/\ell_0 \approx 0.2$-0.3. This supports the proposal of Perot and Moin (1995a) that this mechanism is, at least in part, driven by the increased dissipation of TKE close to the boundary that results in antisplats of reduced energy relative to splats. Due to the role of enhanced dissipation in this mechanism we expect the mechanism to only be significant in the viscous sub-layer.

However, the behaviour of the pressure-strain term Π_{11}^s in figure 3.10(d-f) for $\xi/\ell_0 \gtrsim 0.3$ also indicates the presence of another redistributive energy transfer process. It is known that the pressure-strain term in homogeneous turbulence contributes to the

transfer of energy from energy-rich components to energy-poor components (see for example Chung and Kim, 1995; Choi and Lumley, 2001). Walker et al. (1996) proposed that a similar 'return-to-isotropy' energy redistribution effect should also be present in the boundary-affected region of the interaction between zero-mean-shear turbulence and a boundary. To support this conclusion in OGT we would expect Π_{11}^s to be negative for $\xi/\ell_0 < 1$, indicating a transfer of energy from u^2 to w^2 since over this region $u > w$. Note that the intensity of this mechanism in the pressure-strain term should increase as ξ reduces due to increasing anisotropy (see figure 3.6), but may be masked by the viscous effect very close to the wall. This effect is indeed observed in the results of Aronson et al. (1997), Bodart et al. (2010) and Perot and Moin (1995a). In contrast to previous studies using zero-mean-shear turbulence, note that in the current study since the turbulence is weakly anisotropic for $\xi/\ell_0 > 1$, we observe non-zero values of Π_{11}^s beyond the boundary-affected region; in figure 3.10(d-f) we see that for $\xi/\ell_0 > 1$, Π_{11}^s promotes a transfer from w^2 to u^2. Disregarding the near-wall peak associated with viscous effects, we see that as the boundary is approached Π_{11}^s reduces, indicating that the energy transfer from w^2 to u^2 is reduced as the ratio w/u reduces from approximately 1 to 0 (indicating increasing anisotropy). This has clear parallels to previous results in zero-mean-shear turbulence that demonstrated a 'return-to-isotropy' energy transfer. It is worth noting that this 'return-to-isotropy' energy transfer has its root in a kinematic effect, since it is the blocking effect of the wall that results in the reduction of w^2, causing an increase in anisotropy.

The viscous effects and the 'return-to-isotropy' mechanism discussed above do not explain the observations that $\langle u \rangle_1 / u_0 > 1$ over the region $\xi/\ell_0 \gtrsim 0.3$ in figure 3.7. Recall, however, that the blocking of the vertical energy flux leads to a net transport of u^2 into the boundary-affected region (see figure 3.9 or figure 3.10d-f). Noting that the turbulent energy flux is similar to a diffusive effect in the sense that it transfers energy from an energy-rich region to an energy-poor region, when considered in isolation from other effects the flux would act to increase u up to the limit that it was constant across the boundary-affected region, shown in figure 3.7(d). Hence, given u_0 undergoes a spatial decay based on the far-field trend, this results in $u/u_0 > 1$ over $\xi/\ell_0 < 1$. Therefore, crucially it appears that turbulent transport plays a significant role in amplification of the horizontal turbulent velocity component in the boundary-affected region relative to the far-field trend. This mechanism goes some way to explain the disparity of observations of u/u_0 reported in the literature (shown in figure 3.7(b)); studies conducted in homogeneous turbulence are essentially a limiting case of the problem reported here, in the sense that there is no turbulent kinetic energy flux in homogeneous turbulence. Since here it is the kinetic energy flux that is the primary factor in resulting in values of $u/u_0 > 1$, eliminating this effect implies that $u/u_0 \approx 1$ in line with the observations of studies conducted in homogeneous turbulence (Aronson et al., 1997; Perot and Moin, 1995a)

and the results shown in figure 3.7(c). An important result of this mechanism is that the use of a zero-mean-shear condition alone is not sufficient to predict the effect of the boundary on turbulent velocity components; inhomogeneity in the x_3-direction should be considered.

A critical implication of the blocking of the turbulent kinetic energy flux that arises in turbulence that undergoes a spatial decay normal to the boundary is that values of $u/u_0 > 1$ and $w/w_0 < 1$ (*i.e.* relative to the far-field trend) can occur in the boundary-affected region in the absence of intercomponent energy transfer from w^2 to u^2. Note however that our results do not necessarily suggest that intercomponent energy transfer is independent of the spatial decay of turbulent velocities that gives rise to the vertical turbulent kinetic energy flux. For example, consider the hypothetical situation in which we can control the rate of spatial decay of turbulent velocities (γ_u, γ_w); increasing γ_u and γ_w will intensify the vertical flux of TKE. Since in the boundary-affected region the vertical flux of TKE acts to increase u but not w (shown in figure 3.10), increasing γ_u and γ_w leads to an increase in anisotropy in the boundary-affected region relative to a smaller value of γ_u and γ_w. Hence, this greater anisotropy would promote a stronger 'return-to-isotropy' intercomponent energy transfer.

Links between a statistical structure of OGT (spatially decaying with increasing x_3) and the pressure-strain term have also been proposed in the literature (Magnaudet, 2003; Bodart et al., 2010), by using skewness (σ) to describe the x_3 inhomogeneity. Magnaudet (2003) proposed a relationship between the pressure-strain correlation term and turbulent transport by considering the tangential component of the Reynolds stress transport equation for OGT under ideal conditions; namely

$$0 = T_{11} + \Pi^s_{11} + D_{11} + \varepsilon_{11}. \tag{3.7}$$

With viscous diffusion taken to be small (which figure 3.10 shows is valid for $\xi/\ell_0 \gtrsim 0.3$), the sign of the pressure-strain term depends only upon the relative magnitude of the turbulent transport and dissipation terms. Magnaudet (2003) derived a simple model of the third-order moments present in turbulent transport terms to predict that the sign of the pressure-strain term depends on the skewness of the velocity field. This model assumes that viscous diffusion is small and that dissipation is unaffected by the presence of the boundary. The model is given by

$$\Pi^s_{11} = \Pi^s_{22} \approx \varepsilon_{\infty,0}\left(\frac{2}{3} - \sigma\right) \text{ as } \xi \to 0, \tag{3.8}$$

where ε_∞ denotes the total dissipation of TKE ($\varepsilon_\infty = \varepsilon_{ii}/2$) that would exist if the boundary were absent, and $\varepsilon_{\infty,0}$ is the value at $\xi = 0$. The model predicts that at the limit of the wall for $\sigma < 2/3$, there is a transfer of energy from the (energy-poor) w^2 to the (energy-rich) u^2, but that for $\sigma > 2/3$ the transfer was reversed; a 'return-to-isotropy' energy transfer. Given that the model assumes that diffusion (D_{ij}) is small and that

dissipation (ε_{ij}) is unaffected by the presence of the boundary—which is not valid in the viscous sub-layer, for an impermeable boundary—the model is valid only in the limit of large Reynolds number.

When comparing the model of Magnaudet (2003) to the current results note that for $\sigma > 2/3$ the prediction of this model is to promote a 'return-to-isotropy' energy transfer which is stronger at increasing skewness. Crucially, in regions in which the assumptions made by Magnaudet (2003) are approximately valid, this result is the same as our previous conclusion that as the decay exponents γ_u and γ_w increase we observe a stronger 'return-to-isotropy' energy transfer. However, our considerations of turbulent transport do not support the concept of a 'critical skewness' at $\sigma = 2/3$ below which the pressure-strain term promotes anisotropy. This difference most likely arises as a consequence of the limitations inherent in the derivation of the model of Magnaudet (2003). In contrast to our conclusion, Bodart et al. (2010) argue that their results invalidate the model proposed by Magnaudet (2003) since their results indicate a near-wall peak in pressure-strain that promotes an energy transfer from the (energy-poor) w^2 to the (energy-rich) u^2 under the condition $\sigma \approx 2$. However, note that the model of Magnaudet (2003) is not valid in the region in which the near-wall peak in pressure-strain reported by Bodart et al. (2010) occurs, since in this region viscous diffusion is not small and dissipation is increased. Values of pressure-strain reported by Bodart et al. (2010) further away from the wall (in regions of small viscous diffusion) do in fact support 'return-to-isotropy' energy transfer in agreement with the prediction of the model of Magnaudet (2003) and the current results.

Bodart et al. (2010) also proposed a relationship between skewness and the pressure-strain term. They note that when a fluid element of size ℓ, with characteristic velocity u_3', interacts with an impermeable (stationary) boundary, there is a resulting pressure rise of $p'/\rho \approx u_3'^2/2$ and a strain rate of $\partial u_3'/\partial x_3 \approx -u_3'/\ell$. Hence,

$$\overline{\frac{p'}{\rho}\frac{\partial u_3'}{\partial x_3}} \approx \frac{-\overline{u_3'^3}}{2\ell} \sim \frac{-\sigma w^3}{\ell}. \tag{3.9}$$

As a result, Bodart et al. (2010) argue that although the transfer of energy in the near-wall region is determined by the effect of splat-antisplat imbalance, that this imbalance is essentially governed by the dis-symmetry of the fluctuating field (determined by σ). They argue that this dis-symmetry gives rise to a net redistributive energy transfer and conclude that the, previously discussed, effects of viscosity on splat-antisplat disequilibrium are marginal. However, note that any degree of net intercomponent energy transfer does not appear to be significant; in the results of Bodart et al. (2010), $\Pi_{11}^s > |\varepsilon_{11}|$ by a small amount for only a limited region close to the boundary, in line with the results presented here in figure 3.10(d-f). In addition, the effects of this energy transfer do not appear to be significant enough to cause an increase in the absolute magnitude of u in the boundary-affected region; that is, Bodart et al. (2010) observe a monotonic reduction

of u and recall that we have attributed our values of $\langle u \rangle_1 / u_{0,\ell_0} > 1$ largely to the effects of advection. Hence, although boundary-normal inhomogeneity may have an effect on intercomponent energy transfer very close to the wall, in the current results any effects appear marginal in light of the transport-based effects on turbulent velocity components in the boundary-affected region.

Finally, we return to a central idea of Hunt and Graham (1978); the significant differences found in the results reported in early studies were attributed to Reynolds number effects (Uzkan and Reynolds, 1967; Thomas and Hancock, 1977). Therefore, the question arises what, if any, are the Reynolds number effects present in this interaction? In sections 3.4 and 3.5 we were unable to identify a clear link between our results and Reynolds number across the fairly narrow range of Reynolds numbers achievable with OGT. Other studies using OGT have reported comparable values of $\max(u/u_0) > 1$ across a similar range of Reynolds number (Kit et al., 1997; Brumley and Jirka, 1987; Hannoun et al., 1988). In addition, studies of a boundary inserted into a field of established homogeneous turbulence have reported results with $\max(u/u_0) \approx 1$ at long times after boundary insertion, across only a limited range of Reynolds numbers (*i.e.* $Re_T \approx$ 50-425 in Perot and Moin, 1995a; Aronson et al., 1997). In contrast, Perot and Moin (1995a) identified that terms of the u^2 budget scale on a viscous coordinate system and that the magnitude of the pressure-strain term increased at higher Reynolds number. This can be understood by noting that the viscous effects present in the splat-antisplat disequilibrium mechanism will display Reynolds number dependency, since the ratio δ_v/δ_s decreases with increasing Reynolds number (Hunt and Graham, 1978), where δ_v denotes the thickness of the viscous sub-layer. Hence, although Reynolds number effects are predicted to feature in the interaction, results to support this hypothesis are limited. It is clear that studies across a much broader range of Reynolds number are needed to address this issue.

3.7 Conclusions

We have reported results from an experimental study of the interaction between OGT and a solid boundary (aligned parallel to the grid). The results show that there are three main mechanisms governing the interaction; viscous effects resulting in splat-antisplat disequilibrium; 'return-to-isotropy' intercomponent energy transfer; turbulent transport. The results have shown the importance of turbulent transport to this interaction, an aspect that has received little focus in previous studies. In particular, it was the blocking of a vertical TKE flux, away from the grid towards the boundary, that was the dominant feature in producing the observed amplification of the boundary-tangential turbulent velocity component. This is a critical point; previously it has been assumed that the increase in boundary-tangential turbulent velocity component was due primarily to

energy transfer from the boundary-normal turbulent velocity component; our results indicate that this is not the case. This mechanism has also gone someway to explain the differences in results previously presented in the literature, by noting that results conducted in otherwise homogeneous turbulence can be viewed as the limiting case at which the effects of the turbulent transport mechanism tend to zero, such that the amplification of the boundary-tangential turbulent velocity component is small.

The results presented here also support other, previously proposed, mechanisms that do act through intercomponent energy transfer; viscous effects resulting in splat-antisplat disequilibrium (Perot and Moin, 1995a) and stress anisotropy effects (Walker et al., 1996). Splat-antisplat disequilibrium is a viscous mechanism driven primarily by the dissipation of TKE, as proposed by Perot and Moin (1995a), that dominates the interaction in the viscous sub-layer. This mechanism is characterised by more energetic motions towards the boundary than away, that manifests as an intercomponent energy transfer that promotes anisotropy, described by the pressure-strain correlation term Π_{ij}^s. Outside the viscous sub-layer Π_{ij}^s acts to transfer energy from u^2 to w^2 in a so called 'return-to-isotropy', as proposed by Walker et al. (1996). This mechanism has its root in a kinematic effect; in the boundary-affected region the blocking of w promotes stress anisotropy that promotes the 'return-to-isotropy' energy transfer in the boundary-affected region as in elsewhere in the flow. We have also proposed that these mechanisms are not independent of the energy flux mechanism discussed above; we propose that Π_{ij}^s should promote a stronger 'return-to-isotropy' energy transfer mechanism as the degree of inhomogeneity in the boundary-normal direction increases, in line with the prediction of Magnaudet (2003), due to the effects of energy flux towards the boundary. Hence, it is clear that the effect of a solid impermeable boundary on turbulent velocity components in zero-mean-shear turbulence depends critically on the nature of the turbulence (homogeneous versus inhomogeneous).

Acknowledgements

The authors acknowledge Jim Meakin and Steve Lawton for technical support with the experimental apparatus. MWM acknowledges financial support through an Engineering and Physical Sciences Research Council Studentship (number 1510466).

References

Aronson, D., Johansson, A. V., and Löfdahl, L. (1997). Shear-free turbulence near a wall. *J. Fluid Mech.*, 338:363–395.

Atkinson, J. F., Damiani, L., and Harleman, D. R. F. (1987). Comparison of velocity measurements using a laser anemometer and a hot-film probe, with application to grid-stirring entrainment experiments. *Phys. Fluids*, 30:3290–3292.

Biringen, S. and Reynolds, W. C. (1981). Large-eddy simulation of the shear-free turbulent boundary layer. *J. Fluid Mech.*, 103:53–63.

Bodart, J., Cazalbou, J. B., and Joly, L. (2010). Direct numerical simulation of unsheared turbulence diffusing towards a free-slip or no-slip surface. *J. Turbul.*, 11(48):1–18.

Brumley, B. H. and Jirka, G. H. (1987). Near-surface turbulence in a grid-stirred tank. *J. Fluid Mech.*, 183:235–263.

Choi, K.-S. and Lumley, J. L. (2001). The return to isotropy of homogeneous turbulence. *J. Fluid Mech.*, 436:59–84.

Chu, C. C. and Falco, R. E. (1988). Vortex ring/viscous wall layer interaction model of the turbulence production process near walls. *Exp. Fluids*, 6:305–315.

Chung, M. K. and Kim, S. K. (1995). A nonlinear return-to-isotropy model with Reynolds number and anisotropy dependency. *Phys. Fluids*, 7(6):1425–1437.

Dalziel, S. B. (2006). Digiflow user guide: http://www.damtp.cam.ac.uk/lab/digiflow/.

De Silva, I. P. D. and Fernando, H. J. S. (1994). Oscillating grids as a source of nearly isotropic turbulence. *Phys. Fluids*, 6:2455–2464.

Dickinson, S. C. and Long, R. R. (1983). Oscillating-grid turbulence including effects of rotation. *J. Fluid Mech.*, 126:315–333.

Dohan, K. and Sutherland, B. R. (2002). Turbulence time scales in mixing box experiments. *Exp. Fluids*, 33:709–719.

Fernando, H. J. S. and De Silva, I. P. D. (1993). Note on secondary flows in oscillating grid, mixing box experiments. *Phys. Fluids*, 5:1849–1851.

Hannoun, I. A., Fernando, H. J. S., and List, E. J. (1988). Turbulence structure near a sharp density interface. *J. Fluid Mech.*, 189:189–209.

Hinze, J. O. (1975). *Turbulence*. McGraw-Hill, 2nd edition.

Hopfinger, B. J. and Linden, P. F. (1982). Formation of thermoclines in zero-mean-shear turbulence subjected to a stabilizing buoyancy flux. *J. Fluid Mech.*, 11:157–173.

Hopfinger, B. J. and Toly, J. A. (1976). Spatially decaying turbulence and its relation to mixing across density interfaces. *J. Fluid Mech.*, 78(1):155–175.

Hunt, J. C. R. (1984). Turbulence structure in thermal convection and shear-free boundary layers. *J. Fluid Mech.*, 138:161–184.

Hunt, J. C. R. and Graham, J. M. R. (1978). Free-stream turbulence near plane boundaries. *J. Fluid Mech.*, 84(2):209–235.

Kit, E. L. G., Strang, E. J., and Fernando, H. J. S. (1997). Measurement of turbulence near shear-free density interfaces. *J. Fluid Mech.*, 334:293–314.

Magnaudet, J. (2003). High-Reynolds-number turbulence in a shear-free boundary layer: revisiting the Hunt-Graham theory. *J. Fluid Mech.*, 484:167–196.

McDougall, T. J. (1979). Measurements of turbulence in a zero-mean-shear mixed layer.

J. Fluid Mech., 94(3):409–431.

McKenna, S. P. and McGillis, W. R. (2004). Observations of flow repeatability and secondary circulation in an oscillating grid-stirred tank. *Phys. Fluids*, 16(9):3499–3502.

Nokes, R. I. (1988). On the entrainment rate across a density interface. *J. Fluid Mech.*, 188:185–204.

Perot, B. and Moin, P. (1995). Shear free turbulent boundary layers, Part 1, physical insights into near-wall turbulence. *J. Fluid Mech.*, 295:199–227.

Pope, S. B. (2000). *Turbulent Flows*. Cambridge University Press, 1st edition.

Tennekes, H. and Lumley, J. L. (1972). *A first course in turbulence*. MIT press, 1st edition.

Thomas, N. H. and Hancock, P. E. (1977). Grid turbulence near a moving wall. *J. Fluid Mech.*, 82(3):481–496.

Thompson, S. M. and Turner, J. S. (1975). Mixing across an interface due to turbulence generated by an oscillating grid. *J. Fluid Mech.*, 67(2):349–368.

Uzkan, T. and Reynolds, W. C. (1967). A shear-free turbulent boundary layer. *J. Fluid Mech.*, 28(4):803–821.

Variano, E. A. and Cowen, E. (2008). A random-jet-stirred turbulence tank. *J. Fluid Mech.*, 604:1–32.

Walker, D. T., Leighton, R. I., and Garza-Rios, L. O. (1996). Shear-free turbulence near a flat free surface. *J. Fluid Mech.*, 320:19–51.

Wan Mohtar, W. H. M. and Munro, R. J. (2013). Threshold criteria for incipient sediment motion on an inclined bedform in the presence of oscillating-grid turbulence. *Phys. Fluids*, 25:015103.

Xuequan, E. and Hopfinger, E. J. (1986). On mixing across an interface in stably stratified fluid. *J. Fluid Mech.*, 166:227–244.

Chapter 4

Analysis of intercomponent energy transfer in the interaction of oscillating-grid turbulence with an impermeable boundary

This chapter is comprised of an article currently under review for publication. Article reference:

> McCorquodale, M. W. and Munro, R. J. (2017). Analysis of intercomponent energy transfer in the interaction of oscillating-grid turbulence with an impermeable boundary. ***Submitted to:*** *Physics of Fluids*.

For ease of the reader the following amendments to the structure of the paper have been included:

1. Section and figure numbers are amended to include a chapter reference to ensure consistency across the thesis.
2. Contact details for corresponding authors have not been included
3. Footnotes are included to facilitate references to other chapters of the thesis

Nomenclature

E_u, E_w	Energy spectra for the horizontal/vertical velocity fluctations
f	Grid oscillation frequency
f_E	Spectral frequency
H	Distance between false-floor and grid's mean position
ℓ_w	Transverse integral length scale
L	Half-width of inner box
M	Mesh spacing
p'	Fluctuating pressure
P	Probability
P_{Q_i}	Probability associated with the ith quadrant
Q_i	Label for the ith quadrant
$Re_G \equiv MSf/\nu$	Grid Reynolds number
S	Grid stroke
t	Time
u_i	Instantaneous velocity component
$u_i' \equiv u_i - U_i$	Turbulent velocity component
$U_i \equiv \overline{u}_i$	(Time-averaged) mean velocity component
$u \equiv \overline{u_1'^2}^{1/2}$, $v \equiv \overline{u_2'^2}^{1/2}$, $w \equiv \overline{u_1'^3}^{1/2}$	Root-mean-square turbulent velocity component
$u_{\delta_s}, w_{\delta_s}$	Value of u, w evaluated at $\xi = \delta_s$
u_{Q_i}	Conditional rms value of u_1' associated with Q_i
x_1, x_2, x_3	Co-ordinate system with origin at center of grid's mean position
δ_s	Thickness of boundary-affected region
δ_v	Thickness of viscous sublayer
ν	Kinematic viscosity
$\xi \equiv H - x_3$	Distance normal to and above false floor
ρ	Density
ϕ_T	Constant
A_{ij}^d	Transport due to the mean flow
Φ_{ij}	Production due to the mean flow
T_{ij}	Transport by velocity fluctuations
Π_{ij}^d	Transport by pressure fluctuations
Π_{ij}^s	Pressure-strain correlation (Intercomponent energy transfer)
D_{ij}	Molecular diffusion
ε_{ij}	Viscous dissipation

$\lvert\varepsilon_{11}\rvert_{\delta_s}$	Magnitude of ε_{11} evaluated at $\xi = \delta_s$
$\overline{p}$	Time-average of quantity p
$\lvert p\rvert$	Magnitude of quantity p
$\langle p\rangle_i$	Spatial average of quantity p in the ith direction

Analysis of intercomponent energy transfer in the interaction of oscillating-grid turbulence with an impermeable boundary

Mark W. McCorquodale[1] **and R. J. Munro**[1]

[1]Faculty of Engineering, The University of Nottingham, Nottingham NG7 2RD, UK

New experimental results are presented that investigate the nature of the intercomponent energy transfer that occurs in the interaction between oscillating-grid turbulence and a solid impermeable boundary, using instantaneous velocity measurements obtained from two-dimensional particle imaging velocimetry (PIV). Estimates of the pressure-strain correlation term (Π_{ij}^s) of the transport equation of the Reynolds stress tensor, which represents intercomponent energy transfer, are obtained using the PIV data from a balance of the remaining terms of the transport equation. The influence of Π_{ij}^s on the flow is examined by computing the energy spectra and conditional turbulent statistics associated with events in which intercomponent energy transfer is thought to be concentrated. Data reported here are in support of viscous and 'return-to-isotropy' mechanisms governing the intercomponent energy transfer previously proposed, respectively, by Perot & Moin [*J. Fluid Mech.*, vol. 295, 1995, pp. 199–227] and Walker *et al.* [*J. Fluid Mech.*, vol. 320, 1996, pp. 19–51]. However, the data reported also indicate the presence of a weak net intercomponent energy transfer from the boundary-normal velocity component to the boundary-tangential velocity components over a thin region outside the viscous sublayer which is not captured within existing models of intercomponent energy transfer at the boundary.

4.1 Introduction

Developing an understanding of the nature of the interaction of zero-mean-shear turbulence with an impermeable boundary has proven to be a challenging problem, which has been useful in, for example, the development of turbulent models (Perot and Moin, 1995b). This problem is of fundamental interest as it enables the direct inhibiting effects of boundaries on turbulent fluctuations to be isolated from indirect effects of the boundary (relating to the production of turbulent kinetic energy). However, despite the apparent simplified nature of this interaction, the nature of the intercomponent energy transfer that occurs within the boundary-affected region of the flow has proven to be a controversial topic (see, for example, Hunt and Graham, 1978; Perot and Moin, 1995a; Bodart et al., 2010).

It is thought that the initial adjustment of a zero-mean-shear turbulent flow to the introduction of an impermeable boundary is well described by the rapid distortion theory (RDT) proposed by Hunt and Graham (1978). That is, the no-penetration condition imposed by the boundary results in a monotonic reduction in the magnitude of the boundary-normal root-mean-square (rms) turbulent velocity component, $w \equiv \overline{(u_3')^2}^{1/2}$, from its expected value in the absence of a boundary over a distance of approximately one integral length scale. In order to preserve continuity, suddenly imposing the wall-blocking condition ($w = 0$) results in pressure increases and redistribution of turbulent kinetic energy; a net transfer of energy occurs from the boundary-normal turbulent velocity component (w) to the boundary-tangential turbulent velocity components ($u \equiv \overline{(u_1')^2}^{1/2}$). This results in amplified values of u within the boundary-affected region, relative to its expected value in the absence of a boundary.

However, the subsequent development of the flow and its structure in studies in which a statistically stationary state is reached remains unclear. Results from a range of experimental and simulation based studies, conducted in both otherwise homogeneous (see, for example, Aronson et al., 1997; Perot and Moin, 1995a) and inhomogeneous turbulence (see, for example, Hannoun et al., 1988; McCorquodale and Munro, 2017a)¶, indicate that w remains inhibited by the boundary in accordance with the RDT proposed by Hunt and Graham (1978). However, controversy has arisen regarding whether the blocking of w continues to give rise to an intercomponent energy transfer from w^2 to u^2 through a correlation between the fluctuating pressure and velocity-strain fields, described by the so-called pressure-strain term Π_{ij}^s of the Reynolds stress transport equations. That is, measurements of the pressure-strain term Π_{ij}^s (in both developing and statistically stationary flow) indicate that an intercomponent energy transfer from w^2 to u^2 is significant over a thin layer, typically approximately equal in thickness to the viscous sublayer, immediately adjacent to the boundary (Perot and Moin, 1995a; Bodart et al., 2010; McCorquodale and Munro, 2017a)¶ but the physical interpretation of these measurements remain under dispute. That is, studies remain divided regarding whether the intercomponent energy transfer is primarily governed by dynamic viscous effects (Perot and Moin, 1995a) or by the kinematic blocking of the boundary (Hunt and Graham, 1978; Hunt, 1984; Magnaudet, 2003).

Regarding the first mechanism, Perot and Moin (1995a) used DNS to study the effect of inserting an impermeable boundary on an otherwise isotropic and homogeneous turbulent flow and reported that, following the development of a flow to the initial insertion of the boundary, u was approximately constant within the boundary-affected region except within the viscous sublayer. Similar results for u have also been reported in a range of other studies of zero-mean-shear turbulence interacting with a boundary (see, for example, Uzkan and Reynolds, 1967; Aronson et al., 1997; Bodart et al., 2010).

¶N.B. McCorquodale and Munro (2017a) is shown in chapter 3

To explain these results Perot and Moin (1995a) proposed a physical model in the context of "splats" and "antisplats". Here the term "splats" refers to boundary-incident turbulent motions that are blocked by the boundary; these blocking events result in high instantaneous dynamic pressure and a corresponding transfer of energy from the boundary-normal velocity component u_3' to the boundary-tangential velocity components u_1' and u_2' (Perot and Moin, 1995a). The collision of fluid elements travelling tangential to the boundary was proposed to give rise to similar events, so-called "antisplats" in which the collision of elements again results in high instantaneous dynamic pressure and a transfer of energy from u_1' and u_2' to u_3' as the fluid elements eject from the boundary. Perot and Moin (1995a) proposed that the energy transfer described by the pressure-strain term Π_{ij}^s did not describe a net transfer of energy, but rather was a measure of the imbalance in the energy associated with "splats" and "antisplats", due to the viscous dissipation of turbulent kinetic energy (TKE) from fluid elements close to the boundary. That is, the dissipation of TKE was thought to result in antisplats that were, on average, less energetic than splats, thereby giving rise to a non-zero averaged pressure-strain term (Perot and Moin, 1995a) but which does not result in amplified values of u within the boundary-affected region.

However several studies have reported that u was actually amplified in the boundary-affected region relative to values expected in the absence of the boundary (see, for example, Biringen and Reynolds, 1981; Thomas and Hancock, 1977), which has led to an alternative interpretation of the measurements of Π_{ij}^s in which it is thought that a net transfer of energy from w^2 to u^2 occurs in the boundary-affected region. Note that this interpretation is in qualitative accordance with RDT (Hunt and Graham, 1978) in which, recall, the kinematic blocking condition governs the interaction. Note, however, that in RDT the proposed amplification of u is conditional on the assumption that viscous effects were confined to a viscous sublayer which was small compared to the integral length scale of the turbulence (*i.e.* that the Reynolds number is very high) such that viscous effects could be neglected. This assumption implies that the theory may be valid only for short times over which the turbulence does not decay significantly. As a result, the validity of RDT to describe the subsequent development of the flow after boundary insertion has been questioned (Perot and Moin, 1995a; Aronson et al., 1997). Nonetheless, it has been proposed that RDT remains valid to describe the development of zero-mean-shear turbulence at an impermeable boundary at sufficiently high Reynolds number (Magnaudet, 2003).

More recently Bodart et al. (2010) proposed that the intercomponent energy transfer described by Π_{ij}^s was indeed a net transfer of energy but which only occurs in flows with large skewness ($\overline{u_3'u_3'u_3'}/w^3$) of the turbulent velocity field. However, they were unable to provide a physical model to support their assertion that a net intercomponent energy transfer occurred. Indeed, their measured values of u exhibited a monotonic reduction in

the boundary-affected region - consistent with the results of Perot and Moin (1995a), in which, we recall, it was argued that no net intercomponent energy transfer occurred.

Further from the boundary (outside the viscous sublayer but within the boundary-affected region) the sign of Π_{ij}^s is reported to reverse and an intercomponent energy transfer from energy-rich u^2 components to the energy-poor w^2 component has been reported to occur (Perot and Moin, 1995a; Bodart et al., 2010; Walker et al., 1996; McCorquodale and Munro, 2017a)¶. Walker et al. (1996) proposed that this so-called "return-to-isotropy" intercomponent energy transfer results from anisotropy induced from the kinematic blocking condition acting on u_3'. (Note that here the term "return-to-isotropy" is used specifically to refer to the energy transfer from u^2 to w^2, in a region in which $u > w$, and does not refer to a temporal evolution in statistics.)

In light of its statistical properties, oscillating-grid turbulence (OGT) has also been used to study the interaction of approximately zero-mean-shear turbulence at a boundary. In these studies u has typically been found to be amplified in the boundary-affected region (see for example Hannoun et al., 1988; Kit et al., 1997; Brumley and Jirka, 1987; McCorquodale and Munro, 2017a)¶ in qualitative agreement with the RDT predictions (Hunt and Graham, 1978; Hunt, 1984). However, in a recent study (McCorquodale and Munro, 2017a)¶ the current authors presented measurements of the terms of transport equation of TKE, which attributed the observed increase in u^2 primarily to the effects of turbulent transport, rather than intercomponent energy transfer. McCorquodale and Munro (2017a)¶ attributed the observed near-wall peak of Π_{ij}^s, over a thin region approximately equal in thickness to the viscous sublayer, to a viscous effect (Perot and Moin, 1995a) and consequently concluded that a net energy transfer from w^2 to u^2 (if any occurred) was not a prominent mechanism in determining the spatial structure of u in the boundary-affected region of this flow. McCorquodale and Munro (2017a)¶ further concluded that the 'return-to-isotropy' intercomponent energy transfer was not independent of the effects of turbulent transport and that boundary-normal inhomogeneity outside the boundary-affected region could promote a stronger 'return-to-isotropy' intercomponent energy transfer within the boundary-affected region, consistent with key elements of a related model of the intercomponent energy transfer derived by Magnaudet (2003).

However, analysis of ongoing experiments to study the interaction of OGT with a permeable boundary (not reported here) indicates the presence of a weak net intercomponent energy transfer mechanism from w^2 to u^2 in a thin region just outside the viscous sublayer. The need to document and interpret this new observation has provided the motivation for the current paper, in which we report new results from experiments studying the interaction between OGT and a solid boundary to cast new light specifically on intercomponent energy transfer within the boundary-affected region

¶N.B. McCorquodale and Munro (2017a) is shown in chapter 3

of approximately zero-mean-shear turbulence at a solid boundary. In section 4.2 we describe the experimental set-up and the techniques used to measure the flow. In section 4.3 we present estimates of the pressure-strain term describing intercomponent energy transfer. In section 4.4 we present measurements of the energy spectra which provide evidence of the nature of the intercomponent energy transfer described in section 4.3. In section 4.5 we present results of a statistical analysis of splats and antisplats which provides further evidence of the nature of the intercomponent energy transfer observed. Discussions and conclusions are made in section 4.6.

4.2 Experiments

A schematic view of the experimental set-up is shown in figure 4.1. We stress that the apparatus is identical to those used in the recent related study by McCorquodale and Munro (2017a)¶, to which we refer the reader for a detailed description. For clarity, we provide here a brief summary of pertinent aspects of the apparatus.

The experiments were conducted in a transparent acrylic box with internal dimensions 35.2 cm × 35.2 cm × 48 cm, henceforth denoted the 'outer box' (see figure 4.1), which was filled with a salt-water solution of uniform density $\rho = 1.028\,\mathrm{g/cm^3}$. An open-ended inner box, constructed from 0.5 cm thick transparent acrylic with internal dimensions 24.5 cm × 24.5 cm × 26.5 cm, was fixed centrally on-plan at the base of the tank, as shown in figure 4.1(b), which was used to systematically reduce the mean flow present within the turbulence produced, as described in detail by McCorquodale and Munro (2017b)*. We will henceforth let $2L = 24.5\,\mathrm{cm}$ denote the internal width of the inner box. The grid was suspended inside the outer box with its plane horizontal and positioned so that when at the bottom of its stroke it was 1 cm above the top of the inner box (see figure 4.1a). The grid was of stainless steel construction and consisted of an array of 7 × 7 bars, with square cross-section of 1 cm width, mesh spacing $M = 5\,\mathrm{cm}$ and corresponding solidity of 36.4%. A solid false-floor plate, spanning the interior of the inner tank, was inserted parallel to the grid and at a depth $H \approx 4.2M$ below the grid's mean position (see figure 4.1a).

Here, we report results from five sets of experiments, in which the stroke (defined as equal to the amplitude of the grid's motion) S was varied between 2.5 cm and 3.0 cm and the frequency of the grid's oscillation f between 1.6 Hz and 5.4 Hz. The corresponding grid Reynolds numbers for these five experiments were $Re_G \equiv MSf/\nu \approx 2020$, 4220, 5260, 6480 and 8100. Further increases in Re_G were not possible; proportionately more intense mean flows (in comparison to the magnitude of the fluctuations) are known to arise at higher grid oscillation frequency (McDougall, 1979), such that turbulence produced is a poor approximation to zero-mean-shear turbulence. For each of the

¶N.B. McCorquodale and Munro (2017a) is shown in chapter 3

*N.B. McCorquodale and Munro (2017b) is shown in chapter 2

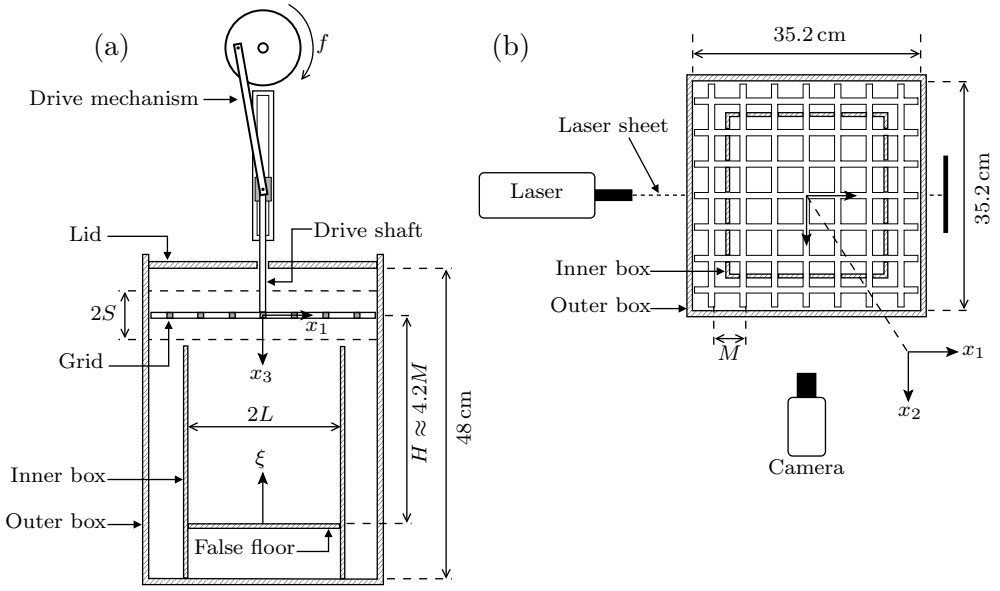


Figure 4.1: Sketches showing the key components of the experimental set-up. (a) A side view showing the positioning of the reciprocating drive mechanism, the horizontal grid, the false floor and the inner and outer boxes. (b) A plan view showing the position of the inner box relative to the grid's mesh, and the position of the camera relative to the vertical laser-sheet. Also shown are the coordinate directions (x_1, x_2, x_3), and the vertical height normal to the false floor, denoted $\xi = H - x_3$.

five grid Reynolds numbers, the experiments were repeated, under nominally identical conditions, a total of 5 times. We note that the measurements from the experiments reported at $Re_G \approx 2020$ and 4220 formed part of the data-set previously reported by McCorquodale and Munro (2017a)[¶], whereas the measurements from the experiments at $Re_G \approx 5260, 6480$ and 8100 have not previously been reported.

Measurements of instantaneous fluid velocities were obtained using the same technique described in McCorquodale and Munro (2017a)[¶]. Two-dimensional particle imaging velocimetry (PIV) was applied to the vertical plane through the centre of the grid, in the region inside the inner box spanned by the grid and the false-floor. PIV calculations were performed using square interrogation windows of 13×13 pixels, overlapped to achieve 8 pixel spacing between velocity vectors, resulting in a physical spacing between velocity vectors of approximately 0.2 cm. OGT is statistically stationary and so the statistical properties of the flow were analysed using time averages; analysis of the data showed that the time-averaged mean and rms velocity components were well converged over an averaging period of 4 min.

The velocity data were calculated and analysed relative to the right-handed coordinate system (x_1, x_2, x_3); here, x_3 denotes vertical depth below the mid-height of the grid's oscillation, and (x_1, x_2) are the horizontal coordinates relative to the center of the

[¶]N.B. McCorquodale and Munro (2017a) is shown in chapter 3

grid (see figure 4.1). The corresponding velocity components are denoted (u_1, u_2, u_3); the two components measured using the PIV set-up described above are $u_1(x_1, x_3, t)$ and $u_3(x_1, x_3, t)$, in the central plane at $x_2 = 0$. We use the conventional Reynolds decomposition $u_i = U_i + u_i'$, where $u_i'(\mathbf{x}, t)$ denote the fluctuating components and $U_i(\mathbf{x}) = \overline{u_i}$ the time-averaged mean components (the overbar notation is used throughout to denote time averaging). We also introduce the coordinate $\xi = H - x_3$, which denotes vertical height above the false floor (see figure 4.1a). This coordinate is used only for convenience when plotting and comparing data; we stress that all velocities (and derivatives of velocities) were calculated in terms of the right-handed coordinates (x_1, x_2, x_3).

In the absence of the false-floor, and away from the inner-box sidewalls, the turbulence produced by the oscillating grid was found to be in good agreement with standard models of OGT (see, for example, Hopfinger and Toly, 1976; Fernando and De Silva, 1993). That is, with this apparatus the turbulence produced is statistically stationary, approximately homogeneous and isotropic on horizontal planes across a central region of the tank ($|x_1/L| \leq 1/2$) and decays spatially with distance below the grid (McCorquodale and Munro, 2017b)*. Outside the central region of the tank $|x_1/L| \geq 1/2$ anisotropic side wall regions exist, which are described in detail by McCorquodale and Munro (2017b)*. Hence throughout this paper our attention is focused on the central region given by $|x_1/L| \leq 1/2$; the side wall anisotropic regions are ignored in the calculation of turbulent statistics. McCorquodale and Munro (2017a)¶ showed that, with the false-floor installed results indicate that the boundary induced effects are mostly confined to a layer of height δ_s (of the order of the integral length scale of the turbulence) above the boundary. Data describing the statistical structure of the mean and turbulent components of the flow, both within the boundary-affected region (*i.e.* $\xi < \delta_s$) and above the boundary-affected region (*i.e.* $\xi > \delta_s$), were in good agreement with the results reported previously by McCorquodale and Munro (2017a)¶, to which we refer the reader for detailed illustrations of the statistical structure of the flow.

4.3 Estimates of the pressure-strain correlation

In section 4.1 we noted that intercomponent energy transfer is described by the pressure-strain correlation term (*i.e.* Π_{ij}^s in equation 4.1 below) of the Reynolds stress transport

*N.B. McCorquodale and Munro (2017b) is shown in chapter 2

¶N.B. McCorquodale and Munro (2017a) is shown in chapter 3

equation, of which the steady form may be written as (see Hinze, 1975, p. 323)

$$0 = \underbrace{-U_k \frac{\partial}{\partial x_k}\overline{u_i' u_j'}}_{A_{ij}^d} \underbrace{-\overline{u_j' u_k'}\frac{\partial U_i}{\partial x_k} - \overline{u_i' u_k'}\frac{\partial U_j}{\partial x_k}}_{\Phi_{ij}} \underbrace{-\frac{\partial}{\partial x_k}\overline{u_i' u_j' u_k'}}_{T_{ij}}$$
$$\underbrace{-\frac{1}{\rho}\left(\frac{\partial}{\partial x_i}\overline{p' u_j'} + \frac{\partial}{\partial x_j}\overline{p' u_i'}\right)}_{\Pi_{ij}^d} + \underbrace{\frac{1}{\rho}\overline{p'\left(\frac{\partial u_j'}{\partial x_i} + \frac{\partial u_i'}{\partial x_j}\right)}}_{\Pi_{ij}^s} + \underbrace{\nu\frac{\partial^2 \overline{u_i' u_j'}}{\partial x_k \partial x_k}}_{D_{ij}} \underbrace{-2\nu\overline{\frac{\partial u_i'}{\partial x_k}\frac{\partial u_j'}{\partial x_k}}}_{\varepsilon_{ij}}, \quad (4.1)$$

where A_{ij}^d and Φ_{ij} denote, respectively, transport and production due to the mean flow; T_{ij} and Π_{ij}^d denote, respectively, transport by velocity and pressure fluctuations; D_{ij} and ε_{ij} denote molecular diffusion and viscous dissipation. Estimates of the terms of (4.1) for the interaction of OGT with an impermeable boundary were recently reported by the current authors (McCorquodale and Munro, 2017a)¶. In this section we briefly revisit these previous estimates of Π_{ij}^s reported by McCorquodale and Munro (2017a)¶ (the same experiments reported here at $Re_G \approx 2020$ and 4220) and highlight key aspects of the results pertinent to the current work.

Within the inner box's central region—the region of interest—the turbulence is approximately homogeneous on horizontal planes and so $\overline{u_i' u_j'} \approx 0$ for $i \neq j$. In addition, given the redistributive nature of the pressure-strain correlation term ($\Pi_{ii}^s = 0$), since the turbulence is approximately homogeneous on horizontal planes we can assume $2\Pi_{11}^s \approx 2\Pi_{22}^s \approx -\Pi_{33}^s$. Hence, an understanding of the pressure-strain correlation term Π_{ij}^s can be reached by considering only the transport equation for the Reynolds stress $\overline{u_1' u_1'} = u^2$. Noting that in turbulence that is approximately homogeneous on horizontal planes $\Pi_{11}^d \approx 0$, then the transport equation for u^2 can be expressed as

$$0 = \underbrace{-U_k \frac{\partial}{\partial x_k}\overline{u_1' u_1'}}_{A_{11}^d} \underbrace{-2\overline{u_1' u_k'}\frac{\partial U_1}{\partial x_k}}_{\Phi_{11}} \underbrace{-\frac{\partial}{\partial x_k}\overline{u_1' u_1' u_k'}}_{T_{11}} + \underbrace{\frac{2}{\rho}\overline{p'\frac{\partial u_1'}{\partial x_1}}}_{\Pi_{11}^s} + \underbrace{\nu\frac{\partial^2 \overline{u_1' u_1'}}{\partial x_k \partial x_k}}_{D_{11}} \underbrace{-2\nu\overline{\frac{\partial u_1'}{\partial x_k}\frac{\partial u_1'}{\partial x_k}}}_{\varepsilon_{11}}. \quad (4.2)$$

We stress that a direct evaluation of Π_{ij}^s, or the other terms of (4.2), is not possible for the current experiments, requiring instantaneous measurements of pressure fluctuations and of all three velocity components. However, a number of simplifying assumptions can be made to allow estimation of the terms not involving pressure fluctuations. Π_{11}^s can then be estimated from a balance of the remaining terms in (4.2); an approach also used previously by Aronson et al. (1997). The simplifying assumptions necessary for this approach include: (i) the time-averaged statistical properties of the flow are assumed to be symmetric in the x_1- and x_2-directions (based on the symmetry of the experimental set-up). (ii) The turbulence is assumed to be approximately homogeneous in horizontal planes. (iii) The approximation $\overline{(\partial u_1'/\partial x_2)^2} \approx 2\overline{(\partial u_1'/\partial x_1)^2}$ can be used in calculation of

¶N.B. McCorquodale and Munro (2017a) is shown in chapter 3

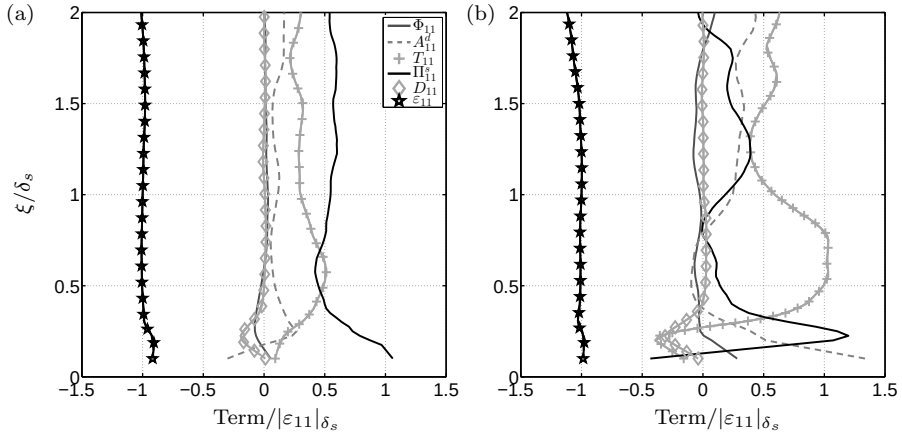


Figure 4.2: Measurements of terms in the transport equation (4.2) at different Reynolds numbers - (a)$Re_G = 2020$ and (b)$Re_G = 4220$. Different symbols have been used to denote each term, which are shown in the legend. Each term has been spatially averaged in the x_1-direction (*i.e.* $\langle\cdot\rangle_1$), and has been normalised by the magnitude of the dissipation evaluated at the edge of the boundary-affected region, $|\varepsilon_{11}|_{\delta_s}$.

the dissipation terms—a relationship which is known to hold for homogeneous, isotropic turbulence (see Pope, 2000, p. 134). Note that when evaluating the velocity derivatives, the no slip and impermeability conditions ($u_i = 0$) were applied at $\xi = 0$.

Estimates of the terms of (4.2) produced using the scheme outlined above are shown in figure 4.2, for experiments conducted at $Re_G \approx 2020$ and 4220 (first reported in McCorquodale and Munro, 2017a)[¶], plotted against scaled height ξ/δ_s. The scheme outlined above inevitably produced scatter in the results so, in an effort to reduce scatter, the data were averaged in the x_1-direction over the central region of the inner box's width (we henceforth denote this averaging by $\langle\cdot\rangle_1$) and also averaged over the 5 repeat experiments conducted under each condition. To facilitate comparison, the data have been normalised by the magnitude of the corresponding component of energy dissipation evaluated at the height $\xi = \delta_s$, denoted $|\varepsilon_{11}|_{\delta_s}$. We note that we were unable to obtain reliable estimates of the terms of (4.2) for experiments conducted at $Re_G \approx 5260$, 6480 and 8100 due to limitations inherent within our 2D PIV measurements. That is, the limited resolution of the PIV used (a resolution of approximately 0.2 cm) was insufficient to capture all scales of turbulent motion and led to underestimation of some terms (primarily the dissipation ε_{11} term) in equation (4.2). Since the pressure-strain term Π^s_{ij} is determined from a balance of the remaining terms in (4.2) this limitation gives rise to unreliable estimates of Π^s_{ij} for these experiments and, as a consequence, results for these experiments are not shown here.

Figure 4.2 indicates that, within the boundary-effected region, Π^s_{11} initially undergoes a gradual and slight reduction over the region $0.6 \lesssim \xi/\delta_s \leq 1$, a slight (positive) increase over the region $0.3 \lesssim \xi/\delta_s \lesssim 0.6$ and a sharp increase to a near-wall (positive) peak

[¶]N.B. McCorquodale and Munro (2017a) is shown in chapter 3

value over the region $\xi/\delta_s \lesssim 0.3$. Note that the sharp increase in Π_{11}^s over the region $\xi/\delta_s \lesssim 0.3$ occurs over a region of thickness approximately equal to the viscous sublayer (McCorquodale and Munro, 2017a)¶. We stress that similar features of Π_{11}^s are evident in the measurements of the studies by Perot and Moin (1995a), Aronson et al. (1997) and Bodart et al. (2010).

The initial reduction of Π_{11}^s at the edge of the boundary-affected region shown in figure 4.2 has previously been attributed to a return-to-isotropy intercomponent energy transfer (Walker et al., 1996; McCorquodale and Munro, 2017a)¶, whilst the sharp increase in Π_{11}^s over a region approximately equal in thickness to the viscous sublayer has previously been attributed to the viscous effects resulting in splat-antisplat disequilibrium (Perot and Moin, 1995a; McCorquodale and Munro, 2017a)¶. However, the cause of the initial increase in Π_{11}^s over the region $0.3 \lesssim \xi/\delta_s \lesssim 0.6$ does not appear consistent with either of these mechanisms and, as far as we are aware, has not previously received comment. Note that in previous studies of the interaction of zero-mean-shear turbulence with an impermeable boundary (Perot and Moin, 1995a; Bodart et al., 2010), the initial increases in the pressure-strain term Π_{11}^s occur in regions in which viscous dissipation is not enhanced and rather the increase in Π_{11}^s is offset by transport terms (as in figure 4.2). Consequently, this intermediate region, over which the data indicate a weak intercomponent energy transfer may occur from the boundary-normal to the boundary-tangential velocity component, is the focus of the analysis here; the interpretation of Π_{11}^s over this region is explored in sections 4.4 and 4.5.

4.4 Energy spectra

In previous studies of OGT interacting with a boundary, spectra have been used to gain insight into intercomponent energy transfer (Hannoun et al., 1988; Kit et al., 1997; Brumley and Jirka, 1987), and have been compared against the spectral estimates derived from RDT (Hunt and Graham, 1978). The energy spectra for the vertical velocity fluctuations $E_w(f_E)$ and for the horizontal velocity fluctuations $E_u(f_E)$ at different distances ξ/δ_s away from the plate are shown in figure 4.3 for a representative subset of the experiments. Here f_E denotes the spectral frequency. The estimates of the energy spectra have been normalised by the square of the magnitude of the corresponding rms turbulent velocity component at the edge of the boundary-affected region, denoted $w_{\delta_s}^2$ or $u_{\delta_s}^2$, and by the grid oscillation frequency f. We stress that in this flow Taylor's frozen turbulence hypothesis cannot be invoked to estimate the corresponding wavenumber spectra and that the spatial resolution of the PIV data in the x_1-direction is not sufficient to directly compute a complete wavenumber spectra. As a result, a direct analysis of the spatial scales over which the energy spectra are influenced by the boundary is not

¶N.B. McCorquodale and Munro (2017a) is shown in chapter 3

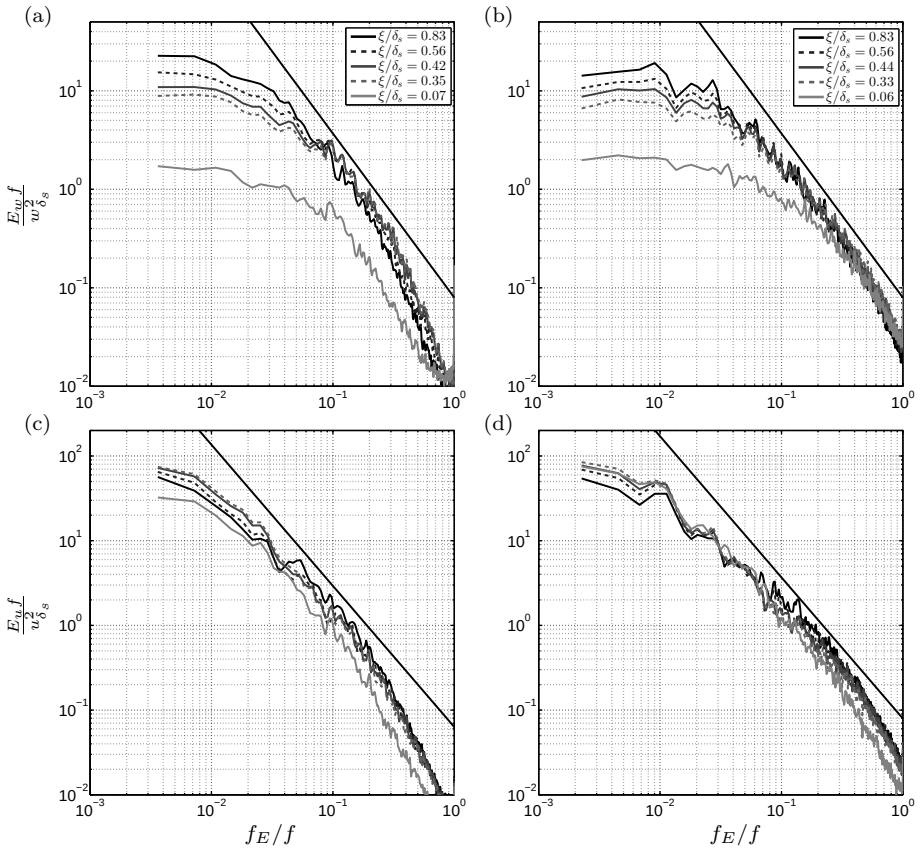


Figure 4.3: Measurements of the energy spectra for (a,b) the vertical velocity fluctuations E_w and (c,d) for the horizontal velocity fluctuations E_u against spectral frequency f_E for different distances above the boundary ξ/δ_s [see legends in (a,b) which also apply to (c,d) respectively]. Data has been normalised by the grid oscillation frequency f and the magnitude of corresponding rms turbulent velocity component at the edge of the boundary-affected region, denoted $w^2_{\delta_s}$ and $u^2_{\delta_s}$. Representative results from a subset of experiments are shown; data shown in (a,c) correspond to experiments conducted at $Re_G = 4220$ and (b,d) correspond to experiments conducted at $Re_G = 8100$.

possible, nor is a quantitative comparison to the spectral estimates derived from RDT (Hunt and Graham, 1978). Rather, in this section we are constrained to analysis within the frequency domain, from which we loosely infer results relating to the size of affected turbulent motions.

Consistent with previous work (Hannoun et al., 1988; Kit et al., 1997; Brumley and Jirka, 1987; Hunt and Graham, 1978), estimates of E_w shown in figure 4.3(a,b) are inhibited at small frequencies (large scales) and depart from a $-5/3$ decay as the boundary is approached ($\xi/\delta_s \to 0$). [A $-5/3$ decay is consistent with an inertial subrange in zero-mean turbulent flow and has previously been reported in OGT (Hannoun et al., 1988)]. As ξ/δ_s reduces (see figure legend), progressively larger frequencies (smaller scales) are shown to be inhibited in qualitative agreement with the spectral estimates derived from RDT (Hunt and Graham, 1978), consistent with the blocking effect of the

boundary.

In contrast, estimates of E_u shown in figure 4.3(c,d) exhibit only very slight increases at small frequencies (large scales) as the boundary is approached (*i.e* as ξ/δ_s reduces), except within a thin region close to the boundary approximately equal in thickness to the viscous sublayer (*i.e.* over the region $\xi/\delta_s \lesssim 0.3$) within which E_u diminishes as the boundary is approached as a result of the increased dissipation of TKE. (This is particularly evident in figure 4.3c.) The increase in E_u at small frequencies as the boundary is approached is in qualitative accordance with previously reported measurements from OGT (Brumley and Jirka, 1987; Hannoun et al., 1988; Kit et al., 1997), although we note that the observed increase in E_u is significantly smaller than that reported by Hannoun et al. (1988) for which the cause is currently unclear. This increase in E_u at small frequencies or large scales has previously been interpreted as evidence of net intercomponent energy transfer from w^2 to u^2 at large spatial scales, sufficient to give rise to an amplification of u^2 with the boundary-affected region (Hannoun et al., 1988; Kit et al., 1997; Brumley and Jirka, 1987; Hunt and Graham, 1978). In particular, amplification of the E_u spectra at small wavenumbers has been attributed to effects of turbulent eddies impinging onto a boundary (*i.e.* splats), whereby they flatten at the boundary and transfer the energy of the vertical component to the horizontal components, and to the non-linear effects of vortex stretching at the boundary which act to increase E_u at large spatial scales (Kit et al., 1997). Note however that figure 4.3 shows that the affect of the boundary on E_u at small frequency is significantly smaller than the affect on E_w. Importantly, this indicates that the observed intercomponent energy transfer is not a traceless transfer of energy between the velocity components, and may only give rise to a weak amplification of u^2 within the boundary-affected region (as per, for example, Perot and Moin, 1995a; Aronson et al., 1997). That is, we stress that the principal mechanism reported to give rise to an amplification of u^2 within the boundary-affected region of OGT has been the blocking of a far-field TKE flux (McCorquodale and Munro, 2017a)[¶]. Regardless, the measurements of the energy spectra are consistent with the estimates of the pressure-strain correlation term presented in section 4.3, indicating the presence of a weak net intercomponent energy transfer from the boundary-normal to the boundary-tangential velocity component outside the viscous sublayer.

4.5 Quadrant analysis

In section 4.1 we noted that intercomponent energy transfer described by the pressure-strain correlation term Π^s_{ij} is thought to manifest within the boundary-affected region as an imbalance in the energy associated with splats and antisplats (see for example Perot and Moin, 1995a; Bodart et al., 2010). In this section we aim to better understand

[¶]N.B. McCorquodale and Munro (2017a) is shown in chapter 3

intercomponent energy transfer by use of a statistical approach to identify and isolate events within the turbulent flow that exhibit characteristics expected of splats and antisplats. That is, the stagnation flow associated with splats and antisplats is thought to exhibit strongly decelerating flow and in section 4.5.1 we use this feature as a criteria to identify splats and antisplats. In section 4.5.2, conditional turbulent statistics associated with splats and antisplats are evaluated, where the conditions derived in section 4.5.1 are used as sampling conditions.

4.5.1 A criteria for isolating splats and antisplats

Splats and antisplats are fluid elements that exhibit strong vertically decelerating flow (*i.e.* large spatial gradients in u_3'); splat events moving towards the boundary ($u_3' > 0$) yield negative values of the vertical strain rate $\partial u_3'/\partial x_3$ and antisplat events moving away from the boundary ($u_3' < 0$) yield positive values of the vertical strain rate $\partial u_3'/\partial x_3$ (Perot and Moin, 1995a; Bodart et al., 2010; Magnaudet, 2003). However, fluid elements that exhibit these statistical characteristics exist throughout the entire flow, as a consequence of the random structure of a turbulent flow. On the other hand, the blocking associated with the formation of splats and antisplats is expected to give rise to more strongly decelerating flow than observed in the bulk interior of the flow. Thus, it is our premise that splats and antisplats may be isolated from the background flow by use of a threshold or critical value on the magnitude of the vertical strain rate $\partial u_3'/\partial x_3$. In the analysis that follows we define this threshold value in comparison to an average reference value of the strain rate given by $w/\overline{\ell}_w$, where $\overline{\ell}_w$ denotes the time-averaged transverse integral length scale of the boundary-normal velocity component u_3'. This reference strain rate is devised from an order of magnitude analysis (as per Bodart et al., 2010); when a fluid packet of size ℓ meets the boundary with velocity u_3' the vertical strain rate can be estimated as u_3'/ℓ. For a given point within the boundary-affected region the average velocity and size of a fluid packet is given by w and $\overline{\ell}_w$ respectively; as a boundary is approached one expects the remaining fluid packets to gradually reduce in size and, consistent with this concept, $\overline{\ell}_w$ monotonically reduces within the boundary-affected region as a result of the blocking effect of the boundary (see for example McCorquodale and Munro, 2017a)[¶]. Thus we expect a measure of the average strain rate observed within the boundary-affected region to scale with $w/\overline{\ell}_w$. The reference strain rate also retains an appropriate physical interpretation outside the boundary-affected region; on average we expect the vertical strain rate of the fluid packet to scale with the average packet velocity, w, and inversely scale with the packet size, $\overline{\ell}_w$. For reference, we note that outside the boundary-affected region $\overline{\ell}_w$ is approximately constant and w monotonically reduces as the boundary is approached (see McCorquodale and Munro, 2017a)[¶].

To validate this premise we determine typical values (ranges of high probability) of

[¶]N.B. McCorquodale and Munro (2017a) is shown in chapter 3

$|(\overline{\ell}_w/w)\partial u_3'/\partial x_3|$ within the bulk interior of the flow and illustrate that the blocking effect of the boundary gives rise to larger values of $|(\overline{\ell}_w/w)\partial u_3'/\partial x_3|$ in the boundary-affected region in comparison to those observed in the bulk interior of the flow; we interpret these measurements of strongly decelerating flow to the formation of splats and antisplats. To distinguish between splats and antisplats, we further consider measurements split into 4 quadrants based upon the sign of u_3' and $\partial u_3'/\partial x_3$. That is, we calculate:

$$\text{Quadrant 1}\,(Q_1) : \mathrm{P}_{Q_1} \equiv \left\langle \mathrm{P}\left(\frac{\overline{\ell}_w}{w}\frac{\partial u_3'}{\partial x_3} > \phi_T \cap u_3' > 0\right)\right\rangle_1, \tag{4.3a}$$

$$\text{Quadrant 2}\,(Q_2) : \mathrm{P}_{Q_2} \equiv \left\langle \mathrm{P}\left(\frac{\overline{\ell}_w}{w}\frac{\partial u_3'}{\partial x_3} > \phi_T \cap u_3' < 0\right)\right\rangle_1, \tag{4.3b}$$

$$\text{Quadrant 3}\,(Q_3) : \mathrm{P}_{Q_3} \equiv \left\langle \mathrm{P}\left(\frac{\overline{\ell}_w}{w}\frac{\partial u_3'}{\partial x_3} < -\phi_T \cap u_3' < 0\right)\right\rangle_1, \tag{4.3c}$$

$$\text{Quadrant 4}\,(Q_4) : \mathrm{P}_{Q_4} \equiv \left\langle \mathrm{P}\left(\frac{\overline{\ell}_w}{w}\frac{\partial u_3'}{\partial x_3} < -\phi_T \cap u_3' > 0\right)\right\rangle_1, \tag{4.3d}$$

as a function of ξ/δ_s, where $\mathrm{P}(A \cap B)$ denotes the probability of A and B. Recall, $\langle\cdot\rangle_1$ denotes a spatial average in the x_1-direction over the central region $|x_1/L| \leq 1/2$. In equation (4.3) ϕ_T denotes a (positive) constant that is gradually increased from 0 to determine characteristic (high probability) ranges of $(\overline{\ell}_w/w)\partial u_3'/\partial x_3$. That is, when $\phi_T = 0$ we consider the probability of each quadrant based upon every measurement of the flow field, but as ϕ_T increases the evaluated probabilities associated with each quadrant decrease (*i.e.* $\mathrm{P}(\phi_T = 0) > \mathrm{P}(\phi_T > 0)$) because those events that exhibit $|(\overline{\ell}_w/w)\partial u_3'/\partial x_3| < \phi_T$ are excluded from the analysis. A range of values of ϕ_T have been considered but for clarity we report here only $\phi_T = 0, 2$ and 6, which are sufficient to illustrate the key aspects of the analysis. We stress that previous work has indicated that splats and antisplats correspond to fluid elements in quadrants Q_4 and Q_2 respectively (Bodart et al., 2010; Perot and Moin, 1995a; Magnaudet, 2003), therefore subsequently we consider only these quadrants. Results are shown in figure 4.4, plotted against scaled height ξ/δ_s.

Outside of the boundary-affected region, turbulent motions do not directly feel the inhibiting effects of the boundary, so spatial gradients of u_3' arise only from random turbulent structure. Consequently, over this region (*i.e.* $\xi/\delta_s \geq 1$) the overall probability (*i.e.* evaluated by considering every measurement of the flow field, using the condition $\phi_T = 0$) of each quadrant is approximately constant with a value in the range 0.2-0.3, shown in figure 4.4. The probability that the normalised strain rate $(\overline{\ell}_w/w)\partial u_3'/\partial x_3$ exceeds 2 is small (approximately 0.07), therefore figure 4.4 indicates that in this region the magnitude of the normalised strain rate typically lies between 0 and 2. In addition, the probability that the normalised strain rate exceeds 6 is negligible. Thus we conclude that imposing the condition $|(\overline{\ell}_w/w)\partial u_3'/\partial x_3| \geq 6$ appears to be sufficient to remove the background turbulent fluctuations that do not feel the inhibiting effects of the boundary.

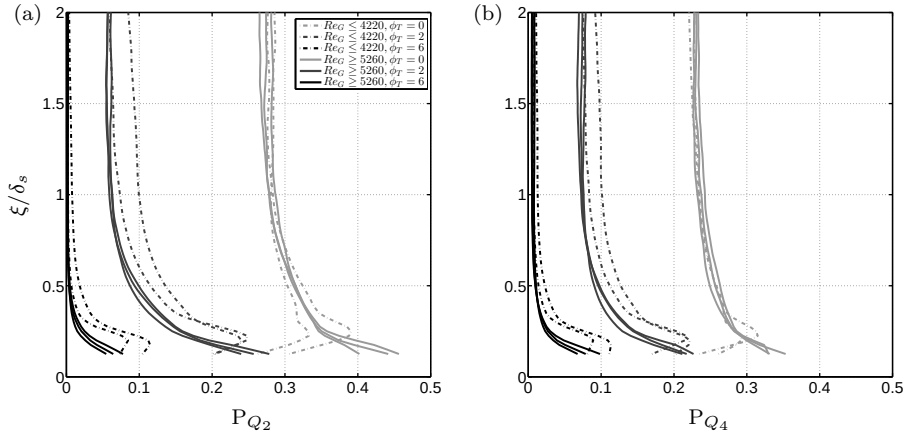


Figure 4.4: Measurements of the probability (described by (4.3)) that the normalised strain rate $(\overline{\ell}_w/w)\partial u_3'/\partial x_3$ surpasses a given constant ϕ_T [for values of ϕ_T see legend in (a) which applies to both plots], against scaled height above the boundary ξ/δ_s. In (a) the data is subject to the additional conditions $u_3' < 0$ and $\partial u_3'/\partial x_3 > 0$, in (b) the data is subject to the additional conditions $u_3' > 0$ and $\partial u_3'/\partial x_3 < 0$. Results from experiments at the 5 different experimental conditions are shown and are plotted differently for $Re_G \leq 4220$ and $Re_G \geq 5260$ [see legend in (a)]. Each data-set shown is an average of the measurements obtained across the 5 repeats conducted for each condition.

Within the boundary-affected region ($\xi/\delta_s < 1$), figure 4.4 shows that there is a small increase in the overall probability (*i.e.* given by $\phi_T = 0$) of events in Q_2 and Q_4 over the region $\xi/\delta_s \sim 0.6$-1. However, the observed magnitudes of $\partial u_3'/\partial x_3$ over the region $0.6 \leq \xi/\delta_s \leq 1$ are in general consistent with those observed in the bulk interior region of the flow. That is, figure 4.4 indicates that in the region $0.6 \leq \xi/\delta_s \leq 1$ the magnitude of the normalised strain rate typically still lies between 0 and 2 and the probability that an event falls within a given quadrant and that the normalised strain rate exceeds 2 is still approximately just 0.08. Crucially, the probability that the normalised strain rate exceeds 6 (*i.e.* the probability evaluated when $\phi_T = 6$) remains negligible for $0.6 \leq \xi/\delta_s \leq 1$. Thus, flow that is more strongly decelerating (*i.e.* which exhibits a larger normalised strain rate) than the flow outside the boundary-affected region (which, recall, is indicative of splats and antisplats) is not regularly observed for $0.6 \leq \xi/\delta_s \leq 1$.

However, over the region $\xi/\delta_s \lesssim 0.6$ the probability of events in Q_2 and Q_4 sharply increases and the observed magnitudes of $\partial u_3'/\partial x_3$ of events in Q_2 and Q_4 also exceed those observed in the bulk interior region of the flow. That is, figure 4.4 indicates that for $\xi/\delta_s < 0.6$ the overall probability of events in Q_2 and Q_4 (*i.e.* evaluated using the condition $\phi_T = 0$) significantly increases as the boundary is approached. However, figure 4.4 also shows that for $\xi/\delta_s < 0.6$ the probability of events in Q_2 and Q_4 when $\phi_T = 6$ also significantly increases as the boundary is approached, and that the increase in probability when $\phi_T = 6$ is approximately equal to the increase in probability when $\phi_T = 0$. Thus over the region $\xi/\delta_s < 0.6$ the increase in the probability of events in Q_2

and Q_4 is primarily driven by events which satisfy the condition $\phi_T = 6$ (*i.e.* which exhibit $|(\overline{\ell}_w/w)\partial u_3'/\partial x_3| > 6$) and therefore that exhibit larger strain rates than typically observed in the bulk interior of the flow ($\xi/\delta_s \geq 1$). We stress that here events in Q_2 and Q_4 exhibit spatial gradients which describe a reduction in the magnitude of u_3' as the boundary is approached. Hence, this increase in probability of events in Q_2 and Q_4 within the boundary-affected region (which also exhibit large normalised strain rates) is attributed to the inhibiting effects of the boundaries on the turbulence (*i.e.* the formation of splats and antisplats). We attribute the increasing probability of large normalised strain rates that is observed as the boundary is approached to a greater range of spatial scales being blocked by the boundary and to the prevalence of viscous effects on the turbulence close to the boundary. Thus within the boundary-affected region measured events in Q_2 and Q_4 consist of a mix of splats, antisplats and background turbulent fluctuations. However, in light of the characteristic values of $|(\overline{\ell}_w/w)\partial u_3'/\partial x_3|$ observed in the bulk interior of the flow (*i.e.* random turbulent fluctuations are characterised by $|(\overline{\ell}_w/w)\partial u_3'/\partial x_3| < 6$), these results indicate that using the condition $\phi_T = 6$ appears to be sufficient to isolate splats and antisplats from background turbulent fluctuations.

Note also that the results shown indicate a Re_G effect; for $Re_G \leq 4220$, results, shown in figure 4.4, indicate that the same trends apply until $\xi/\delta_s \approx 0.2$, at which point the probability of events in Q_2 and Q_4 peaks and then reduces. The origin of this effect is unclear, although we conjecture that this effect may arise from a data processing issue relating to computation of the strain rates. That is, within the viscous sublayer the fluid velocities are much smaller than within the bulk of the flow, such that the uncertainty within these measurements as a proportion of the fluid velocity may be large. Thus, the error associated with these measurements may give rise to unreliable estimates of the strain rate. This effect is likely to be more prevalent at low Reynolds number as a result of the lower fluid velocities that occur in these experiments.

4.5.2 Conditional statistics

Within the boundary-affected region of the flow, intercomponent energy transfer is thought to be governed by an imbalance in the energy associated with splats and antisplats (Perot and Moin, 1995a; Bodart et al., 2010); in this section we seek to explicitly consider this imbalance by computing conditional turbulent statistics from measurements of the flow that exhibit characteristics expected of splats and antisplats. That is, we compute conditional rms values of u_1' where the criteria developed in section 4.5.1 to isolate splats and antisplats are used as conditioning events. We denote the rms values of u_1' associated with measurements of the flow indicative of splats and antisplats by u_{Q_4} and u_{Q_2} respectively. Hence, u_{Q_2} and u_{Q_4} are rms values of u_1' given that the measurements used to compute these statistics satisfy the conditions $(\overline{\ell}_w/w)\partial u_3'/\partial x_3 > \phi_T \cap u_3' < 0$ and $(\overline{\ell}_w/w)\partial u_3'/\partial x_3 < -\phi_T \cap u_3' > 0$, respectively. We note that $u_{Q_2}(\phi_T = 6)$ and

$u_{Q_4}(\phi_T = 6)$ can only be evaluated for $\xi/\delta_s \lesssim 0.6$ since measurements of the flow only exhibit $|(\overline{\ell}_w/w)\partial u_3'/\partial x_3| > 6$ (*i.e.* strongly decelerating flow indicative of splats and antisplats) for $\xi/\delta_s \lesssim 0.6$ (see section 4.5.1).

In order to determine if an imbalance in the energy of splats and antisplats was dominant in giving rise to the average statistical structure of the flow within the boundary-affected region, values of u_{Q_2} and u_{Q_4} have been computed as a function of ϕ_T. That is, conditional u_{Q_2} and u_{Q_4} statistics associated with specifically splats and antisplats have been computed using the critical value $\phi_T = 6$ (see section 4.5.1) and the results compared against conditional statistics evaluated for $\phi_T < 6$ (*i.e.* in which the effects of splats and antisplats are not isolated from the background flow). A range of values of ϕ_T have been considered but for clarity we report here only $\phi_T = 0$ and 6, which are sufficient to illustrate the effects of splats and antisplats, in comparison to the background flow, on the average statistical structure of the flow. That is, they are sufficient to illustrate that the imbalance of energy associated with splats and antisplats that is isolated when $\phi_T = 6$ is able to overcome any additional weak contribution from the random turbulent fluctuations (characterised by $|(\overline{\ell}_w/w)\partial u_3'/\partial x_3| < 6$) that are included within the conditional statistics when $\phi_T < 6$. Measurements of u_{Q_2} and u_{Q_4} are shown in figure 4.5 plotted against scaled height ξ/δ_s.

In order to illustrate boundary effects associated with splats and antisplats on the measured values of u_{Q_4} and u_{Q_2}, we first consider values of u_{Q_4} and u_{Q_2} evaluated with $\phi_T = 0$ outside the boundary-affected region (*i.e.* these are values of u_{Q_4} and u_{Q_2} associated with the background flow only). Outside the boundary-affected region (*i.e.* for $\xi/\delta_s > 1$) figures 4.5(a-c) indicate that $u_{Q_4} > u_{Q_2}$, which indicates that the energy associated with turbulent motions incident towards the boundary exceeds that of turbulent motions moving away from the boundary (recall that u_{Q_4} satisfy the condition $u_3' > 0$ and u_{Q_2} the condition $u_3' < 0$). We stress that this is simply a result of the anisotropic nature of the flow produced by OGT, whereby the magnitude of turbulent fluctuations decay with distance beneath the grid, which gives rise to a TKE flux away from the grid towards the boundary (see McCorquodale and Munro, 2017a)¶.

Figure 4.5(a-c) show that this trend diminishes at the edge of the boundary-affected region ($\xi/\delta_s \approx 0.6$ to 1.0), where we can see that u_{Q_4}/u_{Q_2} approaches a value of 1. Here this trend physically represents a change in the imbalance between the energy associated with turbulent motions incident towards the boundary, which are increasingly less energetic, relative to the energy of turbulent motions moving away from the boundary. Although this is evidently a boundary effect, it appears that this effect is not associated with splats and antisplats - recall that in section 4.5.1 we showed that the strongly decelerating flow associated with splats and antisplats occurred only over the region $\xi/\delta_s \lesssim 0.6$. Instead this observation is attributed to the effects of turbulent transport,

¶N.B. McCorquodale and Munro (2017a) is shown in chapter 3

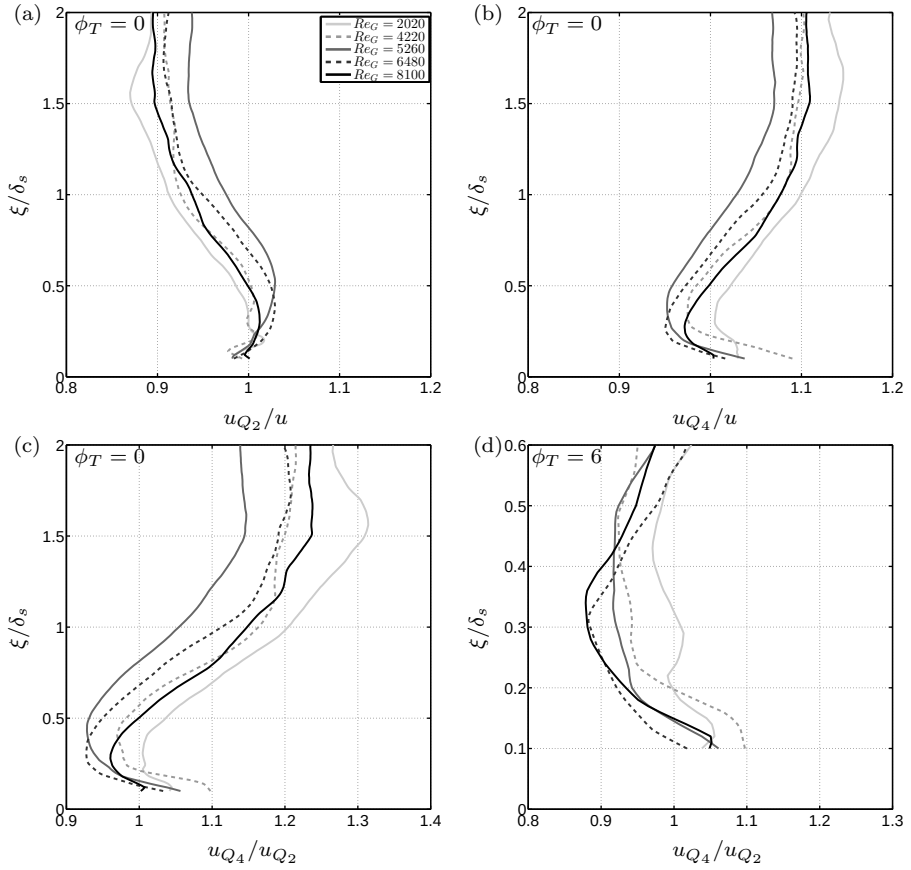


Figure 4.5: Measurements (a)$u_{Q_2}(\phi_T = 0)$ and (b)$u_{Q_4}(\phi_T = 0)$ of the conditionally sampled rms boundary-tangential velocity component plotted against scaled height above the boundary ξ/δ_s. The data has been normalised by the rms measurements of the unsampled turbulent horizontal velocity component. (c) Shows the same data normalised to allow a direct comparison between the magnitude of u_{Q_2} and u_{Q_4}. (d) Shows the same data as (c) subject to the condition $\phi_T = 6$ (note the different scales used). In each plot a single data-set is shown for each experimental condition, which is an average of the measurements obtained across the 5 repeats conducted for each condition.

due to the blocking effect of the boundary on the boundary-normal TKE flux (see McCorquodale and Munro, 2017a)[¶], which in isolation would act to result in $u_{Q_4} \approx u_{Q_2}$. That is, the TKE flux acts to transfer energy from energy-rich regions to energy-poor regions, such that, in isolation, the blocking of the TKE flux would act to give rise to constant values of u within the boundary-affected region (McCorquodale and Munro, 2017a)[¶]. In this instance there would be no imbalance, on average, between the energy associated with turbulent motions incident towards the boundary and the energy of turbulent motions moving away from the boundary.

Figure 4.5(a-c) further indicate that an imbalance in u_{Q_2} and u_{Q_4} is re-established as the boundary is further approached, where $u_{Q_2}(\phi_T = 0) > u_{Q_4}(\phi_T = 0)$ over the

[¶]N.B. McCorquodale and Munro (2017a) is shown in chapter 3

region $0.3 \lesssim \xi/\delta_s \lesssim 0.6$. Hence, over this finite region the average energy associated with turbulent motions moving away from the boundary exceeds that of the energy of turbulent motions incident towards the boundary. There are two likely explanations for this trend: (i) there is a net intercomponent energy transfer from w^2 to u^2 associated with splats and antisplats over this region, or (ii) there is production and advection of TKE by the mean flow over this region. We note that the current results do depart from the zero-mean-shear condition and, therefore, effect (ii) is likely to contribute to the observed results. However, that $u_{Q_2} > u_{Q_4}$ over specifically the region $0.3 \lesssim \xi/\delta_s \lesssim 0.6$ is significant; recall that it was over this region that we observed significant increases in the normalised vertical strain rate $(\overline{\ell}_w/w)\partial u_3'/\partial x_3$ (see figure 4.4), which was indicative of splats and antisplats in which intercomponent energy transfer is concentrated (Perot and Moin, 1995a; Bodart et al., 2010). In addition, measurements of production and advection of TKE by the mean flow shown in figure 4.2 (terms Φ_{11} and A_{11}^d) indicate that mean flow effects are relatively small over this region.

We stress that the effect of splats and antisplats is isolated when $\phi_T = 6$ and is shown in figure 4.5(d), which also indicates that $u_{Q_2} > u_{Q_4}$ over $0.3 \lesssim \xi/\delta_s \lesssim 0.6$. Although not shown, we note that over the region $0.3 \leq \xi/\delta_s \leq 0.6$ the ratio u_{Q_4}/u_{Q_2} gradually decreases as ϕ_T is increased from 0 to 6, which we equate as being equivalent to gradually filtering out those motions that do not feel the inhibiting effects of the boundary. That this effect becomes more pronounced as ϕ_T increases cannot be attributed to mean flow effects (effect (ii) above), but instead is consistent with a net intercomponent energy transfer from w^2 to u^2 associated with splats and antisplats (effect (i) above) over the region $0.3 \lesssim \xi/\delta_s \lesssim 0.6$. Hence, we conclude not only that there is an energy transfer from w^2 to u^2 associated with splats and antisplats over this region (which can only be isolated by use of the condition $\phi_T = 6$), but that this energy transfer is largely able to dominate any weak additional contribution from the random turbulent fluctuations (characterised by $|(\overline{\ell}_w/w)\partial u_3'/\partial x_3| < 6$) that are included within the conditional statistics when $\phi_T < 6$. However, we note that a limitation of this analysis is that we are unable to derive insight into the precise dynamics that give rise to the observed splat antisplat disequilibrium and the associated intercomponent energy transfer over the region $0.3 \lesssim \xi/\delta_s \lesssim 0.6$.

We stress that the observations over the region $0.3 \leq \xi/\delta_s \leq 0.6$ are in contrast to the model of intercomponent energy transfer proposed by Perot and Moin (1995a), in which the intercomponent energy transfer describes a dissipative effect whereby the average energy of splats exceeds that of antisplats. However, note that significant changes in u_{Q_4} and u_{Q_2} occur closer to the boundary; figure 4.5 indicates that u_{Q_4}/u_{Q_2} increases over $\xi/\delta_s \lesssim 0.3$, irrespective of the value of ϕ_T. That this trend occurs over $\xi/\delta_s \lesssim 0.3$ is significant; recall that in the current experiments this is the approximate viscous sublayer thickness within which significant dissipation of TKE occurs (see McCorquodale and

Munro, 2017a)[¶]. These results physically indicate that, over this region, the energy associated with $u_1'u_1'$ of motions incident towards the boundary (splats) increases relative to and ultimately exceeds that of motions moving away from the boundary (antisplats). Hence, these measurements indicate that within a thin layer, approximately equal in thickness to the viscous sublayer, result are consistent with the model of Perot and Moin (1995a), in which the imbalance between splats and antisplats is governed by the dissipation of TKE.

4.6 Discussion and Conclusions

New results from an experimental study of the interaction between oscillating-grid turbulence and a solid boundary (positioned below and aligned parallel to the grid) have been presented which investigate the nature of the intercomponent energy transfer (described by the pressure-strain correlation Π_{ij}^s) that occurs within the boundary-affected region of the flow ($\xi/\delta_s \leq 1$). Within a region approximately equal in thickness to the viscous sublayer, estimates of the pressure-strain correlation Π_{ij}^s indicate that an intercomponent energy transfer occurs from the boundary-normal to the boundary tangential turbulent velocity components and which promotes anisotropy. Estimates of conditional turbulent statistics indicate that, within the region $\xi/\delta_s \lesssim 0.3$, intercomponent energy transfer is associated with splat-antisplat disequilibrium, whereby turbulent motions incident towards the boundary are more energetic than motions away, which are characteristics of an intercomponent energy transfer primarily driven by the dissipation of TKE (Perot and Moin, 1995a).

Estimates of Π_{ij}^s are shown to reduce outside the viscous sublayer, but continue to indicate a (much reduced) intercomponent energy transfer from the boundary-normal to the boundary-tangential velocity components (which also promotes anisotropy) over the region $0.3 \lesssim \xi/\delta_s \lesssim 0.6$. In section 4.3 we noted that similar data can be found in previous studies of the interaction of zero-mean-shear turbulence with an impermeable boundary (Perot and Moin, 1995a; Bodart et al., 2010), although the results have not previously received comment. Estimates of energy spectra (section 4.4) were also consistent with a weak net intercomponent energy transfer from the boundary-normal to the boundary-tangential velocity components at large spatial scales; similar observations have previously been reported (Hannoun et al., 1988; Kit et al., 1997; Brumley and Jirka, 1987; Hunt and Graham, 1978) which has been attributed to the effects of turbulent eddies as they impinge into a boundary (*i.e* splats) (Kit et al., 1997). However, results indicate this is not a traceless energy transfer between the velocity components; the increase in energy spectra at large scales of the boundary-tangential components is far smaller than the corresponding reduction in energy spectra at large scales of the

[¶]N.B. McCorquodale and Munro (2017a) is shown in chapter 3

boundary-normal component. Furthermore, estimates of conditional statistics associated with splats and antisplats indicate that over this region ($0.3 \lesssim \xi/\delta_s \lesssim 0.6$) the magnitude of the boundary-tangential turbulent velocity components of antisplats exceeds that of splats. Thus this splat-antisplat disequilibrium is indicative of a weak net intercomponent energy transfer from the boundary-normal velocity component to the boundary-tangential velocity components, but which is not consistent with the viscous dissipative model of energy transfer proposed by Perot and Moin (1995a) (that was prevalent in the viscous sublayer).

Instead, at first glance this energy transfer appears to be approximately in accordance with that proposed by Hunt and Graham (1978) for the interaction of zero-mean-shear turbulence and a solid boundary. However, whilst these results share the same basic interpretation (*i.e.* net energy transfer from w^2 to u^2), the current results are not consistent with the model proposed by Hunt and Graham (1978). That is, Hunt and Graham (1978) proposed that significant intercomponent energy transfer should occur only sufficiently close to the boundary - over the region $\xi/\delta_s \lesssim 0.3$. However, here the finite Reynolds numbers considered result in a thick viscous sublayer (of thickness $\delta_v/\delta_s \approx 0.2$ to 0.3, where δ_v denotes the thickness of the viscous sublayer), such that the energy transfer proposed by Hunt and Graham (1978) would be inhibited by viscous effects; recall that RDT is valid at the limit of high Reynolds number or constant dissipation with distance above the boundary (Magnaudet, 2003; Hunt, 1984) - neither of these conditions are satisfied here.

Bodart et al. (2010) also proposed that a net intercomponent energy transfer from the boundary-normal to the boundary-tangential turbulent velocity components should occur and that the intensity of the energy transfer should increase as the skewness ($\overline{u_3' u_3' u_3'}/w^3$) of flow increases. Bodart et al. (2010) acknowledge the role of viscosity in acting to increase the skewness of the flow close to the boundary, but argue that the imbalance in energy of splats and antisplats is set primarily by the skewness of the original velocity fields. However, a physical model consistent with the intercomponent energy transfer proposed by Bodart et al. (2010) has yet to be proposed. Evidently, a large skewness associated with anisotropic flow outside the boundary-affected region (such as that reported in OGT, see McCorquodale and Munro, 2017a)[¶] does describe an imbalance in the energy of turbulent motions, but it is our interpretation that this cannot be used as a direct measure of splat-antisplat imbalance (by which, recall, we refer to specifically turbulent motions that form stagnation flow as a result of boundary effects) within the boundary-affected region. That is, the blocking effect of the boundary on turbulent energy fluxes associated with such anisotropic flows has a significant effect on the imbalance of energy associated with turbulent motions inside the boundary-affected region, described by the correlation coefficients $\overline{u_3' u_3' u_3'}/w^3$ and $\overline{u_3' u_1' u_1'}/wu^2$, which is

[¶]N.B. McCorquodale and Munro (2017a) is shown in chapter 3

not associated with intercomponent energy transfer (McCorquodale and Munro, 2017a)¶. Indeed, despite the far-field flow here being anisotropic, the analysis of section 4.5 indicates splat-antisplat imbalance is actually small at the edge of the region in which we are able to identify splats and antisplats, and the imbalance only becomes significant for $\xi/\delta_s \leq 0.5$. Hence it appears that the current results over this region (*i.e.* just outside the viscous sublayer $\xi/\delta_s \approx 0.3$ to 0.6) identify a feature not captured within current key models of intercomponent energy transfer at a boundary.

A limitation in our analysis is that it does not identify an underlying physical mechanism to explain the observed intercomponent energy transfer over this region. However, so far our discussion of antisplats has focussed on regions in which the fluid ejects away from the boundary as a result of high pressure collisions of elements travelling tangential to the boundary (Perot and Moin, 1995a). In reality, antisplats can also form without significant increases in pressure due to the interaction of two regions of opposite vorticity when a splat approaches a boundary; so-called self-generation mechanisms (Hunt and Morrison, 2000; Bodart et al., 2010). That is, as a splat is blocked by the boundary, the no-slip conditions results in instantaneous shear and the vorticity associated with this shear acts to eject fluid away from the boundary. [To clarify, low pressure antisplat formation appears, in concept, similar to the process of vortex ring rebound at a solid impermeable boundary (see for example Walker et al., 1987; Orlandi and Verzicco, 1993; Munro et al., 2009)]. We stress that these events have been reported to give rise to a not-insignificant contribution to the time-averaged measurements of the pressure-strain term (Bodart et al., 2010). However, these events are not currently incorporated into key models of intercomponent energy transfer since their influence on this process is poorly understood due to their complicated dynamics. Indeed, Perot and Moin (1995a) explicitly note that the more complicated dynamics arising in this interaction are not considered in their model in which splats and antisplats arise as simple consequences of the equation of continuity. As a result, we conjecture that these events may be a contributing factor to the weak net intercomponent energy transfer observed here.

This observed net intercomponent energy transfer from w^2 to u^2 also has implications for our understanding of the 'return-to-isotropy' model of intercomponent energy transfer; recall that Walker et al. (1996) proposed that the anisotropy induced by the kinematic blocking condition acting on w^2 would give rise a 'return-to-isotropy' intercomponent energy transfer from u^2 to w^2. This mechanism is thought to be impeded within the viscous sublayer as a result of the prevalent viscous effects in this region (Perot and Moin, 1995a; McCorquodale and Munro, 2017a)¶. The current results further imply that this mechanism is impeded over a thin region even outside the viscous sublayer (in this study over the region $0.3 \lesssim \xi/\delta_s \lesssim 0.6$). Nevertheless, previous measurements of Π_{ij}^s illustrate that this mechanism is prevalent at the edge of the boundary-affected region in the

¶N.B. McCorquodale and Munro (2017a) is shown in chapter 3

interaction of OGT with an impermeable boundary (McCorquodale and Munro, 2017a)[¶] and in the interaction of zero-mean-shear turbulence with an impermeable boundary (Bodart et al., 2010; Perot and Moin, 1995a; Magnaudet, 2003).

Acknowledgements

The authors acknowledge Jim Meakin and Steve Lawton for technical support with the experimental apparatus. MWM acknowledges financial support through an Engineering and Physical Sciences Research Council Studentship (number 1510466).

References

Aronson, D., Johansson, A. V., and Löfdahl, L. (1997). Shear-free turbulence near a wall. *J. Fluid Mech.*, 338:363–395.

Biringen, S. and Reynolds, W. C. (1981). Large-eddy simulation of the shear-free turbulent boundary layer. *J. Fluid Mech.*, 103:53–63.

Bodart, J., Cazalbou, J. B., and Joly, L. (2010). Direct numerical simulation of unsheared turbulence diffusing towards a free-slip or no-slip surface. *J. Turbul.*, 11(48):1–18.

Brumley, B. H. and Jirka, G. H. (1987). Near-surface turbulence in a grid-stirred tank. *J. Fluid Mech.*, 183:235–263.

Fernando, H. J. S. and De Silva, I. P. D. (1993). Note on secondary flows in oscillating grid, mixing box experiments. *Phys. Fluids*, 5:1849–1851.

Hannoun, I. A., Fernando, H. J. S., and List, E. J. (1988). Turbulence structure near a sharp density interface. *J. Fluid Mech.*, 189:189–209.

Hinze, J. O. (1975). *Turbulence*. McGraw-Hill, 2nd edition.

Hopfinger, B. J. and Toly, J. A. (1976). Spatially decaying turbulence and its relation to mixing across density interfaces. *J. Fluid Mech.*, 78(1):155–175.

Hunt, J. C. R. (1984). Turbulence structure in thermal convection and shear-free boundary layers. *J. Fluid Mech.*, 138:161–184.

Hunt, J. C. R. and Graham, J. M. R. (1978). Free-stream turbulence near plane boundaries. *J. Fluid Mech.*, 84(2):209–235.

Hunt, J. C. R. and Morrison, J. F. (2000). Eddy structure in turbulent boundary layers. *Eur. J. Mech. B - Fluids*, 19:679–694.

Kit, E. L. G., Strang, E. J., and Fernando, H. J. S. (1997). Measurement of turbulence near shear-free density interfaces. *J. Fluid Mech.*, 334:293–314.

Magnaudet, J. (2003). High-Reynolds-number turbulence in a shear-free boundary layer: revisiting the Hunt-Graham theory. *J. Fluid Mech.*, 484:167–196.

[¶]N.B. McCorquodale and Munro (2017a) is shown in chapter 3

McCorquodale, M. W. and Munro, R. J. (2017a). Experimental study of oscillating-grid turbulence interacting with a solid boundary. *J. Fluid Mech.*, 813:768–798.

McCorquodale, M. W. and Munro, R. J. (2017b). A method for reducing mean flow in oscillating-grid turbulence. *In preparation for: Experiments in Fluids.*

McDougall, T. J. (1979). Measurements of turbulence in a zero-mean-shear mixed layer. *J. Fluid Mech.*, 94(3):409–431.

Munro, R. J., Bethke, N., and Dalziel, S. B. (2009). Sediment resuspension and erosion by vortex rings. *Phys. Fluids*, 21:046601.

Orlandi, P. and Verzicco, R. (1993). Vortex rings impining on walls: axisymmetric and three-dimensional simulations. *J. Fluid Mech.*, 256:615–646.

Perot, B. and Moin, P. (1995a). Shear free turbulent boundary layers, Part 1, physical insights into near-wall turbulence. *J. Fluid Mech.*, 295:199–227.

Perot, B. and Moin, P. (1995b). Shear free turbulent boundary layers, Part 2, new concepts for Reynolds stress transport equation modelling of inhomogeneous flows. *J. Fluid Mech.*, 295:229–245.

Pope, S. B. (2000). *Turbulent Flows.* Cambridge University Press, 1st edition.

Thomas, N. H. and Hancock, P. E. (1977). Grid turbulence near a moving wall. *J. Fluid Mech.*, 82(3):481–496.

Uzkan, T. and Reynolds, W. C. (1967). A shear-free turbulent boundary layer. *J. Fluid Mech.*, 28(4):803–821.

Walker, D. T., Leighton, R. I., and Garza-Rios, L. O. (1996). Shear-free turbulence near a flat free surface. *J. Fluid Mech.*, 320:19–51.

Walker, J. D. A., Smith, C. R., Cerra, A. W., and Doligalski, T. L. (1987). The impact of a vortex ring on a wall. *J. Fluid Mech.*, 181:99–140.

Chapter 5

Summary

5.1 Conclusions

This work has described laboratory experiments that investigate the interaction of OGT and a solid impermeable boundary. The overall objective of these experiments was to provide insight into the physical mechanisms that govern the interaction of zero-mean-shear turbulence and a solid impermeable boundary.

A detailed preliminary study to characterise the flow generated by the OGT apparatus was initially performed, using two-dimensional PIV applied to the vertical plane through the centre of the grid. Ensemble-averaged measurements of the fluid velocity fields taken at specific stages of the grid's oscillation indicated the presence of side wall related effects that gave rise to large-scale circulations within the flow. That is, the boundary conditions imposed on the flow at the vertical tank side walls, together with the edge conditions of the grid, combined to give rise to a complicated three-dimensional flow structure in the wake around the perimeter of the oscillating grid, which resulted in the merging of grid-induced jets, below the lowest point of the grid's oscillation, close to the tank side walls. These merged outer jets penetrated to a greater depth below the grid before decaying than those jets produced close to the centre of the oscillating grid, thereby inducing large-scale circulations within the flow. However, installation of an open-ended cuboidal 'inner box' (positioned centrally on-plan on the base of the tank, with its top edge 1 cm below the bottom of the grid's oscillation) was shown to inhibit the formation of the merged outer jets and confine the large-scale circulations within the flow to the compartment between the inner box and container walls. Within the inner box, a more regular jet structure was observed close to the oscillating grid that broke down to produce turbulence that was approximately homogeneous and isotropic on planes parallel to the grid, across the central 50% of the inner box's width, and which decayed with distance beneath the grid. The corresponding mean velocity components were significantly reduced in magnitude (by a factor of approximately 6) relative to the flow observed when the inner box was not installed, such that the mean flow velocity components were small compared to the velocity fluctuations, thereby enabling a meaningful comparison to be

made with zero-mean-shear turbulence.

Consequently, these techniques were used in the subsequent investigation of the interaction of OGT with a solid impermeable boundary, positioned below and parallel to the horizontal plane of the oscillating-grid. The inhibiting effect of the boundary was shown to monotonically reduce the magnitude of the boundary-normal rms turbulent velocity component over a region approximately one integral length scale in thickness, as a result of the kinematic blocking condition imposed by the boundary. In contrast, the boundary-tangential rms turbulent velocity components were found to be amplified within the boundary-affected region, relative to their expected values in the absence of the boundary, except within a thin layer close to the boundary within which viscous effects were dominant. Likewise, measurements of the TKE indicated that there was actually an increase in TKE within the boundary-affected region, relative to the expected values in the absence of the boundary, except within the thin layer closer to the boundary within which the boundary-tangential turbulent velocity components were inhibited. Within this thin viscous region the turbulent velocity components were inhibited as the no-slip condition imposed by the boundary gave rise to an increase in the viscous dissipation of TKE.

Estimates of the terms of the transport equation of TKE indicated that the increase in TKE within the boundary-affected region, and the associated increase in the boundary-tangential rms turbulent velocity components, was principally a result of the effect of the kinematic blocking condition of the boundary acting to inhibit a boundary-normal TKE flux. That is, the spatial decay of the rms turbulent velocity components normal to and away from the oscillating grid gave rise to a vertical flux of TKE away from the grid towards the boundary. The blocking effect of the boundary inhibited this vertical flux of TKE and gave rise to an increase in TKE within the boundary-affected region of the flow, relative to expected values in the absence of the boundary. An important implication of this result is that in zero-mean-shear turbulence amplified values of the boundary-tangential rms turbulent velocity components can occur in the boundary-affected region in the absence of intercomponent energy transfer from the boundary-normal to the boundary-tangential turbulent velocity components. This is a critical point which has received little focus in previous related studies. That is, in well-established models of this interaction (Hunt and Graham, 1978; Perot and Moin, 1995a) amplified values of the boundary-tangential turbulent velocity components are attributed to the effects of intercomponent energy transfer and previous authors do not account for the effects of this energy flux mechanism within their models. Critically, this flow feature provides a physical mechanism that goes some way to explain the differences in results present in the previous literature, by noting that results from studies conducted in otherwise homogenous turbulence can be viewed as a limiting case at which the effects of this mechanism tend to zero, such that the amplification of the boundary-tangential

turbulent velocity components is small following boundary insertion (as per the results of, for example, Perot and Moin, 1995a; Aronson et al., 1997).

Further insights have also been derived into the nature of the intercomponent energy transfer that occurs in the boundary-affected region of the flow, described by the pressure-strain term Π_{ij}^{s} of the transport equation of the Reynolds stress tensor; this is a particularly controversial aspect of the interaction (Perot and Moin, 1995a; Hunt and Graham, 1978; Bodart et al., 2010). Measurements of Π_{ij}^{s} indicated that over a thin region adjacent to the boundary, approximately equal in thickness to the viscous sublayer, an intercomponent energy transfer occured from the boundary-normal to the boundary-tangential turbulent velocity components. Results indicated that this energy transfer was associated with splats and antisplats, whereby turbulent motions impinging onto the boundary (splats) were on average more energetic than turbulent motions ejecting away from the boundary (antisplats), as a result of the viscous dissipation of TKE from fluid elements as they travel close to the boundary. These results were consistent with the viscous model of intercomponent energy transfer proposed by Perot and Moin (1995a).

In a thin layer just outside the viscous sublayer Π_{ij}^{s} was shown to reduce, indicating the presence of a weak intercomponent energy transfer from the boundary-normal to the boundary-tangential turbulent velocity components which was not captured within existing models of energy transfer. That is, results consistent with those observed here are available in previous studies (Perot and Moin, 1995a; Bodart et al., 2010), but the feature identified here has not previously received comment. Conditional turbulent statistics indicated that this energy transfer was also linked to an imbalance in the energy associated with splats and antisplats, whereby the magnitude of the boundary-tangential turbulent velocity components associated with antisplats exceeded that associated with splats. This result, and measurements of the correlation coefficients and energy spectra, indicated that the energy transfer described by this imbalance manifested as a net transfer of energy between the velocity components during the formation of splats and antisplats. However, analysis conducted here was unable to identify an underlying physical mechanism to explain this intercomponent energy transfer, although it was conjectured that the energy transfer may be related to the 'self-generation' of antisplats through viscous effects (Hunt and Morrison, 2000; Bodart et al., 2010).

At the edge of the boundary-affected region Π_{ij}^{s} was shown to further reduce, consistent with the presence of an intercomponent energy transfer from the (energy rich) boundary-tangential turbulent velocity components to the (energy poor) boundary-normal turbulent velocity component, as per previous related studies (Walker et al., 1996), in a so-called 'return-to-isotropy' energy transfer. However, this energy transfer was proposed not to be independent of the dominant energy flux mechanism (discussed above). That is, since the blocking of a TKE flux aligned towards the boundary acts to increase the magnitude

of the boundary-tangential turbulent velocity components but not the boundary-normal turbulent velocity component, the blocking of a TKE flux towards the boundary promotes Reynolds stress anisotropy within the boundary-affected region. Since it is Reynolds stress anisotropy that drives this intercomponent energy transfer (Walker et al., 1996), increasing the level of anisotropy within the boundary-affected region (through the effects of blocking a TKE flux towards the boundary) may promote a stronger energy transfer.

In summary, the current results have shown that the effect of a solid impermeable boundary on turbulent velocity components in zero-mean-shear turbulence depends crucially on the nature of the original turbulent flow (*i.e.* homogeneous versus inhomogeneous turbulence). In addition, new insight has been derived into the mechanisms that govern the interaction of approximately zero-mean-shear turbulence and an impermeable boundary, which feature both kinematic and viscous roots and appear to be more complex than commonly acknowledged models of the interaction (Perot and Moin, 1995a; Hunt and Graham, 1978).

5.2 Future work

There are a number of aspects of the interaction between approximately zero-mean-shear turbulence and a solid impermeable boundary that require further study. In particular, this research has identified the presence of an intercomponent energy transfer within the boundary-affected region of the flow that is not captured within existing models of intercomponent energy transfer at the boundary. However, it was not possible to derive insight into the precise dynamics that gave rise to this energy transfer. In addition, uncertainty remains regarding the physical scales of turbulent motions that are dominant in giving rise to the energy transfer that occurs within the boundary-affected region of the flow. A more complete understanding of the dynamics of this interaction could be derived by addressing these limitations. Note also that previous insights derived from studying this interaction have resulted in revised Reynolds stress transport equation models that account for some boundary related effects on the flow (Perot and Moin, 1995b). It is anticipated that the insights derived from the current work could lead to the further development of such models.

In addition, the work presented here could be viewed as addressing only a limiting case in the interaction between zero-mean-shear turbulence and boundaries. That is, whilst many turbulent flows are bound by a rigid impermeable surface, there are also a wide variety of natural and engineered turbulent flows in which the flow interacts with a permeable material. Applications of these flows include, for example, fracking, oil recovery and in a variety of manufacturing processes. In these applications it is desirable to be able to accurately predict the rate of mass transfer that would be induced by a flow under given conditions. As such, it is necessary to be able to accurately describe the

effects of a permeable boundary on a turbulent flow. However, results derived from the study of impermeable boundaries can only be assumed to be applicable in the limiting case that the boundary permeability tends to zero. Commonly this condition is expressed as the limiting condition when the permeability Reynolds number Re_K, which represents the ratio of the typical diameter of a pore of the permeable boundary to a viscous length scale, is small (*i.e.* less than order one; see, for example Hanh et al., 2002; Breugem et al., 2006). When the permeability Reynolds number exceeds order one permeability effects become significant in the interaction between a turbulent flow and a boundary (see, for example, Breugem et al., 2006; Manes et al., 2011).

However, there are a number of factors that complicate the study of the interaction of a turbulent flow with a permeable boundary. One such factor is that increasing the boundary permeability (*i.e* increasing Re_K) alters both the direct effect of the boundary on turbulent fluctuations and the indirect effect of the boundary on turbulent fluctuations, relating to the production of TKE, through changes relating to the mean-shear in the boundary-affected region. Consequently, although many studies report similar observations, such as, for example, a weakening of coherent structures as Re_K increases in the turbulent boundary layer above a permeable boundary (see, for example, Hanh et al., 2002; Rosti et al., 2015; Suga et al., 2011, 2017; Yokojima, 2011; Breugem et al., 2006), it can be difficult to interpret these observations in terms of the effects of boundary permeability on the underlying physical mechanisms. That is, it is unclear if, for example, coherent structures are inhibited as a result of a reduction in mean shear (*i.e.* an indirect effect on the turbulence) or if the relaxation of the no-blocking condition gives rise to larger wall-normal turbulent velocities (*i.e.* a direct effect on the turbulence) that prevent the development of elongated coherent structures (Breugem et al., 2006). Consequently, a better understanding of the dynamics of the turbulent boundary layer above a permeable boundary may be derived by separating the direct and indirect effects of the boundary on the flow through the study of zero-mean-shear turbulence.

However, studies of the effects of boundary permeability within the interaction of zero-mean-shear turbulence and a boundary are unprecedented. In the most closely related study the effects of a 'perfectly permeable boundary' on initially homogeneous isotropic zero-mean-shear turbulence were studied through Direct Numerical Simulation (Perot and Moin, 1995a). Note that a 'perfectly permeable boundary' is defined as a boundary upon which fluid is able to move unimpeded through the boundary in the boundary-normal direction, but at which any motion tangential to the boundary is inhibited. Consequently, the nature of the applied boundary conditions render the results of this study (Perot and Moin, 1995a) hard to interpret for a natural permeable material. That is, to model permeable boundaries exactly one would need to impose the no-slip and no-penetration boundary conditions on the highly convoluted surfaces that constitute the permeable material; a requirement that is currently commonly unfeasible

in computational fluid dynamics (Rosti et al., 2015) and which was not the aim of the study of Perot and Moin (1995a). Rather, Perot and Moin (1995a) simply sought to study the effects of imposing the no-slip condition at a boundary in isolation from the no-penetration condition. Thus, significant new insight could be derived into the effects of boundary permeability within the interaction of a boundary and a turbulent flow by studying the interaction of OGT with permeable boundaries.

Future work investigating the interaction of OGT with boundaries could also take advantage of modern developments in experimental measurement techniques. That is, a limitation of the data presented here is that it was only possible to obtain measurements of two components of the velocity field on a single thin plane within the flow. Thus, when analysing this data it was necessary to make assumptions relating to the third velocity component in order to derive insight into the dominant physical processes that governed the flow. However, modern advances in PIV now enable time-resolved measurements of each velocity component within a turbulent flow (for a recent review see, for example, Westerweel et al., 2013). Some of these approaches, such as multi-plane stereoscopic PIV (see, for example, Kähler and Kompenhans, 2000), are able to resolve all three velocity components (and the associated spatial derivatives) without reducing the resulting spatial resolution of the measured velocity field; a limitation of some volumetric approaches (Elsinga et al., 2006). Measurements obtained by applying this technique to the flow would enable a direct estimation of many of the terms of the transport equation of the Reynolds stress tensor without resorting to the limiting assumptions used here (*i.e.* those detailed in sections 3.5.2 and 4.3). Such advances would enable more accurate and reliable estimates of controversial aspects of the interaction, such as estimates of intercomponent energy transfer as described by the pressure-strain term. However, even using these techniques the experimental data that could be obtained would be limited to measurements of the velocity field and further insight (relating, in particular, to the pressure field) could be obtained from parallel studies using computational approaches.

References

Aronson, D., Johansson, A. V., and Löfdahl, L. (1997). Shear-free turbulence near a wall. *J. Fluid Mech.*, 338:363–395.

Bodart, J., Cazalbou, J. B., and Joly, L. (2010). Direct numerical simulation of unsheared turbulence diffusing towards a free-slip or no-slip surface. *J. Turbul.*, 11(48):1–18.

Breugem, W. P., Boersma, B. J., and Uittenbogaard, R. E. (2006). The influence of wall permeability on turbulent channel flow. *J. Fluid Mech.*, 562:35–72.

Elsinga, G. E., Scarano, F., Wieneke, B., and van Oudheusden, B. W. (2006). Tomographic particle image velocimetry. *Exp. Fluids*, 41:933–947.

Hanh, S., Je, J., and Choi, H. (2002). Direct numerical simulation of turbulent channel flow with permeable walls. *J. Fluid Mech.*, 450:259–285.

Hunt, J. C. R. and Graham, J. M. R. (1978). Free-stream turbulence near plane boundaries. *J. Fluid Mech.*, 84(2):209–235.

Hunt, J. C. R. and Morrison, J. F. (2000). Eddy structure in turbulent boundary layers. *Eur. J. Mech. B - Fluids*, 19:679–694.

Kähler, C. J. and Kompenhans, J. (2000). Fundamentals of multiple plane stereo particle image velocimetry. *Exp. Fluids*, Suppl.:S70–S77.

Manes, C., Poggi, D., and Ridolfi, L. (2011). Turbulent boundary layers over permeable walls: scaling and near-wall structure. *J. Fluid Mech.*, 687:141–170.

Perot, B. and Moin, P. (1995a). Shear free turbulent boundary layers, Part 1, physical insights into near-wall turbulence. *J. Fluid Mech.*, 295:199–227.

Perot, B. and Moin, P. (1995b). Shear free turbulent boundary layers, Part 2, new concepts for Reynolds stress transport equation modelling of inhomogeneous flows. *J. Fluid Mech.*, 295:229–245.

Rosti, M. E., Cortelezzi, L., and Quadrio, M. (2015). Direct numerical simulation of turbulent channel flow over porous walls. *J. Fluid Mech.*, 784:396–442.

Suga, K., Mori, M., and Kaneda, M. (2011). Vortex structure of turbulence over permeable walls. *Int. J. Heat and Fluid Flow*, 32:586–595.

Suga, K., Nakagawa, Y., and Kaneda, M. (2017). Spanwise turbulence structure over permeable walls. *Journal of Fluid Mechanics*, 822:186–201.

Walker, D. T., Leighton, R. I., and Garza-Rios, L. O. (1996). Shear-free turbulence near a flat free surface. *J. Fluid Mech.*, 320:19–51.

Westerweel, J., Elsinga, G. E., and Adrian, R. J. (2013). Particle image velocimetry for complex and turbulent flows. *Annu. Rev. Fluid Mech.*, 45:409–436.

Yokojima, S. (2011). Effect of wall permeability on wall-bounded turbulent flows. *J. Phys. Soc. Jpn.*, 80:033401.